The Astrophysical Journal Letters, 930:L19 (32pp), 2022 May 10 https://doi.org/10.3847/2041-8213/ac6428

Millimeter Light Curves of Sagittarius A* Observed during the 2017 Event Horizon Telescope Campaign

Maciek Wielgus[1], Nicola Marchili[2,1], Iván Martí-Vidal[3,4], Garrett K. Keating[5], Venkatessh Ramakrishnan[6,7,8], Paul Tiede[5,9], Ed Fomalont[10], Sara Issaoun[5,11], Joey Neilsen[12], Michael A. Nowak[13], Lindy Blackburn[9,5], Charles F. Gammie[14,15], Ciriaco Goddi[16,17], Daryl Haggard[18,19], Daeyoung Lee[14], Monika Moscibrodzka[20], Alexandra J. Tetarenko[21,11], Geoffrey C. Bower[22,23], Chi-kwan Chan[24,25], Koushik Chatterjee[9,5], Paul M. Chesler[9], Jason Dexter[26], Sheperd S. Doeleman[9,5], Boris Georgiev[27,28,29], Mark Gurwell[5], Michael D. Johnson[9,5], Daniel P. Marrone[24], Alejandro Mus[3,4], Dimitrios Psaltis[24], Bart Ripperda[30,31], Gunther Witzel[1], Kazunori Akiyama[32,33,9], Antxon Alberdi[34], Walter Alef[1], Juan Carlos Algaba[35], Richard Anantua[9,5,36], Keiichi Asada[37], Rebecca Azulay[3,4,1], Uwe Bach[1], Anne-Kathrin Baczko[1], David Ball[24], Mislav Baloković[38], John Barrett[32], Michi Bauböck[14], Bradford A. Benson[39,40], Dan Bintley[41,42], Raymond Blundell[5], Wilfred Boland[43], Katherine L. Bouman[44], Hope Boyce[18,19], Michael Bremer[45], Christiaan D. Brinkerink[20], Roger Brissenden[9,5], Silke Britzen[1], Avery E. Broderick[29,27,28], Dominique Broguiere[45], Thomas Bronzwaer[20], Sandra Bustamante[46], Do-Young Byun[47,48], John E. Carlstrom[49,40,50,51], Chiara Ceccobello[52], Andrew Chael[53,11], Shami Chatterjee[54], Ming-Tang Chen[22], Yongjun Chen (陈永军)[55,56], Ilje Cho[34], Pierre Christian[57], Nicholas S. Conroy[15,5], John E. Conway[52], James M. Cordes[54], Thomas M. Crawford[40,49], Geoffrey B. Crew[32], Alejandro Cruz-Osorio[58], Yuzhu Cui[59,60,61], Jordy Davelaar[62,31,20], Mariafelicia De Laurentis[63,58,64], Roger Deane[65,66,67], Jessica Dempsey[41,42,68], Gregory Desvignes[1,69], Vedant Dhruv[14], Sergio A. Dzib[45,1], Ralph P. Eatough[70,1], Razieh Emami[5], Heino Falcke[20], Joseph Farah[71,72], Vincent L. Fish[32], H. Alyson Ford[24], Raquel Fraga-Encinas[20], William T. Freeman[73,74], Per Friberg[41,42], Christian M. Fromm[75,58,1], Antonio Fuentes[34], Peter Galison[9,76,77], Roberto García[45], Olivier Gentaz[45], Roman Gold[78,58], Arturo I. Gómez-Ruiz[79,80], José L. Gómez[81], Minfeng Gu (顾敏峰)[55,82], Kazuhiro Hada[60,61], Kari Haworth[5], Michael H. Hecht[32], Ronald Hesper[83], Luis C. Ho (何子山)[84,85], Paul Ho[37,42], Mareki Honma[60,61,86], Chih-Wei L. Huang[37], Lei Huang (黄磊)[55,82], David H. Hughes[79], Shiro Ikeda[33,87,88,89], C. M. Violette Impellizzeri[90,10], Makoto Inoue[37], David J. James[91], Buell T. Jannuzi[24], Michael Janssen[1], Britton Jeter[37], Wu Jiang (江悟)[55], Alejandra Jiménez-Rosales[20], Svetlana Jorstad[92], Abhishek V. Joshi[14], Taehyun Jung[47,48], Mansour Karami[29,27], Ramesh Karuppusamy[1], Tomohisa Kawashima[93], Mark Kettenis[94], Dong-Jin Kim[1], Jae-Young Kim[95,47,1], Jongsoo Kim[47], Junhan Kim[24,44], Motoki Kino[33,96], Jun Yi Koay[37], Prashant Kocherlakota[58], Yutaro Kofuji[60,86], Patrick M. Koch[37], Shoko Koyama[97,37], Carsten Kramer[45], Michael Kramer[1], Thomas P. Krichbaum[1], Cheng-Yu Kuo[98,37], Noemi La Bella[20], Tod R. Lauer[99], Sang-Sung Lee[47], Po Kin Leung[100], Aviad Levis[44], Zhiyuan Li (李志远)[101,102], Rocco Lico[34,103,1], Greg Lindahl[5], Michael Lindqvist[52], Mikhail Lisakov[1], Jun Liu (刘俊)[1], Kuo Liu[1], Elisabetta Liuzzo[2], Wen-Ping Lo[37,104], Andrei P. Lobanov[1], Laurent Loinard[105,106], Colin Lonsdale[32], Ru-Sen Lu (路如森)[41,42,55,107,1], Jirong Mao (毛基荣)[41,42,108,109,110], Sera Markoff[111,112], Alan P. Marscher[92], Satoki Matsushita[37], Lynn D. Matthews[32], Lia Medeiros[113,24], Karl M. Menten[1], Daniel Michalik[114,40], Izumi Mizuno[41,42], Yosuke Mizuno[59,115,58], James M. Moran[9,5], Kotaro Moriyama[32,60,58], Cornelia Müller[1,20], Gibwa Musoke[111,20], Ioannis Myserlis[116], Andrew Nadolski[15], Hiroshi Nagai[33,61], Neil M. Nagar[6], Masanori Nakamura[117,37], Ramesh Narayan[9,5], Gopal Narayanan[46], Iniyan Natarajan[65,118], Antonios Nathanail[58,119], Santiago Navarro Fuentes[116], Roberto Neri[45], Chunchong Ni[27,28,29], Aristeidis Noutsos[1], Junghwan Oh[120], Hiroki Okino[60,86], Héctor Olivares[20], Gisela N. Ortiz-León[121], Tomoaki Oyama[60], Feryal Özel[24], Daniel C. M. Palumbo[9,5], Georgios Filippos Paraschos[1], Jongho Park[37,122], Harriet Parsons[41,42], Nimesh Patel[5], Ue-Li Pen[37,29,123,124,125], Dominic W. Pesce[5,9], Vincent Piétu[45], Richard Plambeck[126], Aleksandar PopStefanija[46], Oliver Porth[111,58], Felix M. Pötzl[127,1], Ben Prather[14], Jorge A. Preciado-López[29], Hung-Yi Pu[128,129,37], Ramprasad Rao[22], Mark G. Rawlings[130,41,42], Alexander W. Raymond[9,5], Luciano Rezzolla[58,131,132], Angelo Ricarte[5,9], Freek Roelofs[5,9,20], Alan Rogers[32], Eduardo Ros[1], Cristina Romero-Canizales[37], Arash Roshanineshat[24], Helge Rottmann[1], Alan L. Roy[1], Ignacio Ruiz[116], Chet Ruszczyk[32], Kazi L. J. Rygl[2], Salvador Sánchez[116], David Sánchez-Argüelles[79,80], Miguel Sánchez-Portal[116], Mahito Sasada[60,133], Kaushik Satapathy[24], Tuomas Savolainen[134,8,1], F. Peter Schloerb[46], Karl-Friedrich Schuster[45], Lijing Shao[85,1], Zhiqiang Shen (沈志强)[41,42,55,56], Des Small[94], Bong Won Sohn[41,42,47,48,135], Jason SooHoo[32], Kamal Souccar[46], He Sun (孙赫)[44], Fumie Tazaki[60], Remo P. J. Tilanus[20,90,136,24], Michael Titus[32], Pablo Torne[116,1], Efthalia Traianou[81,1], Tyler Trent[24], Sascha Trippe[137,41,42], Ilse van Bemmel[94], Huib Jan van Langevelde[94,90,138], Daniel R. van Rossum[20], Jesse Vos[20], Jan Wagner[1], Derek Ward-Thompson[139], John Wardle[140], Jonathan Weintroub[9,5], Norbert Wex[1], Robert Wharton[1], Kaj Wiik[141], Michael F. Wondrak[20,142], George N. Wong[113,143], Qingwen Wu (吴庆文)[41,42,144], Paul Yamaguchi[5], Doosoo Yoon[111], André Young[20], Ken Young[5], Ziri Younsi[145,58], Feng Yuan (袁峰)[41,42,55,82,146], Ye-Fei Yuan (袁业飞)[41,42,147], J. Anton Zensus[1], Shuo Zhang[148], Guang-Yao Zhao[34], and Shan-Shan Zhao[55]

[1] Max-Planck-Institut für Radioastronomie, Auf dem Hügel 69, D-53121 Bonn, Germany; maciek.wielgus@gmail.com
[2] Italian ALMA Regional Centre, INAF-Istituto di Radioastronomia, Via P. Gobetti 101, I-40129 Bologna, Italy
[3] Departament d'Astronomia i Astrofísica, Universitat de València, C. Dr. Moliner 50, E-46100 Burjassot, València, Spain
[4] Observatori Astronòmic, Universitat de València, C. Catedrático José Beltrán 2, E-46980 Paterna, València, Spain
[5] Center for Astrophysics, Harvard & Smithsonian, 60 Garden Street, Cambridge, MA 02138, USA
[6] Astronomy Department, Universidad de Concepción, Casilla 160-C, Concepción, Chile
[7] Finnish Centre for Astronomy with ESO, FI-20014 University of Turku, Finland
[8] Aalto University Metsähovi Radio Observatory, Metsähovintie 114, FI-02540 Kylmälä, Finland
[9] Black Hole Initiative at Harvard University, 20 Garden Street, Cambridge, MA 02138, USA
[10] National Radio Astronomy Observatory, 520 Edgemont Road, Charlottesville, VA 22903, USA
[11] NASA Hubble Fellowship Program, Einstein Fellow
[12] Villanova University, Mendel Science Center Rm. 263B, 800 E. Lancaster Ave., Villanova, PA 19085, USA
[13] Physics Department, Washington University CB 1105, St. Louis, MO 63130, USA
[14] Department of Physics, University of Illinois, 1110 West Green Street, Urbana, IL 61801, USA
[15] Department of Astronomy, University of Illinois at Urbana-Champaign, 1002 West Green Street, Urbana, IL 61801, USA
[16] Dipartimento di Fisica, Universitá degli Studi di Cagliari, SP Monserrato-Sestu km 0.7, I-09042 Monserrato, Italy
[17] INAF—Osservatorio Astronomico di Cagliari, Via della Scienza 5, I-09047, Selargius, CA, Italy
[18] Department of Physics, McGill University, 3600 rue University, Montréal, QC H3A 2T8, Canada
[19] McGill Space Institute, McGill University, 3550 rue University, Montréal, QC H3A 2A7, Canada
[20] Department of Astrophysics, Institute for Mathematics, Astrophysics and Particle Physics (IMAPP), Radboud University, P.O. Box 9010, 6500 GL Nijmegen, The Netherlands
[21] Department of Physics and Astronomy, Texas Tech University, Lubbock, TX 79409-1051, USA
[22] Institute of Astronomy and Astrophysics, Academia Sinica, 645 N. A'ohoku Place, Hilo, HI 96720, USA
[23] Department of Physics and Astronomy, University of Hawaii at Manoa, 2505 Correa Road, Honolulu, HI 96822, USA
[24] Steward Observatory and Department of Astronomy, University of Arizona, 933 N. Cherry Ave., Tucson, AZ 85721, USA
[25] Data Science Institute, University of Arizona, 1230 N. Cherry Ave., Tucson, AZ 85721, USA
[26] JILA and Department of Astrophysical and Planetary Sciences, University of Colorado, Boulder, CO 80309, USA
[27] Department of Physics and Astronomy, University of Waterloo, 200 University Avenue West, Waterloo, ON N2L 3G1, Canada
[28] Waterloo Centre for Astrophysics, University of Waterloo, Waterloo, ON N2L 3G1, Canada
[29] Perimeter Institute for Theoretical Physics, 31 Caroline Street North, Waterloo, ON N2L 2Y5, Canada
[30] Department of Astrophysical Sciences, Peyton Hall, Princeton University, Princeton, NJ 08544, USA
[31] Center for Computational Astrophysics, Flatiron Institute, 162 Fifth Avenue, New York, NY 10010, USA
[32] Massachusetts Institute of Technology Haystack Observatory, 99 Millstone Road, Westford, MA 01886, USA
[33] National Astronomical Observatory of Japan, 2-21-1 Osawa, Mitaka, Tokyo 181-8588, Japan
[34] Instituto de Astrofísica de Andalucía-CSIC, Glorieta de la Astronomía s/n, E-18008 Granada, Spain
[35] Department of Physics, Faculty of Science, Universiti Malaya, 50603 Kuala Lumpur, Malaysia
[36] Department of Physics & Astronomy, The University of Texas at San Antonio, 1 UTSA Circle, San Antonio, TX 78249, USA
[37] Institute of Astronomy and Astrophysics, Academia Sinica, 11F of Astronomy-Mathematics Building, AS/NTU No. 1, Sec. 4, Roosevelt Rd., Taipei 10617, Taiwan, R.O.C.
[38] Yale Center for Astronomy & Astrophysics, Yale University, 52 Hillhouse Avenue, New Haven, CT 06511, USA
[39] Fermi National Accelerator Laboratory, MS209, P.O. Box 500, Batavia, IL 60510, USA
[40] Department of Astronomy and Astrophysics, University of Chicago, 5640 South Ellis Avenue, Chicago, IL 60637, USA
[41] East Asian Observatory, 660 N. A'ohoku Place, Hilo, HI 96720, USA
[42] James Clerk Maxwell Telescope (JCMT), 660 N. A'ohoku Place, Hilo, HI 96720, USA
[43] Nederlandse Onderzoekschool voor Astronomie (NOVA), PO Box 9513, 2300 RA Leiden, The Netherlands
[44] California Institute of Technology, 1200 East California Boulevard, Pasadena, CA 91125, USA
[45] Institut de Radioastronomie Millimétrique, 300 rue de la Piscine, F-38406 Saint Martin d'Hères, France
[46] Department of Astronomy, University of Massachusetts, 01003, Amherst, MA, USA
[47] Korea Astronomy and Space Science Institute, Daedeok-daero 776, Yuseong-gu, Daejeon 34055, Republic of Korea
[48] University of Science and Technology, Gajeong-ro 217, Yuseong-gu, Daejeon 34113, Republic of Korea
[49] Kavli Institute for Cosmological Physics, University of Chicago, 5640 South Ellis Avenue, Chicago, IL 60637, USA
[50] Department of Physics, University of Chicago, 5720 South Ellis Avenue, Chicago, IL 60637, USA
[51] Enrico Fermi Institute, University of Chicago, 5640 South Ellis Avenue, Chicago, IL 60637, USA
[52] Department of Space, Earth and Environment, Chalmers University of Technology, Onsala Space Observatory, SE-43992 Onsala, Sweden
[53] Princeton Center for Theoretical Science, Jadwin Hall, Princeton University, Princeton, NJ 08544, USA
[54] Cornell Center for Astrophysics and Planetary Science, Cornell University, Ithaca, NY 14853, USA
[55] Shanghai Astronomical Observatory, Chinese Academy of Sciences, 80 Nandan Road, Shanghai 200030, People's Republic of China
[56] Key Laboratory of Radio Astronomy, Chinese Academy of Sciences, Nanjing 210008, People's Republic of China
[57] Physics Department, Fairfield University, 1073 North Benson Road, Fairfield, CT 06824, USA
[58] Institut für Theoretische Physik, Goethe-Universität Frankfurt, Max-von-Laue-Straße 1, D-60438 Frankfurt am Main, Germany
[59] Tsung-Dao Lee Institute, Shanghai Jiao Tong University, Shengrong Road 520, Shanghai, 201210, People's Republic of China
[60] Mizusawa VLBI Observatory, National Astronomical Observatory of Japan, 2-12 Hoshigaoka, Mizusawa, Oshu, Iwate 023-0861, Japan
[61] Department of Astronomical Science, The Graduate University for Advanced Studies (SOKENDAI), 2-21-1 Osawa, Mitaka, Tokyo 181-8588, Japan
[62] Department of Astronomy and Columbia Astrophysics Laboratory, Columbia University, 550 W. 120th Street, New York, NY 10027, USA
[63] Dipartimento di Fisica "E. Pancini," Universitá di Napoli "Federico II," Compl. Univ. di Monte S. Angelo, Edificio G, Via Cinthia, I-80126, Napoli, Italy
[64] INFN Sez. di Napoli, Compl. Univ. di Monte S. Angelo, Edificio G, Via Cinthia, I-80126, Napoli, Italy
[65] Wits Centre for Astrophysics, University of the Witwatersrand, 1 Jan Smuts Avenue, Braamfontein, Johannesburg 2050, South Africa
[66] Department of Physics, University of Pretoria, Hatfield, Pretoria 0028, South Africa
[67] Centre for Radio Astronomy Techniques and Technologies, Department of Physics and Electronics, Rhodes University, Makhanda 6140, South Africa
[68] ASTRON, Oude Hoogeveensedijk 4, 7991 PD Dwingeloo, The Netherlands
[69] LESIA, Observatoire de Paris, Université PSL, CNRS, Sorbonne Université, Université de Paris, 5 place Jules Janssen, F-92195 Meudon, France
[70] National Astronomical Observatories, Chinese Academy of Sciences, 20A Datun Road, Chaoyang District, Beijing 100101, People's Republic of China
[71] Las Cumbres Observatory, 6740 Cortona Drive, Suite 102, Goleta, CA 93117-5575, USA
[72] Department of Physics, University of California, Santa Barbara, CA 93106-9530, USA
[73] Department of Electrical Engineering and Computer Science, Massachusetts Institute of Technology, 32-D476, 77 Massachusetts Ave., Cambridge, MA 02142, USA

[74] Google Research, 355 Main St., Cambridge, MA 02142, USA
[75] Institut für Theoretische Physik und Astrophysik, Universität Würzburg, Emil-Fischer-Str. 31, D-97074 Würzburg, Germany
[76] Department of History of Science, Harvard University, Cambridge, MA 02138, USA
[77] Department of Physics, Harvard University, Cambridge, MA 02138, USA
[78] CP3-Origins, University of Southern Denmark, Campusvej 55, DK-5230 Odense M, Denmark
[79] Instituto Nacional de Astrofísica, Óptica y Electrónica, Apartado Postal 51 y 216, 72000. Puebla Pue., México
[80] Consejo Nacional de Ciencia y Tecnologìa, Av. Insurgentes Sur 1582, 03940, Ciudad de México, México
[81] Instituto de Astrofísica de Andalucía-CíSIC, Glorieta de la Astronomía s/n, E-18008 Granada, Spain
[82] Key Laboratory for Research in Galaxies and Cosmology, Chinese Academy of Sciences, Shanghai 200030, People's Republic of China
[83] NOVA Sub-mm Instrumentation Group, Kapteyn Astronomical Institute, University of Groningen, Landleven 12, 9747 AD Groningen, The Netherlands
[84] Department of Astronomy, School of Physics, Peking University, Beijing 100871, People's Republic of China
[85] Kavli Institute for Astronomy and Astrophysics, Peking University, Beijing 100871, People's Republic of China
[86] Department of Astronomy, Graduate School of Science, The University of Tokyo, 7-3-1 Hongo, Bunkyo-ku, Tokyo 113-0033, Japan
[87] The Institute of Statistical Mathematics, 10-3 Midori-cho, Tachikawa, Tokyo, 190-8562, Japan
[88] Department of Statistical Science, The Graduate University for Advanced Studies (SOKENDAI), 10-3 Midori-cho, Tachikawa, Tokyo 190-8562, Japan
[89] Kavli Institute for the Physics and Mathematics of the Universe, The University of Tokyo, 5-1-5 Kashiwanoha, Kashiwa, 277-8583, Japan
[90] Leiden Observatory, Leiden University, Postbus 2300, 9513 RA Leiden, The Netherlands
[91] ASTRAVEO LLC, P.O. Box 1668, Gloucester, MA 01931, USA
[92] Institute for Astrophysical Research, Boston University, 725 Commonwealth Ave., Boston, MA 02215, USA
[93] Institute for Cosmic Ray Research, The University of Tokyo, 5-1-5 Kashiwanoha, Kashiwa, Chiba 277-8582, Japan
[94] Joint Institute for VLBI ERIC (JIVE), Oude Hoogeveensedijk 4, 7991 PD Dwingeloo, The Netherlands
[95] Department of Astronomy and Atmospheric Sciences, Kyungpook National University, Daegu 702-701, Republic of Korea
[96] Kogakuin University of Technology & Engineering, Academic Support Center, 2665-1 Nakano, Hachioji, Tokyo 192-0015, Japan
[97] Niigata University, 8050 Ikarashi-nino-cho, Nishi-ku, Niigata 950-2181, Japan
[98] Physics Department, National Sun Yat-Sen University, No. 70, Lien-Hai Road, Kaosiung City 80424, Taiwan, R.O.C.
[99] National Optical Astronomy Observatory, 950 N. Cherry Ave., Tucson, AZ 85719, USA
[100] Department of Physics, The Chinese University of Hong Kong, Shatin, N. T., Hong Kong
[101] School of Astronomy and Space Science, Nanjing University, Nanjing 210023, People's Republic of China
[102] Key Laboratory of Modern Astronomy and Astrophysics, Nanjing University, Nanjing 210023, People's Republic of China
[103] INAF-Istituto di Radioastronomia, Via P. Gobetti 101, I-40129 Bologna, Italy
[104] Department of Physics, National Taiwan University, No.1, Sect. 4, Roosevelt Rd., Taipei 10617, Taiwan, R.O.C
[105] Instituto de Radioastronomía y Astrofísica, Universidad Nacional Autónoma de México, Morelia 58089, México
[106] Instituto de Astronomía, Universidad Nacional Autónoma de México, CdMx 04510, México
[107] Key Laboratory of Radio Astronomy, Chinese Academy of Sciences, Nanjing 210008, People's Republic of China
[108] Yunnan Observatories, Chinese Academy of Sciences, 650011 Kunming, Yunnan Province, People's Republic of China
[109] Center for Astronomical Mega-Science, Chinese Academy of Sciences, 20A Datun Road, Chaoyang District, Beijing, 100012, People's Republic of China
[110] Key Laboratory for the Structure and Evolution of Celestial Objects, Chinese Academy of Sciences, 650011 Kunming, People's Republic of China
[111] Anton Pannekoek Institute for Astronomy, University of Amsterdam, Science Park 904, 1098 XH, Amsterdam, The Netherlands
[112] Gravitation and Astroparticle Physics Amsterdam (GRAPPA) Institute, University of Amsterdam, Science Park 904, 1098 XH Amsterdam, The Netherlands
[113] School of Natural Sciences, Institute for Advanced Study, 1 Einstein Drive, Princeton, NJ 08540, USA
[114] Science Support Office, Directorate of Science, European Space Research and Technology Centre (ESA/ESTEC), Keplerlaan 1, 2201 AZ Noordwijk, The Netherlands
[115] School of Physics and Astronomy, Shanghai Jiao Tong University, 800 Dongchuan Road, Shanghai, 200240, People's Republic of China
[116] Institut de Radioastronomie Millimétrique, IRAM, Avenida Divina Pastora 7, Local 20, E-18012, Granada, Spain
[117] National Institute of Technology, Hachinohe College, 16-1 Uwanotai, Tamonoki, Hachinohe City, Aomori 039-1192, Japan
[118] South African Radio Astronomy Observatory, Observatory 7925, Cape Town, South Africa
[119] Department of Physics, National and Kapodistrian University of Athens, Panepistimiopolis, GR 15783 Zografos, Greece
[120] Sejong University, 209 Neungdong-ro, Gwangjin-gu, Seoul, Republic of Korea
[121] Instituto de Astronomía, Universidad Nacional Autónoma de México (UNAM), Apdo Postal 70-264, Ciudad de México, México
[122] EACOA Fellow
[123] Canadian Institute for Theoretical Astrophysics, University of Toronto, 60 St. George Street, Toronto, ON M5S 3H8, Canada
[124] Dunlap Institute for Astronomy and Astrophysics, University of Toronto, 50 St. George Street, Toronto, ON M5S 3H4, Canada
[125] Canadian Institute for Advanced Research, 180 Dundas St. W, Toronto, ON M5G 1Z8, Canada
[126] Radio Astronomy Laboratory, University of California, Berkeley, CA 94720, USA
[127] Department of Physics, University College Cork, Kane Building, College Road, Cork T12 K8AF, Ireland
[128] Department of Physics, National Taiwan Normal University, No. 88, Sec. 4, Tingzhou Rd., Taipei 116, Taiwan, R.O.C.
[129] Center of Astronomy and Gravitation, National Taiwan Normal University, No. 88, Sec. 4, Tingzhou Road, Taipei 116, Taiwan, R.O.C.
[130] Gemini Observatory, 670 N. A'ohoku Place, Hilo, HI 96720, USA
[131] Frankfurt Institute for Advanced Studies, Ruth-Moufang-Strasse 1, D-60438 Frankfurt, Germany
[132] School of Mathematics, Trinity College, Dublin 2, Ireland
[133] Hiroshima Astrophysical Science Center, Hiroshima University, 1-3-1 Kagamiyama, Higashi-Hiroshima, Hiroshima 739-8526, Japan
[134] Aalto University, Department of Electronics and Nanoengineering, PL 15500, FI-00076 Aalto, Finland
[135] Department of Astronomy, Yonsei University, Yonsei-ro 50, Seodaemun-gu, 03722 Seoul, Republic of Korea
[136] Netherlands Organisation for Scientific Research (NWO), Postbus 93138, 2509 AC Den Haag, The Netherlands
[137] Department of Physics and Astronomy, Seoul National University, Gwanak-gu, Seoul 08826, Republic of Korea
[138] University of New Mexico, Department of Physics and Astronomy, Albuquerque, NM 87131, USA
[139] Jeremiah Horrocks Institute, University of Central Lancashire, Preston PR1 2HE, UK
[140] Physics Department, Brandeis University, 415 South Street, Waltham, MA 02453, USA
[141] Tuorla Observatory, Department of Physics and Astronomy, University of Turku, Finland
[142] Radboud Excellence Fellow of Radboud University, Nijmegen, The Netherlands
[143] Princeton Gravity Initiative, Princeton University, Princeton, NJ 08544, USA
[144] School of Physics, Huazhong University of Science and Technology, Wuhan, Hubei, 430074, People's Republic of China
[145] Mullard Space Science Laboratory, University College London, Holmbury St. Mary, Dorking, Surrey, RH5 6NT, UK
[146] School of Astronomy and Space Sciences, University of Chinese Academy of Sciences, No. 19A Yuquan Road, Beijing 100049, People's Republic of China

[147] Astronomy Department, University of Science and Technology of China, Hefei 230026, People's Republic of China
[148] Bard College, 30 Campus Road, Annandale-on-Hudson, NY 12504, USA
Received 2022 February 5; revised 2022 March 25; accepted 2022 March 25; published 2022 May 12

Abstract

The Event Horizon Telescope (EHT) observed the compact radio source, Sagittarius A* (Sgr A*), in the Galactic Center on 2017 April 5–11 in the 1.3 mm wavelength band. At the same time, interferometric array data from the Atacama Large Millimeter/submillimeter Array and the Submillimeter Array were collected, providing Sgr A* light curves simultaneous with the EHT observations. These data sets, complementing the EHT very long baseline interferometry, are characterized by a cadence and signal-to-noise ratio previously unattainable for Sgr A* at millimeter wavelengths, and they allow for the investigation of source variability on timescales as short as a minute. While most of the light curves correspond to a low variability state of Sgr A*, the April 11 observations follow an X-ray flare and exhibit strongly enhanced variability. All of the light curves are consistent with a red-noise process, with a power spectral density (PSD) slope measured to be between −2 and −3 on timescales between 1 minute and several hours. Our results indicate a steepening of the PSD slope for timescales shorter than 0.3 hr. The spectral energy distribution is flat at 220 GHz, and there are no time lags between the 213 and 229 GHz frequency bands, suggesting low optical depth for the event horizon scale source. We characterize Sgr A*'s variability, highlighting the different behavior observed just after the X-ray flare, and use Gaussian process modeling to extract a decorrelation timescale and a PSD slope. We also investigate the systematic calibration uncertainties by analyzing data from independent data reduction pipelines.

Unified Astronomy Thesaurus concepts: Black holes (162); Galactic Center (565); Radio interferometry (1346)

1. Introduction

Several years after its initial identification (Balick & Brown 1974), the radio source at the center of our Galaxy, now associated with the supermassive black hole Sagittarius A* (Sgr A*), was discovered to be significantly variable at radio frequencies (Brown & Lo 1982). Variations of tens of percent over year-long timescales had been recognized, with convincing evidence for variability on timescales of $\gtrsim$1 day, and factor of four variations occurring on timescales $\lesssim$10 days (Wright & Backer 1993). It was noted that "flickering noise" was certainly possible on shorter timescales as well (Brown & Lo 1982).

After Chandra's discovery of rapid X-ray flares from Sgr A* (Baganoff et al. 2001), however, many of the subsequent studies of its multiwavelength variability focused on impulsive events, where the flux could grow by a factor of several tens on short timescales. The first observed X-ray flare had a duration ≈10 ks (Baganoff et al. 2001), i.e., the light-crossing time for a diameter of $\approx 500\,GM/c^2$, or roughly the orbital timescale at $\approx 20\,GM/c^2$ for a Schwarzschild black hole given the $\sim 4 \times 10^6\,M_\odot$ mass of Sgr A* (Ghez et al. 2008; Gillessen et al. 2009, 2017; Boehle et al. 2016; Gravity Collaboration et al. 2018a, 2019; Do et al. 2019a). All subsequently observed X-ray flares (see, e.g., Porquet et al. 2003; Neilsen et al. 2013, 2015; Li et al. 2015; Ponti et al. 2015; Yuan & Wang 2016; Bouffard et al. 2019; Haggard et al. 2019) have occurred on timescales ranging from 0.4 to 10 ks, with the short timescale being limited by counting statistics, and longer flares apparently being absent from the data (Neilsen et al. 2013, 2015).

Similar impulsive variability at other wavelength bands—millimeter/submillimeter (mm/submm) and infrared (IR)—have also steered variability studies of Sgr A*, especially because the first detected IR variability occurred on the short orbital timescales of the inner regions (Genzel et al. 2003; Ghez et al. 2004). The parallels to the X-ray flares have led to a strong focus on studying the flare/radiation mechanism and the relationship between the different wave bands. For cases where flares were observed simultaneously in both IR and X-ray light curves, the IR variability was not delayed from the X-ray by more than ∼10–15 minutes (Eckart et al. 2004, 2006; Marrone et al. 2008). This suggests that the IR emission and X-ray emission predominantly arise from the same regions. The most recent and comprehensive analysis of X-ray-to-IR variability is consistent with no delay at 99.7% confidence, but at 68% confidence, it allows for a 10-to-20-minute delay of the IR (Boyce et al. 2019). Multiwavelength lags including the mm and submm are more complex. The mm flux density maxima typically have a far lower relative flux density gain than flares at higher frequencies and are often delayed by 1–2 hr (Yusef-Zadeh et al. 2008; Eckart et al. 2012), although Marrone et al. (2008) and Witzel et al. (2021) report delays as short as 20–30 minutes and Fazio et al. (2018) report a flare with a negligible mm–IR lag. The lack of high-fidelity mm light curves and the sparse sampling compared to the IR and X-ray have limited detailed variability and cross-correlation studies, and it has been suggested that the perceived delays between mm and IR/X-ray may in fact just be coincidental (Capellupo et al. 2017).

Recently, the increase in quality of the Sgr A* IR light curves has allowed one to go beyond the studies of individual flare events and led to more detailed statistical and variability modeling over a wide range of timescales, spanning minutes to hours. Various groups have characterized the IR light curves with a red-noise Fourier power spectral density (PSD; approximately $\propto f^{-2}$) on timescales longer than a few minutes, with a break to a flat, white-noise PSD on timescales longer than ≈3 hr (Do et al. 2009; Meyer et al. 2009). Consideration of the shortest timescales has mostly been limited by the signal-to-noise ratio (S/N). Equivalently, the structure function (SF) analyses have revealed a similar result: variances consistent with the unstructured white noise on timescales longer than a few hours, and consistent with red noise on hour to minute timescales (Do et al. 2009; Witzel et al. 2018, 2021). Although periodic signals have been searched for in the IR light curves (e.g., Genzel et al. 2003), no convincing

signatures that could not instead be attributed to limited sampling of red noise have been found.

It has been only relatively recently that the quality of mm light curves for Sgr A* has begun to match that in the IR, such that a similar detailed analysis can be applied to describe the mm behavior of Sgr A* on timescales from minutes to hours. In particular, Dexter et al. (2014) have shown that, similar to the IR variability, mm light curves indicate red-noise characteristics, with a break to white noise on longer timescales. Additionally, detailed studies of the Sgr A* mm and submm emission have been enabled by high-S/N observations using the Atacama Large Millimeter/submillimeter Array (ALMA; Bower et al. 2015, 2018, 2019; Brinkerink et al. 2015) and the Submillimeter Array (SMA; Bower et al. 2015; Fazio et al. 2018; Witzel et al. 2021). Further, short-timescale variability of Sgr A* mm ALMA light curves has been analyzed by Iwata et al. (2020), based on 10 epochs with a duration of 70 minutes.

In this work, we present the detailed analysis of ALMA and SMA light curves of Sgr A* obtained during the observing campaign of the Event Horizon Telescope (EHT; Event Horizon Telescope Collaboration et al. 2022a, 2022b, 2022c, 2022d, 2022e, and 2022f, hereafter Papers I, II, III, IV, V, and VI) on 2017 April 5–11. These observations consist of 5 days of SMA monitoring and 3 days of ALMA monitoring of the source for 3–10 hr each day. They constitute a uniquely long, homogeneously processed, high-cadence and high-S/N mm Sgr A* light-curve data set. We compare these observations with the historic data available at 230 GHz. During the 2017 EHT observations, Sgr A* was mostly in a low variability state, with slowly varying mm flux density of 2–3 Jy. However, on 2017 April 11, ALMA observations immediately followed a 5.5 ks X-ray flare seen by Chandra, peaking at about 8.8 UT (Paper II). The mm variability on that day was strongly enhanced, with the flux density growing by about 50% and reaching a maximum at about 10.98 UT, 2.2 hr after the X-ray peak.

This paper is organized as follows. In Section 2, we discuss the observations and nonstandard data reduction procedures dedicated to extracting the compact source emission from the phased array data. Section 3 discusses overall data properties and consistency between individual data sets, as well as the spectral index measurements. In Section 4, we compare the new observations with the archival mm data sets and characterize the variability of the light curves with correlations and SFs. We then model the data using Gaussian process (GP) models in Section 5. In Section 6, we discuss the PSDs and search for statistically significant periodicity signatures in the data. Finally, we summarize and discuss the full results in Section 7.

2. Observations and Data Reduction

The EHT observed Sgr A* in April 2017 with a very long baseline interferometry (VLBI) array of eight stations at six distinct geographic locations (Event Horizon Telescope Collaboration et al. 2019a, 2019b, hereafter M87* Papers I and II).[149] A detailed analysis of the VLBI observations of Sgr A* on 2017 April 6 and 7 is presented in Papers I, II, III, IV, V, and VI. Two of the participating EHT stations are connected interferometers, formed by the coherent combination of their elements: SMA located on Maunakea (Hawai'i, USA), and ALMA located on the Chajnantor plateau (Atacama Desert, Chile). An advantage of using connected-element interferometers as EHT stations, besides the enhanced sensitivity of the resulting array, is that it is possible to compute the coherency matrices among their connected elements simultaneously with the summed signals that are recorded for their later use in VLBI (Goddi et al. 2019). Therefore, as a by-product of EHT VLBI observations, we can make use of the connected-element visibilities to obtain Sgr A* light curves with long duration, high cadence, and high S/N. Apart from their standalone scientific value, the light-curve products are also employed downstream in the EHT VLBI data calibration; see Appendix A.

Utilizing observations in the VLBI mode to produce Sgr A* light curves allows us to access the particularly long observing windows needed for the VLBI aperture synthesis, at the cost of using a phased array in a compact configuration with relatively low resolution and observing the source partly at an unusually low elevation. Since this is a nonstandard procedure that could be employed for similar observations in the future, in this paper we dedicate some additional effort to addressing the comparisons between data reduction pipelines and to recommending procedures for future VLBI observing campaigns.

The ALMA observations were carried out across four frequency subbands (spectral windows), each with a bandwidth of 2 GHz, centered at 213.1 and 215.1 GHz (B1 and B2, lower sideband) and 227.1 and 229.1 GHz (LO and HI, upper sideband). ALMA observed Sgr A* on 2017 April 6, 7, and 11, typically with ∼37 dishes of 12 m diameter in the phased array, with 4–10 hr tracks; see Table 1. The integration time used by the ALMA correlator was set to 4 s. Due to the array phasing requirements, ALMA observed in a compact configuration, with the longest projected baselines reaching 160 m on 2017 April 6, 278 m on 2017 April 7, and 374 m on 2017 April 11.

The use of the VLBI phased array mode at ALMA has several implications for the data properties and calibration procedures, as compared to standard ALMA observations (Matthews et al. 2018; Goddi et al. 2019). In order to perform a proper VLBI polarization conversion of the ALMA signal streams (using the `PolConvert` program; Martí-Vidal et al. 2016), the official ALMA reduction scripts needed to be adapted in such a way that their final products are not ready for scientific use of the ALMA-only data. In particular (Goddi et al. 2019):

1. The ALMA phasing efficiency has to be computed at each integration time of the correlator, using the same subset of antennas that are present in the VLBI signal, regardless of the data quality of each phased element, as well as of any other factor that would imply the removal of the data under normal circumstances (e.g., shadowing among antennas). Therefore, low-quality data cannot be edited before the calibration, hence degrading the final product.
2. The system temperatures of each individual antenna are not applied to the calibration tables. Instead, a global system temperature is computed and applied to the summed signal. The effects of atmospheric opacity are computed from the overall system temperatures and then stored in the VLBI metadata. As a consequence, the

[149] All EHT M87* papers (Event Horizon Telescope Collaboration et al. 2019a, 2019b, 2019c, 2019d, 2019e, 2019f) will be hereafter referred to as M87* Papers I, II, III, IV, V, and VI, respectively.

Table 1
Sgr A* Light Curves Presented in This Paper

Array	Reduction	Band (GHz)	Day in 2017	t_{start} UT (hr)	t_{stop} UT (hr)	Duration (hr)	Samples	Flux $\mu \pm \sigma$ (Jy)	Modulation σ/μ	max–min (Jy)
ALMA	A1	B1	Apr 6	8.40	14.15	5.75	2226	2.59 ± 0.11	0.042	0.57
	cadence: 4 s	212.1–214.1	Apr 7	4.39	14.07	9.68	3549	2.34 ± 0.16	0.068	0.68
	min. elev.: 25°		Apr 11	9.00	13.09	4.09	1663	2.44 ± 0.31	0.127	1.16
	S/N ∼ 1300	B2	Apr 6	8.40	14.15	5.75	2232	2.59 ± 0.11	0.042	0.56
		214.1–216.1	Apr 7	4.39	14.07	9.68	3541	2.34 ± 0.16	0.068	0.65
			Apr 11	9.00	13.10	4.10	1654	2.43 ± 0.31	0.128	1.20
		LO	Apr 6	8.40	14.15	5.75	2222	2.50 ± 0.09	0.036	0.51
		226.1–228.1	Apr 7	4.39	14.07	9.68	3507	2.26 ± 0.16	0.071	0.69
			Apr 11	9.00	13.09	4.09	1645	2.31 ± 0.29	0.126	1.25
		HI	Apr 6	8.40	14.15	5.75	2222	2.59 ± 0.11	0.042	0.57
		228.1–230.1	Apr 7	4.39	14.07	9.68	3488	2.33 ± 0.16	0.067	0.72
			Apr 11	9.00	13.09	4.09	1624	2.40 ± 0.31	0.129	1.27
	A2	B1	Apr 6	8.40	13.75	5.35	519	2.48 ± 0.12	0.048	0.49
	cadence: 18 s	212.1–214.1	Apr 7	4.93	13.57	8.64	785	2.32 ± 0.12	0.052	0.56
	min. elev.: 30°		Apr 11	9.00	13.15	4.15	461	2.11 ± 0.25	0.118	0.95
	S/N ∼ 400	B2	Apr 6	8.40	13.75	5.35	519	2.49 ± 0.12	0.048	0.49
		214.1–216.1	Apr 7	4.93	13.57	8.64	785	2.33 ± 0.12	0.052	0.57
			Apr 11	9.00	13.15	4.15	460	2.12 ± 0.25	0.118	0.95
		LO	Apr 6	8.40	13.75	5.35	519	2.41 ± 0.12	0.050	0.49
		226.1–228.1	Apr 7	4.93	13.57	8.64	786	2.23 ± 0.12	0.054	0.56
			Apr 11	9.00	13.15	4.15	371	2.12 ± 0.21	0.099	0.93
		HI	Apr 6	8.40	13.75	5.35	518	2.51 ± 0.13	0.052	0.51
		228.1–230.1	Apr 7	4.93	13.57	8.64	786	2.32 ± 0.12	0.052	0.59
			Apr 11	9.00	13.15	4.15	331	2.22 ± 0.21	0.095	0.98
SMA	SM	LO	Apr 5	11.30	15.71	4.41	165	2.48 ± 0.14	0.056	0.66
	cadence: 62 s	226.1–228.1	Apr 6	11.24	14.54	3.30	148	2.59 ± 0.08	0.031	0.41
	min. elev.: 15°		Apr 7	11.17	15.59	4.42	199	2.29 ± 0.11	0.048	0.46
	S/N ∼ 60		Apr 10	10.98	14.77	3.79	157	2.50 ± 0.12	0.048	0.54
			Apr 11	10.92	15.00	4.09	188	2.60 ± 0.29	0.112	0.88
		HI	Apr 5	11.30	15.71	4.41	165	2.49 ± 0.15	0.060	0.69
		228.1–230.1	Apr 6	11.24	14.54	3.30	148	2.62 ± 0.08	0.031	0.43
			Apr 7	11.17	15.59	4.42	199	2.30 ± 0.12	0.052	0.47
			Apr 10	10.98	14.77	3.79	157	2.50 ± 0.12	0.048	0.55
			Apr 11	10.92	15.00	4.09	188	2.62 ± 0.29	0.111	0.90
FULL	ALMA+SM	LO	Apr 5–11	⋯	⋯	147.70	7874	2.36 ± 0.22	0.094	1.37
FULL	ALMA+SM	HI	Apr 5–11	⋯	⋯	147.70	7834	2.44 ± 0.23	0.094	1.44

Note. μ and σ denote signal mean and standard deviation, respectively.

opacity correction is provided in the VLBI metadata, but it is not present in the ALMA-only calibrated visibilities.

3. In ordinary ALMA observations, amplitude calibration uses a primary flux density calibrator, e.g., a solar system object or a monitored quasar. The calibration is then extrapolated to the secondary calibrator and bootstrapped into the target. However, when working in VLBI mode, we need to self-calibrate each ALMA subscan (16 s segment), which implies the need to use an a priori (constant) model for the flux density of Sgr A*.

These limitations in the official quality assurance (QA2) calibration of the ALMA VLBI observations can be overcome with the development of independent calibration scripts, which have to handle the aforementioned peculiarities of the ALMA phasing system. In an attempt to further limit and characterize the influence of the systematic calibration errors on the analysis, we have corrected the limitations of the QA2 calibration of the Sgr A* observations using two independent procedures (A1 and A2), described in more detail in the following subsections, along with the SMA data reduction procedures. We consider the A1 pipeline to be the most self-consistent and reliable, given the robust assumption of a lack of structural variability of a parsec-scale image on a timescale of several days, enabling the time-dependent self-calibration of the amplitude gains. Nevertheless, comparing the two pipelines offers a valuable insight into the potential systematic errors corrupting mm light-curve observations. These effects are quantified and discussed in Section 3.

The SMA observations were carried out across eight subbands, each with a bandwidth of 2 GHz, covering a range of frequencies between 208.1 and 232.1 GHz. In this paper, we

focus on the 227.1 and 229.1 GHz bands (LO and HI, respectively), corresponding to the two bands used for the VLBI observations with the EHT in 2017 (M87* Paper II; M87* Paper III). The light curves from the other frequency subbands are very consistent and are summarized in Appendix B. The SMA observed Sgr A* on 2017 April 5–11, with shorter observing tracks lasting 3.3–4.4 hr, starting at a later time when compared to ALMA. The SMA observed the source with six to seven dishes of 6 m diameter and a correlator integration step of 10.4 s.

For both stations, observations were arranged into scans lasting typically 5–10 minutes, interleaved with observations of calibrators (Paper II). The Sgr A* light-curve data sets analyzed in this paper are summarized in Table 1.

2.1. A1: Intrafield Flux Density ALMA Calibration

The Sgr A* image field of view can be split into two components at angular scales of arcseconds probed by ALMA:

1. An extended structure with a low brightness temperature, primarily originating from thermal emission from ionized gas and dust infalling into the central region of the Galaxy, the so-called "minispiral" (e.g., Lo & Claussen 1983; Goddi et al. 2021). From our ALMA observations, the integrated extended flux density of the minispiral is ∼1.1 Jy. Given the physical origin of this emission and the spatial scales involved (several tens of parsecs), we can assume the brightness distribution of the minispiral to remain constant during the few days of the EHT observing campaign.
2. An unresolved and highly variable component corresponding to the compact source Sgr A*, with a flux density typically ranging between 2 and 5 Jy at 230 GHz.

With the superb sensitivity of ALMA (M87* Paper III; Paper II) and the sufficiently high integrated extended flux density of the minispiral, it is possible to detect the whole field-of-view structure (i.e., the minispiral plus Sgr A*) in each ALMA 4 s snapshot. Therefore, one can assume a two-component Fourier domain model, $V_t^{\rm mod}$, composed of (1) $\mathcal{F}^e$, a Fourier transform of the static extended minispiral, F^e, corrupted with a time-dependent amplitude gain, G_t, accounting for atmospheric and instrumental effects (following the QA2 calibration, these effects can be modeled with a single function of time, representing the effective gain of the interferometric array); and (2) F_t, an unresolved Sgr A* compact component with a time-dependent flux density (still corrupted by the G_t gain at this stage), so

$$V_t^{\rm mod} = G_t \mathcal{F}^e + F_t. \quad (1)$$

If we denote the visibility observed at a time t on a baseline i as $V_{i,t}^{\rm obs}$ and the model sampled at the same Fourier plane location as $V_{i,t}^{\rm mod}$, the model can be fitted to the data by minimizing

$$\chi^2_t(G_t, F_t) = \sum_i \omega_{i,t} \, |V_{i,t}^{\rm obs} - V_{i,t}^{\rm mod}|^2 \quad (2)$$

for each time t, with S/N-based baseline weights, $\omega_{i,t}$, and the summation extending over all baselines available at a given time t (Martí-Vidal et al. 2014).

Since the true integrated flux density of the minispiral is assumed to be constant, we can use the values of G_t to remove the residual corruption effects in the Sgr A* flux density estimates, F_t. Hence, we produce a corrected estimate of the Sgr A* flux density, F_t^c, using the equation

$$F_t^c = \frac{F_t}{G_t}. \quad (3)$$

In practice, we also need to solve for the image domain minispiral model, F^e. We use the CLEAN algorithm (e.g., Högbom 1974) implemented in the Common Astronomy Software Application (CASA) framework (McMullin et al. 2007) as the `tclean` task, iteratively reconstructing the image of the minispiral, recalibrating the data with G_t, and updating G_t and F_t. While the minispiral structure is assumed to be constant across observed frequencies, the absolute flux density scale is allowed to vary between the subbands. The procedure runs until convergence. The times with unphysical or unconverged (G_t, F_t) are flagged. Special attention is given to the minispiral total flux density, which is fixed per subband to the median of the flux densities estimated from all of the snapshots obtained throughout the EHT campaign.

In Figure 1, we show two model images of the field around Sgr A*; the left panel corresponds to the original QA2 calibrated data (the initial condition for the iterative procedure) and shows the complete source structure (minispiral and Sgr A*); the right panel is the final minispiral model obtained after the convergence of the intrafield calibration. The high noise level seen in the QA2 image (i.e., the artifacts that are distributed across the whole field of view) is due to the effects of the time variability of Sgr A*. By modeling the source variability with Equation (1), the noise level in the final minispiral image (Figure 1, right) is reduced. We notice that the size of the ALMA primary beam at 230 GHz is of the order of the size of the minispiral structure. This implies that different points across the image are affected by a different ALMA sensitivity. Only emission from regions with a primary-beam response >5% can be considered as detections above 5σ of the ALMA sensitivity. As we approach this primary-beam threshold, marked with a dashed line in Figure 1, the noise effects in the brightness distribution increase. Regions far from the phase center have a negligible contribution to the visibilities, since such a contribution also scales with the primary-beam response. The effects of these regions on the calibration of the Sgr A* light curves will thus be small.

In Figure 2, we show the visibility amplitudes for a representative ALMA snapshot from 2017 April 7, band B1. The contribution of the extended minispiral model (green crosses) at short baselines is clearly visible. As a final product, we obtain converged light curves of Sgr A* with a snapshot cadence of 4 s. Data corresponding to a source elevation below 25°, exhibiting significant quality loss, are flagged.

The time-dependent factor, G_t, can also be used to correct the amplitudes of the VLBI visibilities related to the phased ALMA. Based on Martí-Vidal et al. (2016), the scaling gain factor to correct ALMA amplitudes on VLBI baselines is $\sqrt{G_t}$. This approach has been employed for a priori amplitude calibration of the EHT VLBI Sgr A* data (see Appendix A and Paper II).

2.2. A2: SEFD-based ALMA Calibration

A custom script was prepared to process the nonstandard array data acquired during the phased ALMA observations of Sgr A* using measurements of the system equivalent flux density (SEFD) of each ALMA antenna. While similar to the

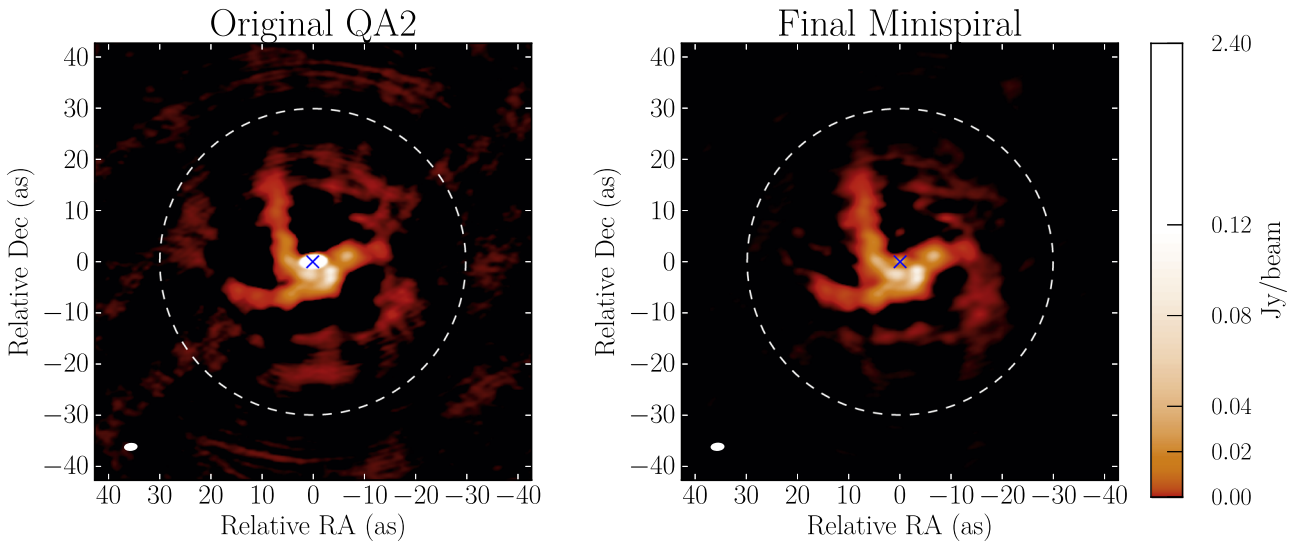

Figure 1. Left: an image of the Sgr A* field obtained from the original QA2 calibrated data, using natural weighting and a Gaussian taper in Fourier space to boost the sensitivity to the extended (minispiral) structure. Right: a final image of the minispiral, after applying the intrafield calibration and removing the signal from Sgr A*. In each panel, the convolving beam is shown in the lower left corner and the location of Sgr A* is marked with a cross. The dashed line marks the region where the primary-beam response of the ALMA antennas is above 5%.

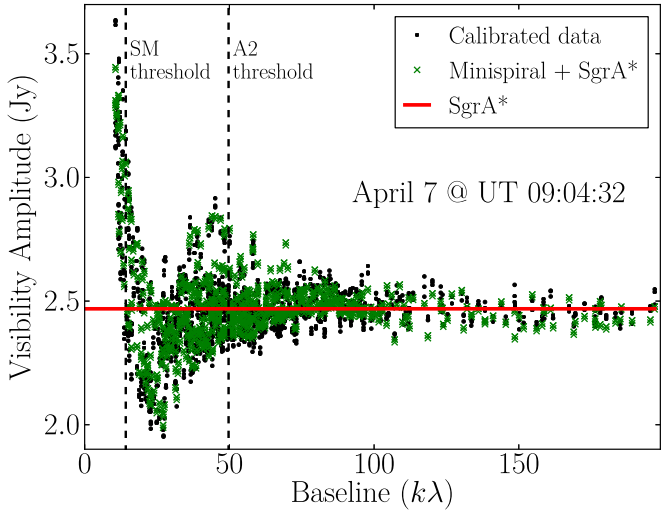

Figure 2. Calibrated visibility amplitudes of Sgr A* for band B1 on 2017 April 7 within a snapshot taken at 9:04:32 UT. The green crosses are the total model prediction (i.e., minispiral plus Sgr A*). The red line shows the instantaneous flux density of the compact unresolved Sgr A*. The vertical dashed lines indicate the flagging thresholds used in the A2 and SM pipelines.

standard ALMA QA2 pipeline, it includes additional calibration steps necessary to produce the time-dependent light-curve data. The ALMA observations are grouped in scans, which consist of subscans of 18 s cadence, with 16 s of correlated data (Goddi et al. 2019). A nearby phase calibrator, J1744–3116 (J1744–312), was observed for 30 s every 20 minutes. Observations of two bright quasars, NRAO 530 (J1733–1304, B1730–130) and J1924–2914 (B1921–293), were also included for the amplitude calibration; see Table 2. First, the phase delays associated with the atmospheric water vapor were estimated from measurements of the 183 GHz water line, performed with high time cadence using radiometers located at each ALMA antenna. The radiometer measurements allowed us to estimate the column of water vapor above each ALMA antenna, which were then converted into a phase correction related to the atmospheric optical path. Conversion from the relative visibility correlation amplitude to a flux density scale was performed by applying the system temperature measurements performed routinely at each antenna. The corrected data were concatenated and reduced to produce a single CASA measurement set (McMullin et al. 2007) for each observing day, containing relevant data for all four subbands.

Table 2
Calibrators Used in ALMA and SMA Data Reduction

Day	Bandpass	Flux	Gain
		ALMA A2[a]	
April 6	NRAO 530	NRAO 530	J1744–3116
April 7	NRAO 530	NRAO 530	J1744–3116
April 11	NRAO 530	NRAO 530	J1744–3116
		SMA	
April 5	3C 279	Callisto	NRAO 530 and J1924–2914
April 6	3C 273	Ganymede	NRAO 530 and J1924–2914
April 7	3C 454.3	Ganymede	NRAO 530 and J1924–2914
April 10	3C 279	Titan	1749+096
April 11	3C 279	Callisto	J1924–2914

Note.
[a] J1924–2914 was also used as a flux calibration consistency check.

The second step was the bandpass calibration of all of the frequency channels in each subband. We used NRAO 530 to generate the bandpass calibration tables, choosing a scan when the source was nearest to the zenith. The chosen reference antenna was located near the array center and not shadowed by neighboring antennas. Lower-sensitivity channels near the edges of each subband, as well as data from shadowed antennas, were flagged. Following bandpass calibration, all channels within each subband were averaged.

In the third step, we determined the amplitude scale of the observations on each day, and we applied the phase-referencing calibration. Since all three calibrators were observed as unresolved point sources, anomalously low amplitudes on some antennas were apparent. The few low-amplitude data

points, with less than about 70% of the nominal sensitivity of the majority of antennas, were subsequently flagged. Next, the flux density scale over the entire observation was set using NRAO 530 as a flux density calibrator, assuming a flux density of 1.56 Jy at 213.1 GHz and a spectral index of −0.72, obtained from the ALMA calibrator catalog.[150] The flux density calibration was applied using the average gain of the two polarizers of each antenna (*X* and *Y*), so that there was no gain bias caused by the source linear polarization.

The flux densities of the other two quasar calibrators were verified to be constant over each observation day to within a few percent. The last calibration step, phase referencing between J1744–3116 and Sgr A*, was performed by deriving the antenna-based phase for each J1744–3116 scan with the CASA task `gaincal` and then interpolated to each Sgr A* scan, which completed the calibration cycle.

The above steps provide calibrated complex visibilities from which an image containing a strong point source, Sgr A*, and the extended minispiral emission can be obtained. Since the phase calibrator J1744–3116 was observed only every 20 minutes, the interpolated phase correction can deviate from the true values. To determine the time variability of Sgr A* in the presence of extended emission and calibration phase errors, we first flag baselines shorter than 70 m (about 50 kλ; Figure 2). Since virtually all of the extended emission is resolved out on longer baselines, the remaining data are reasonably consistent with a point-source model, although its position may vary in time. Subsequently, given a large number of available long baselines, we perform phase self-calibration to remove the residual phase errors remaining after the calibration with J1744–3116. The phase self-calibration algorithm determines phase corrections for each antenna and time segment, producing a set of visibilities consistent with a point source at a fixed location.

We then reconstruct CLEAN (Högbom 1974) images corresponding to the phase self-calibrated long-baseline data on timescales of individual subscans. These images correspond to a near-perfect point source with a flux density equal to that of Sgr A* at each short time period. The relevant flux density and error estimates were obtained by fitting the CLEAN image using the CASA task `imfit`. The sequence of these short-time flux density measurements defines the time-dependent light curve of Sgr A* for each observing day. Finally, data corresponding to source elevations below 30° were found to be of poor quality and self-consistency and were subsequently flagged in the final data set.

2.3. SM: SMA Calibration and Reduction

An initial pass through the SMA data was performed with a custom MATLAB[151] based reduction pipeline, primarily responsible for preliminary flagging and bandpass calibration. Bandpass calibration was performed using various bright calibrators, given in Table 2. After these steps, the bandpass corrections were applied to the data, after which they were spectrally averaged down by a factor of 128, to a channel resolution of 17.875 MHz.

After averaging, a second round of bandpass solving was performed, and the solutions were inspected to verify that the gain corrections were consistent with unity (as the data had already been bandpass corrected). The absolute flux density scale was set by using the flux density calibrator observed closest to the time of the Sgr A* observations, also noted in Table 2, using the Butler–JPL–Horizons 2012 models,[152] on a spectral-window-by-spectral-window basis. Next, amplitude gains for individual antennas were derived using bright quasars, NRAO 530 and J1924–2914. Analysis of the gain solutions showed that the most significant trends are correlated with the elevation of the gain calibrator, consistently with known issues with antenna pointing on the SMA at very low elevations (∼15°; data corresponding to lower elevations were flagged). In light of this, gain amplitudes were interpolated using a third-order polynomial fitted based on the elevation of Sgr A*, with the median amplitude elevation-dependent correction below 25° being approximately 5%.

Due to the rapid fluctuations in the instrumental phase arising from the real-time phasing loop used in VLBI beam forming, the first three integrations (≈30 s in total) were flagged whenever the telescopes moved onto Sgr A* from a calibrator source. Additionally, due to strong line absorption, presumably arising from CN foreground absorption (see Appendix H.1. of Goddi et al. 2021), spectral channels between 226.6 and 227.0 GHz were flagged.

After amplitude-only gain calibration and the aforementioned flagging, a round of phase-only gains were derived and applied using self-calibration of Sgr A* itself. Data for these observations were collected while the array was in a compact configuration including baselines with lengths spanning ∼5–50 kλ, which at 230 GHz are sensitive to structures up to ∼20″ in size, picking up extended minispiral emission surrounding Sgr A*. Examination of the SMA data shows a strong uptick in visibility amplitudes at (*u*, *v*)-distances below 15 kλ (about 20 m). Therefore, visibilities from shorter baselines are flagged prior to self-calibration and further analysis. The remaining long-baseline data are mostly sensitive to the flux density from the unresolved Sgr A* point source; see Figure 2.

Once phase self-calibration corrections were applied, an Sgr A* light curve was generated by taking the naturally weighted vector average of all baselines, for each spectral window observed by the SMA. The resultant light curves were evaluated for large fluctuations in amplitude, under the assumption that, over a 30 s interval, changes in the brightness of Sgr A* should be subdominant to the instrumental noise. Where fluctuations greater than 3σ were seen, the measurement in question was flagged, with the total volume of data flagged in this way amounting to ∼ 1%. Finally, to help improve the S/N of the data, they were time-averaged over 62 s intervals (six integration steps).

3. Data Consistency and Spectral Index

The light curves from all three reduction pipelines, corresponding to the HI band (229.1 GHz) on 2017 April 6, 7, and 11, are shown in Figure 3. There is overall agreement of the data features between pipelines. As a preliminary step of the analysis, we quantify the data sets' consistency and investigate any potential systematic discrepancies.

[150] https://almascience.eso.org/alma-data/calibrator-catalogue

[151] Mathworks, Version 2019b; http://www.mathworks.com/products/matlab/.

[152] ALMA Memo #594.

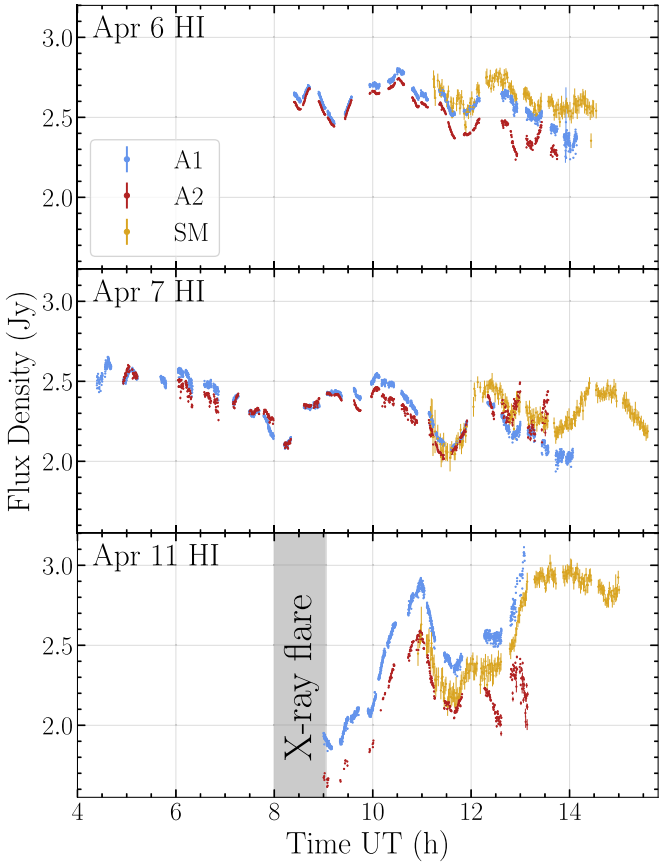

Figure 3. Sgr A* light curves obtained with ALMA (A1 and A2) and SMA (SM), in the HI band (229.1 GHz) using the reduction pipelines described in Section 2. The differences between light curves originating from different pipelines are strongly dominated by the systematic calibration errors, rather than by the thermal uncertainties.

3.1. Consistency between Instruments and Pipelines

The data sets were correlated through a Locally Normalized Discrete Correlation Function (LNDCF), as defined by Lehar et al. (1992), which revised the standard algorithm proposed by Edelson & Krolik (1988),

$$\mathrm{LNDCF}(\Delta t) = \frac{1}{M_{\Delta t}} \sum_{i,j} \frac{(a_i - \bar{a}_{\Delta t})(b_j - \bar{b}_{\Delta t})}{\sqrt{(\sigma^2{}_{a\Delta t} - e_a^2)(\sigma^2{}_{b\Delta t} - e_b^2)}}, \quad (4)$$

where a_i and b_j indicate the flux density measurements of the two compared data sets, e_a and e_b refer to the estimated measurement errors, and $M_{\Delta t}$ represents the number of data pairs contributing to the lag bin, Δt. The flux density means and standard deviations, $\bar{a}_{\Delta t}$, $\bar{b}_{\Delta t}$, $\sigma_{a\Delta t}$, $\sigma_{b\Delta t}$, are calculated for each lag, Δt, using exclusively the flux density measurements that contribute to the calculation of the LNDCF(Δt). As a comparison between the data sets, we compute the LNDCF(0) $\equiv$ LNDCF$_0$, presented in Table 3.

The correlation is generally high between the two ALMA pipelines, A1 and A2, with values higher than 0.8 on each individual day and band. It remains larger than 0.7 if we consider full light curves formed by joining the individual days. Similarly, there is a rather high correlation between the SMA data set and the ALMA pipeline A1, reaching above 0.75 in all cases. The correlation is less satisfactory between the A2 pipeline and the SMA, dropping below 0.5 in some cases on

Table 3
LNDCF$_0$ Coefficient Calculated between Selected Sgr A* Data Sets

Band	Apr 6	Apr 7	Apr 11	Joined
		A1–A2		
B1	0.85	0.89	0.96	0.76
B2	0.84	0.87	0.95	0.76
LO	0.81	0.87	0.91	0.74
HI	0.87	0.83	0.92	0.72
		A1–SM		
LO	0.83	0.93	0.99	0.80
HI	0.87	0.76	0.99	0.77
		A2–SM		
LO	0.38	0.97	0.45	0.66
HI	0.59	0.90	0.44	0.67

Table 4
Ratio of the Median Flux Densities in the Overlapping Observing Periods

Band	Apr 6	Apr 7	Apr 11	Joined
		A2/A1		
B1	0.96	1.00	0.86	0.95
B2	0.96	1.00	0.87	0.95
LO	0.96	0.99	0.91	0.95
HI	0.97	1.00	0.91	0.96
		SM/A1		
LO	1.05	1.08	0.94	1.03
HI	1.03	1.05	0.92	1.00
		SM/A2		
LO	1.13	1.06	1.10	1.09
HI	1.10	1.03	1.08	1.05

2017 April 6 and 11, but remaining high for the longest and most informative light curve from 2017 April 7. Some discrepancies between A2 and SM can be directly seen in Figure 3. Note that the ALMA–SMA correlation is calculated only in the short overlapping time of 2–3 hr, when Sgr A* is seen at low elevation by both ALMA (where it is setting) and the SMA (where it is rising), contributing additional difficulty to constraining systematic errors.

Apart from the correlation, which informs us about the consistency of the variable component, we are also interested in the consistency of the absolute flux density scale. We characterize it by comparing the median flux density in the overlapping observing periods. These results are summarized in Table 4. The systematic uncertainties of the absolute flux density scaling can be as large as 10% and vary between the days, although the ratios are quite consistent between the bands. These uncertainties do not affect relative variability metrics such as the light-curve modulation index, σ/μ, defined as the standard deviation divided by the mean, given in Table 1 (see also Section 4.2). Yet another way to quantify the differences between the data pipelines is through a mean flux density absolute difference between A2 and A1. In terms of this metric, the mean A1–A2 light-curve consistency is 3.7% on 2017 April 6, 2.7% on 2017 April 7, and 16.0% on 2017 April

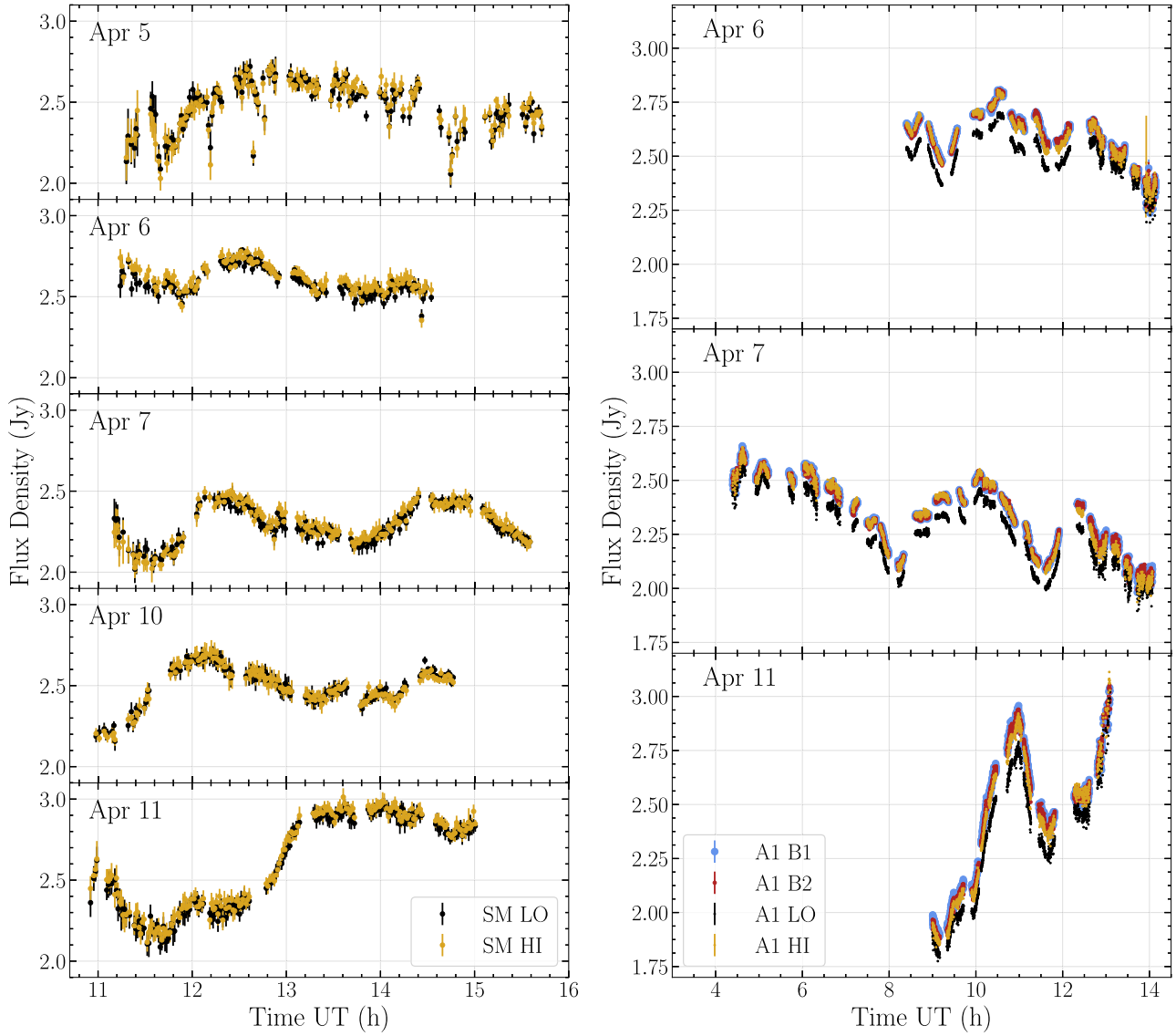

Figure 4. Sgr A* light curves discussed in the body of this paper. Left column: Sgr A* light curves obtained with SMA in the LO and HI bands, for all 5 days of the EHT observations. Right column: Sgr A* light curves obtained with ALMA in the B1, B2, LO, and HI bands, for all 3 days of the EHT observations with ALMA. Only the A1 pipeline results are shown.

11, the latter being strongly dominated by the constant offset in the flux density measurements.

We see that the overall discrepancy between light curves produced by different pipelines can be substantial. In particular, it can be significantly larger than the formal level of the thermal error in the data. Hence, we conclude that the errors are strongly dominated by the calibration systematics, which we attribute predominantly to the imperfections in the gain calibration of the individual telescopes participating in the connected-element arrays, manifesting themselves as slowly varying differences between the pipelines. If the pipelines were considered fundamentally equal, the consistency metrics provided in this section could serve as a proxy for quantifying systematic errors. However, since the A1 pipeline relies less heavily on a priori sensitivity estimates than the other ones, it is expected to be more robust against the relevant sources of corruption. In Figure 3, we observe the decorrelation between A1 and A2 to increase toward the end of the observing tracks, which suggests that these inconsistencies are related to the low source elevation, which is exactly when more severe gain-related corruptions are to be expected. In the subsequent analysis, we stress the A1 pipeline results in particular, supplementing them with the A2 and SM results, allowing us to assess our confidence in the obtained result.

3.2. Consistency within Pipelines

The LNDCF_0 coefficient computed between the different frequency bands within the same pipeline is remarkably high in all cases, above 0.99. This consistency across the frequency bands can be seen in Figure 4. We also verify the ratio of medians in the overlapping observing periods, using the HI band as a reference; see Table 5. We notice that the ratio is very close to unity, which is consistent with the flat mm spectrum of Sgr A* (Marrone et al. 2006; Bower et al. 2015) and expected given the narrow fractional band, $\Delta\nu/\nu \lesssim 0.1$. There is a persistent systematic effect of 4% missing flux density in the LO frequency band (227.1 GHz), seen in both of the ALMA pipelines; see Table 5 and the right panel of Figure 4. This could be a systematic processing/scaling error shared by both of the ALMA reduction pipelines, or an effect of

Table 5
Ratio of the Band Median Flux Density with Respect to the HI Band Median Flux Density

Band	Apr 6	Apr 7	Apr 11	Joined
		A1		
B1	1.00	1.00	1.02	1.00
B2	1.00	1.00	1.01	1.00
LO	0.96	0.96	0.96	0.96
		A2		
B1	0.99	1.00	0.97	0.99
B2	0.99	1.00	0.97	0.99
LO	0.96	0.96	0.96	0.96
		SM		
LO	0.99	0.99	0.99	0.99

absorption in the LO band. A similar effect is not seen in the SMA data, for which spectral channels possibly affected by CN absorption were flagged within the LO band (Section 2.3). However, the absorption alone was estimated to be too small to be responsible for a 4% effect (Appendix H.1. of Goddi et al. 2021). As a result of this discrepancy, we refrain from using the ALMA LO band for applications such as the spectral index estimation.

3.3. Spectral Index

We model the frequency dependence of the flux density with a power law, $F_\nu \propto \nu^\alpha$, thus defining the spectral index as α. Subsequently, we compute α for each pair of simultaneous flux density measurements in the bands (B1, H I) and (B2, H I). We show the results with sample standard deviation error bars in Figure 5. We conclude that the spectral index measured between 213.1 and 229.1 GHz is consistent with zero, $\alpha_{220} = 0.0 \pm 0.1$. Figure 5 implies that the calibration-related systematic uncertainties and short-timescale fluctuations of the spectral index dominate the associated error budget. In Appendix B, we confirm these findings with the full-bandwidth SMA data analysis.

Combining our flux density measurements at 220 GHz of 2.4 ± 0.2 Jy with the compact flux of 2.0 ± 0.2 Jy at 86 GHz reported by Issaoun et al. (2019) based on semi-simultaneous observations on 2017 April 3, we find a spectral index of $\alpha_{150} = 0.19 \pm 0.13$ at $\nu_0 = 0.5 \times (86 + 220) \approx 150$ GHz. Hence, we find a small positive spectral index at about 150 GHz that becomes consistent with zero at about 220 GHz. These findings are generally consistent with a flat spectral index at mm wavelengths reported by Bower et al. (2015) and Iwata et al. (2020), as well as with our broad understanding of the Sgr A* spectral energy distribution, with a flattening spectrum in the mm approaching a peak in the submm ("submm bump"; Zylka et al. 1995; Melia & Falcke 2001). The mean light-curve spectral index may be an important discriminant of the theoretical models of Sgr A* (Ricarte et al. 2022), as this quantity is sensitive to physical properties such as temperature, magnetic field strength, optical depth, and the electron distribution function.

One can also resolve the measured spectral index as a function of time, obtaining the results presented in Figure 6. These measurements show large fluctuations of the spectral index and swings in a range between −0.2 and 0.1 on a timescale of ∼1 hr. This can be interpreted as rapid fluctuations of the effective optical

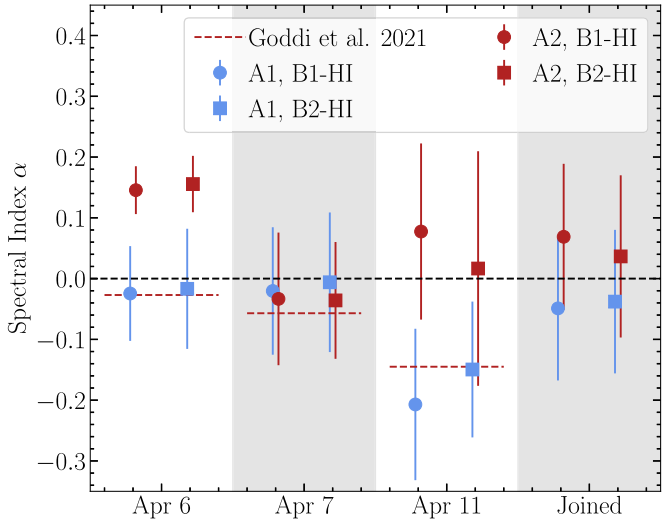

Figure 5. The spectral index at 220 GHz estimated from the presented light curves. We consider ratios between the B1 and HI bands (circles) and the B2 and HI bands (squares). Blue markers correspond to the A1 pipeline and red markers to the A2 pipeline. The red dashed line indicates the values reported by Goddi et al. (2021), based on the raw QA2 ALMA data (see Section 2), consistent with the A1 pipeline measurements.

depth of the compact system, possibly related to the turbulent character of the accretion flow. Interestingly, both pipelines indicate that α was more negative immediately after the 2017 April 11 X-ray flare (ALMA observations begin at 9.0 UT, about 10–15 minutes after the peak of the X-ray flare reported by Chandra in Paper II; see also Figure 3), reaching -0.23 ± 0.05 and subsequently recovering to values consistent with zero on a timescale of 1–2 hr. This suggests an increased contribution of the optically thin component to the total intensity immediately after the X-ray flare. Indeed, since the synchrotron self-absorption decreases with decreasing magnetic field, B, and increasing plasma temperature, T_e (Rybicki & Lightman 1979), a flaring event injecting energy of the magnetic field into electrons through magnetic reconnection (Yuan et al. 2003) is expected to reduce the effective optical depth of the system. Additionally, we note that the first scan by ALMA, which marginally overlaps with the X-ray flare, indicates a decrease in the 1.3 mm emission, while all subsequent scans for the next 2 hr show a growing flux density, in total by about 60%. Such an evolution of the flux density and spectral index suggests a particle acceleration event where magnetic reconnection heats up electrons to a power-law distribution (Guo et al. 2014; Sironi & Spitkovsky 2014; Werner et al. 2015), thus shifting the emission to near-IR and X-ray wavelengths and causing an inverted spectrum (i.e., $\alpha < 0$). As the electrons cool down radiatively, and subsequently the reconnection layer powering the flare depletes (Ripperda et al. 2021), the optically thin emission shifts back to mm and radio wavelengths (e.g., Brinkerink et al. 2015), and the source eventually settles back to the state before the flare.

An elevated X-ray activity was also reported in Chandra observations on 2017 April 7 at 11–13 UT (Paper II). Here we see that this X-ray event was accompanied by a decreased spectral index period in our A1 pipeline data (as seen in Figure 6) and a total flux density decrease at 11–13 UT in the A1 pipeline and the SMA observations. This was then followed up by a flux density recovery seen in the SMA data around 14 UT (as seen in Figure 3). All of these observations further strengthen the presented interpretation.

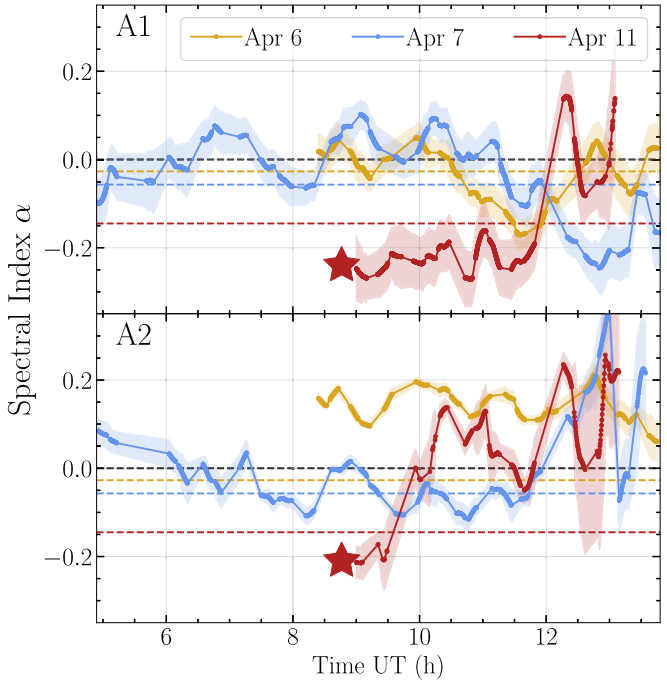

Figure 6. The time dependence of the Sgr A* spectral index between the HI and B1 bands for the two pipelines, A1 (top) and A2 (bottom). The lines and color bands for each day represent a mean and standard deviation calculated in a running window with a width of 10 minutes. Dashed lines indicate values reported by Goddi et al. (2021) for each corresponding day. The red star marks the peak of the X-ray flare on 2017 April 11. While there are overall significant discrepancies between the pipelines, they both indicate a negative spectral index of Sgr A* immediately after the X-ray flare.

4. Variability Characterization

The compact radio source Sgr A* is associated with a supermassive black hole of mass $\sim 4 \times 10^6\, M_\odot$ (Do et al. 2019a; Gravity Collaboration et al. 2019). The mm synchrotron emission unresolved by the ALMA and SMA arrays originates predominantly in the hot innermost part of the accretion flow, on a scale of a few Schwarzschild radii (Doeleman et al. 2008; Fish et al. 2011; Paper I).[153] Given that the light-crossing timescale, $t_M = GM/c^3$, is only about 20 s for Sgr A*, brightness variability on timescales as short as $\sim$1 minute can be expected. A characterization of the variability can be achieved through the estimation of the associated magnitudes and timescales. By comparing the variability analysis results for different days, we aim to establish whether the estimated variability properties persist over the whole period covered by the observations or whether they change with time. Such changes, if detected, could indicate a variation in the state of the source and be compared with other observables, such as the simultaneous VLBI observations (Paper I), for a deeper understanding of the emission process.

[153] It is prudent to notice that in our observations the longest projected ALMA baselines reach about 0.2 Gλ ($\sim$1″), ALMA-APEX 2 Gλ ($\sim$100 mas), while the shortest EHT non-intrasite VLBI baselines reach 500 Gλ ($\sim$400 μas). Thus, there is a range of mas angular scales to which we are blind, and additional extended source structure could be hidden. However, there is no evidence for a significant missing flux, either in the EHT data or in the lower-frequency VLBI observations. This is discussed more extensively in Papers II and V.

4.1. Comparison to Historic Data

In Table 6, we present the previously published Sgr A* light-curve data sets at frequencies close to 230 GHz (that is, closest in frequency to our H I band). We only consider observations with radiointerferometric arrays, where reliable extraction of the compact source light-curve component is feasible. Compared to data sets published in this paper, summarized in Table 1, the archival data sets typically have lower cadence and a far lower number of collected data points. Thus, more reliable studies of the source variability, particularly on short timescales, are enabled by our new data sets.

All data sets given in Tables 1 and 6, spanning a total period of about 14 yr, can be divided into 18 observing epochs no longer than 16 days, where the EHT observations constitute a single epoch of 2017 April 5–11. Normalized histograms of the 230 GHz flux density observed in these epochs are shown in the top left panel of Figure 7. The flux density remains remarkably consistent across all these epochs, with all measurements in agreement with 4.0 Jy within about 50%.

We also show a (differently normalized) generalized λ distribution (GλD; Freimer et al. 1988) fit to all of the 2005–2019 data sets, computed using the `gldex` package (Su 2007). It approximates the full distribution of the Sgr A* flux density at 230 GHz across all of the observing epochs. The GλD fit corresponds to flux density values within $3.24^{+0.68}_{-0.60}$ Jy at 68% confidence, indicating a weak positive tail driven primarily by the record high flux densities observed by Fazio et al. (2018). All measurements given in Tables 1 and 6 are also shown in the bottom panel of Figure 7 as a function of the observing date.

These ranges are also consistent with Sgr A* monitoring with ALMA and SMA in 2013 June–2014 November presented in Bower et al. (2015).[154] The relative calmness of Sgr A* is in strong contrast to the X-ray and IR behavior, where flux densities may vary by orders of magnitude during the flaring events (Porquet et al. 2003; Do et al. 2019b). We notice that the 2017 April epoch is characterized by the lowest mean flux density among all 2005–2019 observations. Within several hours of a single observing epoch, the mm flux density of Sgr A* may fluctuate by $\sim$1 Jy.

4.2. Modulation Index

We quantify the variability with the modulation index, σ/μ, corresponding to the ratio between the signal standard deviation, σ, and its mean value, μ. It is related to the rms–flux relation, abundantly used in IR and X-ray studies of variability. We notice, however, that unlike in the IR (e.g., Gravity Collaboration et al. 2020), we did not find strong indications of a linear rms–flux relation in the mm light curves. For a red-noise stochastic process, which we expect to describe the variability of Sgr A* mm light curves well (Dexter et al. 2014), most variability manifests on the longest timescales. Hence, the modulation index, σ_T/μ_T, calculated from a chunk of data of a finite duration T, is biased with respect to the asymptotic modulation index, σ_∞/μ_∞. On the other hand, for a particular light-curve realization, the influence of sparse or nonuniform sampling on σ/μ is small. We verified the robustness of the σ/μ estimation against the measurement

[154] The data set of Bower et al. (2015) consists of at most a single measurement per day and is not reported in Table 6. ALMA detections reported by Bower et al. (2015) are shown in the bottom panel of Figure 7.

Table 6
Archival Sgr A* Light Curves at Frequency ∼230 GHz from the Literature

Reference	Array	Date	Duration (hr)	Samples	Flux Density (Jy)	σ/μ	max–min (Jy)
Marrone (2006)	SMA	2005 Jun 4	3.3	15	3.99 ± 0.44	0.109	1.31
		2005 Jun 9	5.9	32	3.41 ± 0.24	0.071	1.01
		2005 Jun 16	6.5	45	3.85 ± 0.34	0.087	1.07
		2005 Jul 20	5.3	32	3.78 ± 0.27	0.070	0.86
		2005 Jul 22	5.4	33	3.36 ± 0.24	0.071	0.87
		2005 Jul 30	6.8	33	4.12 ± 0.42	0.103	1.95
Marrone et al. (2008)	SMA	2006 Jul 17	6.3	45	3.04 ± 0.25	0.081	0.97
Yusef-Zadeh et al. (2009)	SMA	2007 Apr 1	6.3	13	3.35 ± 0.25	0.074	0.73
		2007 Apr 3	5.3	35	3.32 ± 0.35	0.104	1.14
		2007 Apr 4	6.4	41	2.82 ± 0.11	0.038	0.45
		2007 Apr 5	6.5	32	2.84 ± 0.28	0.097	0.91
Dexter et al. (2014)	CARMA[a]	2009 Apr 5	3.9	46	3.23 ± 0.26	0.081	0.98
		2009 Apr 6	3.8	42	3.33 ± 0.29	0.088	1.13
		2011 Mar 29	4.2	36	3.03 ± 0.57	0.187	2.14
		2011 Mar 31	3.2	25	2.89 ± 0.29	0.102	0.84
		2011 Apr 1	4.2	32	2.99 ± 0.17	0.059	0.73
		2011 Apr 4	3.7	39	3.49 ± 0.37	0.107	1.72
		2012 May 4	4.6	50	3.58 ± 0.27	0.077	1.24
		2012 May 10	4.3	48	3.89 ± 0.38	0.097	1.71
	SMA	2012 May 16	7.6	82	4.13 ± 0.28	0.067	1.35
		2012 May 17	7.5	76	3.94 ± 0.31	0.078	2.02
		2012 May 18	7.0	60	3.91 ± 0.43	0.110	2.23
		2012 May 19	6.7	68	4.21 ± 0.20	0.047	0.98
		2012 Jul 20	3.8	25	2.50 ± 0.20	0.081	0.69
		2012 Jul 21	2.3	24	4.13 ± 0.12	0.030	0.51
		2012 Jul 22	4.0	32	3.29 ± 0.17	0.052	0.73
		2012 Jul 23	2.5	22	2.90 ± 0.34	0.117	0.99
Fazio et al. (2018)	SMA	2015 May 14	5.7	439	5.25 ± 0.36	0.069	1.56
Bower et al. (2018)	ALMA	2016 Mar 3	3.0	40	3.92 ± 0.16	0.040	0.72
		2016 May 3	3.0	45	3.21 ± 0.17	0.054	0.62
		2016 Aug 13	6.4	26	2.66 ± 0.28	0.103	0.82
Witzel et al. (2021)	ALMA	2016 Jul 12	4.7	78	4.00 ± 0.09	0.023	0.34
		2016 Jul 18	6.5	88	3.20 ± 0.34	0.106	1.13
	SMA	2016 Jul 13	6.5	798	3.71 ± 0.22	0.059	0.82
		2017 Jul 15	7.7	1671	2.75 ± 0.27	0.098	1.45
		2017 Jul 25	6.0	1280	2.37 ± 0.15	0.064	0.91
Iwata et al. (2020)	ALMA	2017 Oct 5	1.2	44	2.85 ± 0.07	0.023	0.21
		2017 Oct 7	1.2	45	3.20 ± 0.08	0.025	0.23
		2017 Oct 8	1.2	44	3.11 ± 0.08	0.027	0.30
		2017 Oct 10	1.2	45	3.27 ± 0.05	0.017	0.18
		2017 Oct 11a	1.2	45	3.25 ± 0.06	0.020	0.23
		2017 Oct 11b	1.2	44	2.96 ± 0.05	0.016	0.16
		2017 Oct 14	1.2	44	3.00 ± 0.03	0.009	0.11
		2017 Oct 17	1.2	45	2.63 ± 0.12	0.047	0.36
		2017 Oct 18	1.2	44	2.08 ± 0.08	0.040	0.23
		2017 Oct 19	1.2	45	3.04 ± 0.05	0.018	0.18
Murchikova & Witzel (2021)	ALMA	2019 Jun 12	1.2	1252	4.62 ± 0.06	0.013	0.27
		2019 Jun 13	1.2	1286	3.14 ± 0.05	0.015	0.22
		2019 Jun 14	1.2	1267	3.33 ± 0.13	0.039	0.49
		2019 Jun 20	1.2	1305	3.59 ± 0.07	0.021	0.25
		2019 Jun 21	4.6	3913	3.85 ± 0.19	0.050	0.68

Note.
[a] Combined Array for Research in Millimeter-wave Astronomy, Cedar Flat, California, USA.

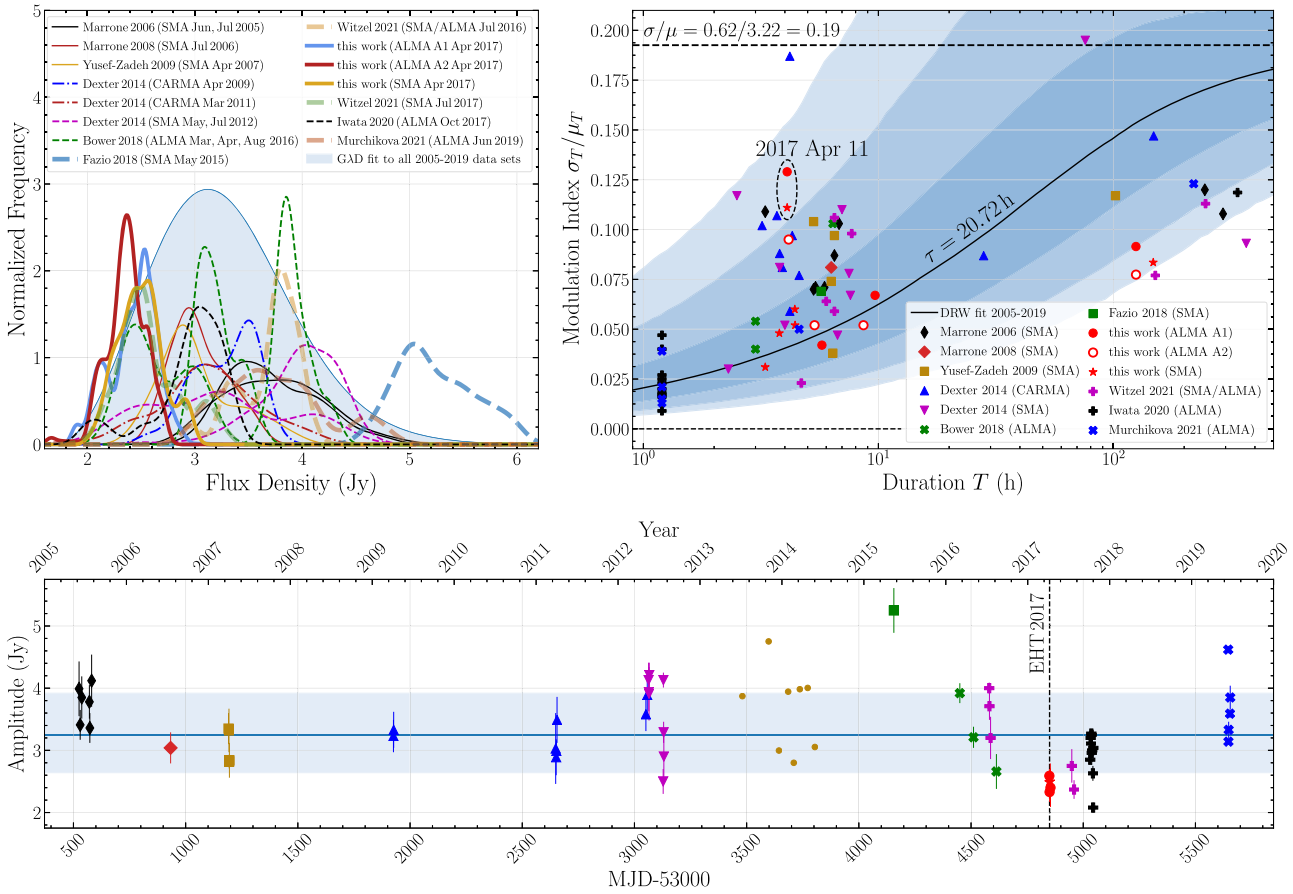

Figure 7. Top left: distributions of the published flux density measurements of Sgr A* at 230 GHz. Each distribution represents an epoch no longer than 16 days. Across all of the epochs, the flux density remained roughly within the 4 ± 2 Jy range. Top right: modulation index, σ_T/μ_T, measured in different observations as a function of the observation duration, T. The black median line and the 1σ, 2σ, and 3σ uncertainty bands, calculated with a Monte Carlo scheme, correspond to expectations from a damped random walk model fitted to the combined 2005–2019 data set (with the timescale $\tau = 20.72$ hr, and with the asymptotic modulation index of $\sigma/\mu = 0.19$ indicated with a dashed line; see also Section 5). Bottom: all data sets presented in Tables 1 and 6 with mean values and standard deviations indicated. The markers follow the convention of the top right panel. Additional points between 2013 and 2015 correspond to ALMA measurements reported in Bower et al. (2015). The horizontal line and blue bands correspond to the median value and 68% confidence interval of a GλD fit to combined 2005–2019 data sets.

noise and irregular sampling by comparing our findings with the results of the intrinsic modulation index algorithm of Richards et al. (2011), finding an excellent agreement. The influence of the light-curve duration T can be seen in the top right panel of Figure 7, where light curves of longer duration generally exhibit a larger modulation index. The figure presents all of the observations listed in Tables 1 and 6. For data sets spanning several days, we also show the modulation index calculated for the entire campaign, corresponding to the histograms in the top left panel of Figure 7. The variability measurements are compared with the expectations from a GP model (damped random walk; black line indicating the expected values, with 1σ, 2σ, and 3σ error ranges plotted as blue bands) best-fitting the full combined 2005–2019 data set; see Section 5 for details and discussion.

The 230 GHz light curves collected in 2005–2019, in particular the high-quality EHT light curves from 2017 April, indicate rather low modulation index, σ/μ, typically below 0.10. Hence, we conclude that on 2017 April 6 and 7 the source displayed an amount of variability consistent with historical measurements. On 2006 July 17 (Marrone et al. 2008), 2015 May 14 (Fazio et al. 2018), and 2017 April 11 (this work and Paper II) increased variability metrics can be connected to flares detected in the X-ray; however, the variability enhancement is particularly clear only in the case of the 2017 April 11 observations. We expect that modulation index values above ~0.15 seen in the top right panel of Figure 7 may possibly be outliers suffering from calibration errors—it is generally far easier to increase the apparent variability with the calibration errors than to reduce it (e.g., erroneous amplitude gains, coherence losses, pointing issues).

The modulation index measured in general relativistic magnetohydrodynamic (GRMHD) simulations was found to be generally larger than what the observations indicate (Chatterjee et al. 2021; Paper V). For comparisons between observations and simulations, a $T = 3$ hr $\approx 540\,GM/c^3$ window for computing the modulation index was used in Paper V. This duration is justified by the synthetic observations decorrelation argument—separate 3 hr segments are expected to behave like statistically independent draws from the modulation index statistic. In Table 7, we give nonoverlapping values of $(\sigma/\mu)_{3\,\mathrm{hr}}$ from all days and sites/pipelines (three nonoverlapping samples for ALMA 2017 April 7, a single 3 hr modulation index measurement for all of the other light curves). The measurements presented in Table 7 show a factor of 2 enhancement of the 3 hr modulation index on the X-ray flare day of 2017 April 11. On the remaining days, the modulation index varies between 0.024 and 0.051, while the damped random walk model fitted to all of the 2005–2019 data sets

Table 7
Independent Measurements of $(\sigma/\mu)_{3\,\mathrm{hr}}$

ALMA A1					
Band	Apr 6	Apr 7			Apr 11
B1	0.026	0.026, 0.048, 0.044			0.098
B2	0.025	0.025, 0.050, 0.044			0.099
LO	0.028	0.030, 0.051, 0.040			0.097
HI	0.029	0.024, 0.051, 0.044			0.099
ALMA A2					
Band	Apr 6	Apr 7			Apr 11
B1	0.043	0.035, 0.044			0.097
B2	0.044	0.035, 0.046			0.098
LO	0.044	0.038, 0.048			0.084
HI	0.045	0.039, 0.050			0.079
SMA					
Band	Apr 5	Apr 6	Apr 7	Apr 10	Apr 11
LO	0.049	0.030	0.042	0.039	0.117
HI	0.049	0.029	0.040	0.040	0.115

predicts $(\sigma/\mu)_{3\,\mathrm{hr}} = 0.03^{+0.02}_{-0.01}$, as shown in the top right panel of Figure 7.

4.3. Structure Function Analysis

To investigate the possible existence of characteristic variability timescales in the Sgr A* light curves, a second-order SF analysis (Simonetti et al. 1985) has been applied to the data. The SF of a time series $\{x_i\} = x_1, x_2,...,x_n$, observed at times $\{t_i\} = t_1, t_2,...,t_n$, at time lag Δt, is defined as

$$\mathrm{SF}(\Delta t) = \frac{1}{M_{\Delta t}} \sum_{i,j} (x_i - x_j)^2, \tag{5}$$

where the sum is extended to all $M_{\Delta t}$ pairs (t_i, t_j) for which $\Delta t - \Delta t_0/2 < (t_i - t_j) < \Delta t + \Delta t_0/2$, and Δt_0 is the shortest time lag for which the SF is calculated. The SF informs us about the signal variance across a range of timescales. A noise contribution has been neglected in Equation (5), given the very high reported data S/N. For this analysis, we use the data cadence reported in Table 1 as Δt_0. Assuming that the observed variability can be described as a sum of the random error (measurement/calibration error) and the true signal, possibly resulting from a complex superposition of processes with different spectral properties and characteristic timescales, the SF is expected to show the following:

1. A flat slope at the shortest timescales, when the random error amplitude dominates over the source signal.
2. A steepening increase on a range of timescales for which the random error amplitude is nonnegligible compared to the signal.
3. A steep increase with a constant slope, on timescales for which the contribution of the random error to the flux density measurements is negligible compared to the variations induced by the source. If the signal can be modeled in the spectral domain as a power law with the PSD exponent (α_{PSD}) steeper than ≈ -1.5 but not steeper than -3 (Emmanoulopoulos et al. 2010), the SF slope (α_{SF}) should have a value of $\alpha_{\mathrm{SF}} \approx -(1 + \alpha_{\mathrm{PSD}})$.
4. A change of slope at the characteristic timescale of the source signal, which corresponds to $0.5/f_b$, where f_b is the frequency at which the power-law PSD shows a break. In case the signal is a superposition of multiple components, each characterized by its own timescale and power-law slope, these should be reflected as slope changes in the SF.
5. A plateau at a time lag corresponding to the maximum characteristic timescale of the source.
6. A flat slope at larger timescales, where the SF should oscillate around a value of twice the sum of the variances of the signal and the measurement/calibration noise.

An SF analysis is prone to identifying spurious characteristic timescales resulting from random fluctuations in a finite realization of a red-noise process, possibly interacting with the sampling window function. To determine whether a detected characteristic timescale is real, it is necessary to sample at least several cycles of the variability (that is, to observe for a duration of at least several times longer than the timescale in question). The significance of timescales larger than 0.2 times the total duration of the observations is low; it slowly increases as this ratio becomes smaller. At the shorter timescales, the SF results reflect quite accurately the properties of the signal realized in the light curves. The SF slope can therefore be a faithful estimator for the PSD slope (α_{PSD}).

4.3.1. Estimating Intrinsic Noise

As a first step of the SF analysis, we isolated the random noise component by applying a denoising algorithm, which works as a low-pass filter with a cutoff timescale of $0.01\,\mathrm{hr} < 2GM/c^3$. To verify the correct separation between the source signal and the random noise contribution to the variability, we applied the SF to both the denoised signal and the noise component. In the first case, we checked that the slope at the shortest timescales follows the same trend as at the intermediate ones, where the random noise is negligible. For the noise component, we verified that the SF slope is approximately zero, in agreement with properties of white noise. The noise component becomes subdominant for timescales longer than $\sim$1 minute; see Figure 8. As a by-product of this step, we obtain a realistic estimate of the flux density uncertainties. These uncertainties turn out to be generally larger than the statistical errors reported in the data sets, with values on the order of $\sim$0.5% of the measured flux densities, or about 0.01 Jy. A cross-correlation of the ALMA noise component extracted from the two independent calibration procedures shows that for all epochs and frequencies there is no correlation between them. This result allows us to conclude that the random noise is mainly due to the calibration-specific uncertainties.

4.3.2. SF Analysis Results

The results of the SF analysis applied to the denoised light curves and cross-checked on the original ones are reported in Tables 8–9. The variability characteristics inferred through the SF appear to be nearly identical across all of the frequency bands, while they show a noticeable variation with both the observing day and the instrument/calibration pipeline (e.g., the SFs of the ALMA B1 band A1 and A2 pipeline light curves,

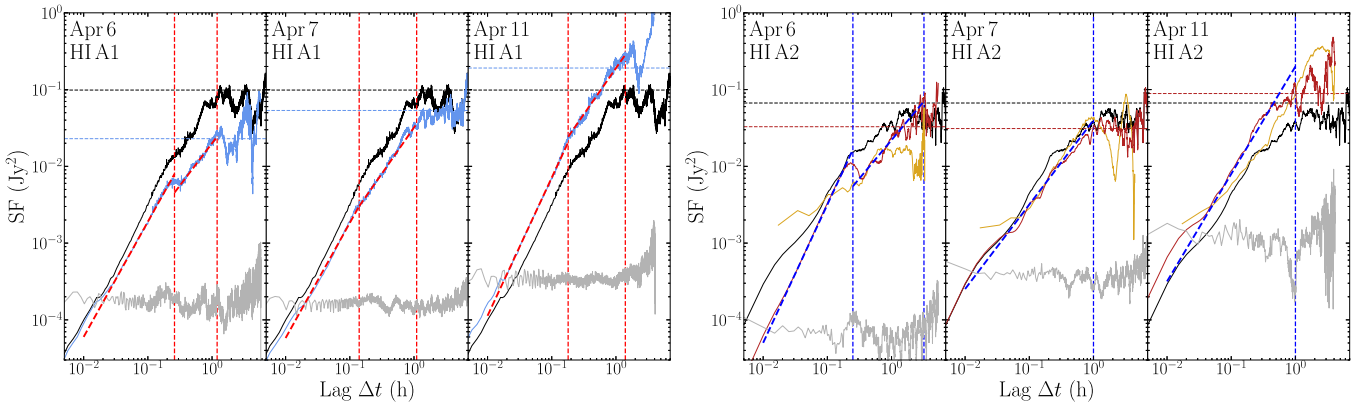

Figure 8. Left: SF plots for the ALMA A1 pipeline HI band data. Results are shown for 2017 April 6, 7, and 11 (from left to right). Results from the joined data sets are shown in black. The dashed lines indicate the estimated timescales and slopes reported in Table 8, and the value of twice the variance, where the SF is expected to asymptote for long lags in the case of stationary signals. The gray lines represent the SF calculated for the extracted noise component; its flat slope confirms the white-noise characteristic of this component. Right: same as the left panel, but for the ALMA A2 pipeline HI band data (red lines). Additionally, the SMA HI band SFs are shown (orange curves). An excess variance on 2017 April 11 can be seen across all pipelines, particularly at the longer timescales.

plotted in Figure 8). Despite these differences, the SF results seem to converge toward a description of the variability as a superposition of two power-law components. The faster component corresponds to a timescale, t_1, between 0.14 and 0.30 hr and is characterized by a steeper slope for delays $\Delta t < t_1$ ($\alpha_{\rm SF} \sim 1.6$). The slower component is characterized by a milder slope ($\alpha_{\rm SF} \sim 1.1$) for lags between t_1 and timescale $t_2 \approx 1.0$–1.5 hr. In most of the epochs, it is possible to observe a long-term trend that exceeds the duration of the observations; this explains the episodic detection of a further SF timescale for which we can only derive a lower limit between 3 and 6 hr.

Both timescales above should be taken with some caution. The 0.14–0.30 hr timescale is highly significant given the number of variability cycles available across the entire period of the observation. However, the fact that this timescale is similar to the scan segmentation timescale raises the suspicion of a sampling effect. This suspicion is corroborated by some discrepancies in the SF shape at short timescales for the A1 and A2 pipeline data, although the combined A2 light curves do indicate a similar break; see Figure 8. The fact that the SMA data never show evidence of such a fast variability component is less significant because of the higher noise and worse sampling of the light curves, which could make its detection very difficult. Additionally, we verified for the synthetic light curves modeled in the GP framework (see Section 5.5) that the sampling of the ALMA observations is sufficient to measure the SF slopes robustly and without any persistent spurious characteristic timescales shorter than ∼1 hr. Finally, indication of the SF slope flattening on a timescale of ∼0.3 hr was also reported by Iwata et al. (2020). We measured the slope in their data set to be $\alpha_{\rm SF} \approx 1.8$. Recently, the analysis of high-cadence ALMA light curves was reported by Murchikova & Witzel (2021), who found $\alpha_{\rm SF} \approx 1.6$ (when adopted to our conventions) for timescales shorter than 0.4 hr. Overall, we see suggestive evidence that the SF slope, $\alpha_{\rm SF}$, is steeper than 1.0 for short-timescale variability, and closer to 1.6. This is inconsistent with the damped random walk model; see more discussion in Section 5.5. Within the power-law PSD model assumption, these findings correspond to a PSD slope of $\alpha_{\rm PSD} \approx -2.6$, flattening to about -2 for variability on timescales longer than 0.15–0.30 hr, comparable to the dynamical timescale of the innermost part of the accretion flow.

The 1.0–1.5 hr characteristic timescale falls into a time range for which the number of measured variability cycles is still not large enough to ensure the significance of the detection. Its identification in the all-epoch light curves corroborates the detection, but the sampling effects are still too important to reach a very confident conclusion.

With the presented SF analysis, we confirm the intrinsic source variability on timescales as short as 1 minute $\approx 3\,GM/c^3$, which is generally less than the expected emission region diameter (Paper V). This implies that at least the variability on shortest timescales must have a structural characteristic in the compact source resolved by the EHT, and it hence requires mitigation in the analysis of the VLBI data beyond the simple light-curve normalization (Paper IV; Broderick et al. 2022; Georgiev et al. 2022).

Another important observation concerns the difference between 2017 April 11 and other observing days. The SF values on 2017 April 6 and 7, as well as the SMA-only values on 2017 April 5 and 10, are reasonably consistent. However, we see that SF values for 2017 April 11 are significantly larger than those found for the other days. This is consistent with Table 1, reporting standard deviations larger by a factor of ∼2–3 on 2017 April 11, compared to those measured on the other days. The SF analysis allows us to see that this effect of enhanced variability is present across all timescales, although it becomes more prominent for the longer ones; for a minute timescale the ratio between the 2017 April 11 SF and the 2017 April 6/7 SF is ∼2, and it becomes ∼10 for timescales longer than 1 hr. We connect this significantly enhanced variability to the flaring event preceding the ALMA observations on 2017 April 11. Interestingly, this enhanced variability effect is seen also in the SMA light curves, despite the fact that the SMA started observing 2 hr after the X-ray flare peak.

4.4. Autocorrelations

In the case of stationary signals, there is a unique relationship between the autocorrelation and the SF (see Section 5). Nevertheless, apart from the uncertainty in the stationarity assumption, studying autocorrelations separately offers a different perspective into the data. We study the signal autocorrelation using the LNDCF method (Lehar et al. 1992), Equation (4). A summary of these results is shown in Figure 9.

Table 8
Structure Function Analysis Results for the ALMA Light Curves

Data Set	Timescales (hr)	Slopes α_{SF} $\alpha_{PSD} \approx -(1+\alpha_{SF})$	Noise (Jy)
	2017 Apr 6		
A1 B1	0.26 ± 0.05, >1.2	1.5, 1.1	0.008
A1 B2	0.26 ± 0.05, >1.2	1.5, 1.1	0.009
A1 LO	0.26 ± 0.05, >1.2	1.4, 1.1	0.010
A1 HI	0.26 ± 0.05, >1.2	1.5, 1.1	0.009
A2 B1	0.25 ± 0.05, >3.2	1.8, 1.0	0.006
A2 B2	0.25 ± 0.05, >3.2	1.8, 1.0	0.006
A2 LO	0.25 ± 0.05, >3.2	1.8, 1.0	0.006
A2 HI	0.25 ± 0.05, >3.2	1.8, 1.0	0.006
	2017 Apr 7		
A1 B1	0.14 ± 0.03, 1.1 ± 0.3, >6	1.5, 1.2,⋯	0.009
A1 B2	0.14 ± 0.03, 1.1 ± 0.3, >6	1.5, 1.2,⋯	0.009
A1 LO	0.14 ± 0.03, 1.1 ± 0.3, >6	1.5, 1.2, ⋯	0.010
A1 HI	0.14 ± 0.03, 1.1 ± 0.3, >6	1.5, 1.2, ⋯	0.010
A2 B1	1.1 ± 0.3, >6	1.1,⋯	0.013
A2 B2	1.1 ± 0.3, >6	1.1, ⋯	0.013
A2 LO	1.1 ± 0.3, >6	1.1, ⋯	0.014
A2 HI	1.1 ± 0.3, >6	1.1, ⋯	0.014
	2017 Apr 11		
A1 B1	0.18 ± 0.03, 1.4 ± 0.4	1.8, 1.2	0.013
A1 B2	0.18 ± 0.03, 1.4 ± 0.4	1.8, 1.2	0.013
A1 LO	0.18 ± 0.03, 1.4 ± 0.4	1.8, 1.2	0.014
A1 HI	0.18 ± 0.03, 1.4 ± 0.4	1.8, 1.2	0.013
A2 B1	1.4 ± 0.4	1.4	0.019
A2 B2	1.4 ± 0.4	1.4	0.019
A2 LO	>1.0	1.4	0.024
A2 HI	>1.0	1.4	0.022
	All Days		
A1 B1	0.23, 1.2 ± 0.4, >6	1.7, 1.2	⋯
A1 B2	0.23, 1.2 ± 0.4, >6	1.7, 1.2	⋯
A1 LO	0.23, 1.2 ± 0.4, >6	1.6, 1.2	⋯
A1 HI	0.23, 1.2 ± 0.4, >6	1.6, 1.2	⋯
A2 B1	0.26, 1.5 ± 0.3	1.3, 1.0	⋯
A2 B2	0.26, 1.5 ± 0.3	1.3, 1.0	⋯
A2 LO	0.3, 1.4 ± 0.4	1.3, 1.1	⋯
A2 HI	0.3, 1.4 ± 0.4	1.3, 1.1	⋯

Note. The first reported slope corresponds to lags shorter than the first reported timescale, and so on.

Table 9
Structure Function Analysis Results for the SMA Light Curves

Data Set	Timescales (hr)	Slopes α_{SF} $\alpha_{PSD} \approx -(1+\alpha_{SF})$	Noise (Jy)
	2017 Apr 5		
SM LO	1.7 ± 0.3	0.7	0.060
SM HI	1.7 ± 0.3	0.7	0.060
	2017 Apr 6		
SM LO	0.9 ± 0.2	1.2	0.030
SM HI	0.8 ± 0.2	1.0	0.030
	2017 Apr 7		
SM LO	1.0 ± 0.1	1.4	0.020
SM HI	1.0 ± 0.1	1.4	0.020
	2017 Apr 10		
SM LO	1.0 ± 0.1	1.5	0.017
SM HI	1.0 ± 0.1	1.5	0.016
	2017 Apr 11		
SM LO	2.3 ± 0.1	1.5	0.020
SM HI	2.3 ± 0.1	1.5	0.030
	All Days		
SM LO	3.3 ± 0.1	1.1	⋯
SM HI	3.3 ± 0.1	1.1	⋯

In this plot, we indicate all of the contributing autocorrelation measurements (circles), with the running mean (colored line) and the running one standard deviation bands. In the first panel of Figure 9, we show the autocorrelation calculated using all of the available observations in each pipeline, in the H I band (the other bands are very consistent). The data indicate autocorrelations decreasing roughly on a timescale of ∼1 hr; the black dashed line corresponds to $\exp(-\Delta t/1\,\mathrm{hr})$. This is significantly less than one would expect based on the results of Dexter et al. (2014). In the subsequent panels of Figure 9, we show autocorrelations for 2017 April 6, 7, and 11. The nonmonotonic structure of the autocorrelation functions is not detected confidently, given the associated uncertainties. The persistence of such features may be established with more observations, e.g., pipeline A1 results show a bump at ∼30 minutes for both 2017 April 7 and 11. This resembles the innermost stable circular orbit period for a Schwarzschild black hole with $4 \times 10^6\ M_\odot$ mass, but there is very little confidence in such an association at this point. Significant biases that may affect the autocorrelation measurement prevent us from drawing strong conclusions based on this analysis; see the discussion in Section 5.5.

Several authors have recently considered signatures of multiple-path propagation of photons traveling through a strongly curved spacetime in a black hole vicinity and reaching the observer with a delay (e.g., Moriyama et al. 2019; Chesler et al. 2021; Hadar et al. 2021; Wong 2021; or Wielgus et al. 2020 for the case of exotic spacetimes of black hole mimickers). While observing a feature related to a photon shell around a black hole is a tantalizing possibility, such an observation does not seem feasible yet, given the model simplifications and the limited duration of the observations. There are no significant signatures of autocorrelations detected at the relevant time lags of $\sim 20GM/c^3 \approx 400$ s in our presented data sets.

4.5. Lags between the Frequency Bands

The presence of time lags between frequency bands in observations of Sgr A* has been theoretically predicted. In the optically thick regime of radio observations at frequencies below 100 GHz, theoretical models attribute those lags to the adiabatic spherical expansion of plasma blobs (van der Laan 1966; Yusef-Zadeh et al. 2008; Eckart et al. 2012), or to a bulk outflow (Falcke et al. 2009). Such lags could be detected across the spectrum, with the higher-frequency signal typically leading the lower frequency signal (Yusef-Zadeh et al. 2009; Brinkerink et al. 2015, 2021). Hints of a similar delay structure have been seen in some numerical GRMHD models of Sgr A* compact emission (Chan et al. 2015). In this

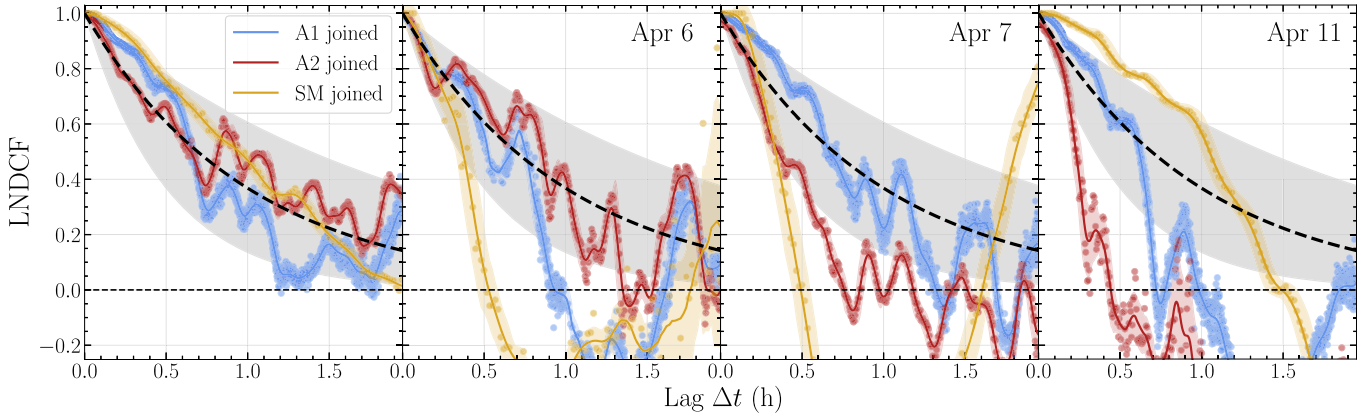

Figure 9. Estimated autocorrelation of the Sgr A* light curves in the HI band. The black dashed line corresponds to an exponential decay with 1 hr timescale, and the shaded region corresponds to autocorrelation timescales between 0.5 and 2 hr. Due to the irregular sampling, we show the actual values of the measured autocorrelation along with the running mean and the running standard deviation uncertainty band for each day.

theoretical framework, we could expect lags of 1–2 minutes between the HI and B1 bands, easily detectable with the cadence of the ALMA data. However, no indication of a correlation lag between the bands in any of our data sets is found, with the uncertainty no larger than 20 s. The cross-correlation function very clearly peaks at zero for all days and for both ALMA reduction pipelines, as shown in Figure 10. We interpret this lack of detectable delays as a signature that the emission region in the 213–229 GHz range is already optically thin all the way to the horizon, possibly with patches of higher optical depth material formed in the turbulent accretion flow, necessary to explain the intermediate spectral index $\alpha \approx 0$ (identified in Section 3.3). This is particularly likely given that in 2017 April Sgr A* was in a rather low mm flux density state (Section 4; Mościbrodzka et al. 2012). Historically, no delays were reported by Iwata et al. (2020) across similar frequency bands; there was also no significant delay between 230 and 345 GHz reported by Marrone et al. (2008), and no delay between 134 and 146 GHz or between 230 and 660 GHz reported by Yusef-Zadeh et al. (2009). Finally, the conclusion of a low optical depth is consistent with the interpretation of the first EHT images of Sgr A*, reported in Paper III, as the observable shadow of a supermassive black hole.

5. Modeling Light-curve Variability

We attempt to represent the variable behavior of the Sgr A* light curves using statistical models within a GP framework (Rasmussen & Williams 2006). The GP assumption is restrictive by itself. To a degree its impact was investigated by Dexter et al. (2014), who compared fits to light curves in linear and in logarithmic space, finding reasonably consistent results. We consider the low relative variability of the 230 GHz light curves (see Section 4), with only weak tails of the flux density distributions, to be a convincing motivation for limiting the modeling efforts to GP. To fit the models and explore the associated posterior probability space, we use the dynamic nested sampling algorithm implemented in `dynesty` (Speagle 2020).

5.1. Damped Random Walk (DRW)

DRW (or the Ornstein–Uhlenbeck process) is a unique Markovian stationary GP (Rasmussen & Williams 2006). Application of the DRW as a mathematical model to describe

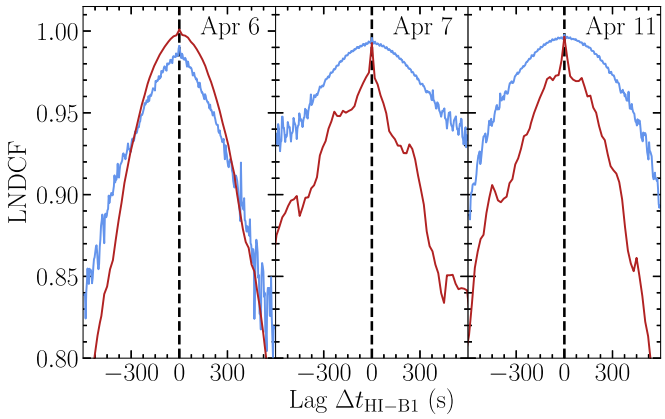

Figure 10. The cross-correlation between the HI and B1 bands for the time lags ±600 s. The results for the A1 (A2) pipeline are shown in blue (red). There is no indication of delays between the frequency bands.

the optical variability of quasars was proposed by Kelly et al. (2009). The DRW with variance σ^2 is characterized by a covariance function,

$$k_{\rm DRW}(\Delta t) = \sigma^2 \exp\left(-\left|\frac{\Delta t}{\tau}\right|\right), \quad (6)$$

where a characteristic timescale, τ, is a model parameter. For stationary processes there is a general relation between the covariance and the SF defined in Equation (5),

$$\mathrm{SF}(\Delta t) = 2\sigma^2 - 2k(\Delta t). \quad (7)$$

The corresponding PSD is related to the covariance function through the Wiener–Khinchin theorem, and in the case of a DRW process it becomes

$$\mathrm{PSD}(f) = \frac{4\sigma^2\tau}{1 + (2\pi f\tau)^2}, \quad (8)$$

which corresponds to a red-noise spectrum with an index of $\alpha_{\rm PSD} = -2$ in a high-frequency limit ($f\tau \gg 1$) and a flat white-noise spectrum at low frequencies ($f\tau \ll 1$). In the context of the Galactic Center, Dexter et al. (2014) modeled the Sgr A* variability at mm wavelengths with the DRW, following the procedure outlined by Kelly et al. (2009). By fitting several

years of Sgr A* observations (Section 4), they identified a poorly constrained DRW timescale of $\tau \sim 8$ hr.

Our model differs from that of Kelly et al. (2009) and Dexter et al. (2014) only by the inclusion of an additional parameter, σ_0, representing the noise floor. Then, the full model consists of four variables,

$$\theta = (\tau, \mu, \sigma, \sigma_0), \tag{9}$$

the correlation timescale τ, the mean value of the process μ, the standard deviation σ, and the noise floor σ_0. The timescale τ is not necessarily related to the timescales estimated in Section 4.3—the SF timescales may be indicative of the presence of multiple stochastic components in the real signal. Because the DRW is a Markovian process, the likelihood function for observations, $\{x_i\} = x_1, x_2,...,x_n$, observed at times $\{t_i\} = t_1, t_2,...,t_n$, can be calculated directly as

$$p(\{x_i\}|\theta) = \prod_{i=1}^{n} \frac{\exp[-0.5(\hat{x}_i - x_i^*)^2/\widetilde{\Omega}_i]}{(2\pi\widetilde{\Omega}_i)^{1/2}}, \tag{10}$$

where

$$\widetilde{\Omega}_i = \Omega_i + \sigma_0^2 + \sigma_i^2, \tag{11}$$

$$x_i^* = x_i - \mu. \tag{12}$$

The indexed σ_i represents measurement uncertainties and is distinct from the estimated process standard deviation σ and the noise floor σ_0. The quantities Ω_i and $\hat{x}_i$ are calculated through an iterative procedure,

$$\hat{x}_i = a_i \hat{x}_{i-1} + \frac{a_i \Omega_{i-1}}{\widetilde{\Omega}_{i-1}}(\hat{x}_{i-1} - x_{i-1}^*), \tag{13}$$

$$\Omega_i = \Omega_1(1 - a_i^2) + a_i^2 \Omega_{i-1}\left(1 - \frac{\Omega_{i-1}}{\widetilde{\Omega}_{i-1}}\right), \tag{14}$$

$$a_i = \exp[-(t_i - t_{i-1})/\tau], \tag{15}$$

with the initial conditions

$$\Omega_1 = \sigma^2; \hat{x}_1 = 0. \tag{16}$$

Note that we use a slightly different parameterization of the DRW model than Kelly et al. (2009), with σ^2 representing the variance of the DRW, related to their parameterization by $\sigma_{\rm Kelly} = \sigma\sqrt{2/\tau}$. Since the procedure outlined above allows us to explicitly compute the best-fitting DRW realization for a given vector of parameters, θ, we can assess the fit quality by computing the reduced-χ^2 statistic for the residuals,

$$\chi_n^2 = \frac{1}{n}\sum_{i=1}^{n} \frac{(x_i^* - \hat{x}_i)^2}{\widetilde{\Omega}_i}. \tag{17}$$

5.2. Matérn Covariance Model

The DRW model fixes the high-frequency limit PSD slope to $\alpha_{\rm PSD} = -2$. This is a rather strong assumption, and there are indications of a steeper PSD slope in both the context of optical variability of quasars (Mushotzky et al. 2011; Zu et al. 2013) and the variability of X-ray binaries (e.g., Tetarenko et al. 2021). The high-frequency PSD slope may be a relevant parameter to extract, less affected by the sampling and observation duration limitations than the timescale τ, and having the potential to constrain theoretical models of Sgr A*. Moreover, observations presented in this paper sample the high-frequency regime, relevant for constraining $\alpha_{\rm PSD}$ uniquely well. Hence, we employ a more general statistical model of a GP with a Matérn covariance function (see, e.g., Rasmussen & Williams 2006),

$$k_{\rm Mat}(\Delta t) = \sigma^2 \frac{2^{1-\nu}}{\Gamma(\nu)}\left(\sqrt{2\nu}\frac{\Delta t}{\tau}\right)^{\nu} K_\nu\left(\sqrt{2\nu}\frac{\Delta t}{\tau}\right), \tag{18}$$

where K_ν is the modified Bessel function of the second kind. The parameter ν defines the order of the Matérn process and subsequently controls the smoothness of the resulting curve. The PSD of the Matérn process is

$$\mathrm{PSD}_{\rm Mat}(f) \propto \left[1 + \frac{(2\pi f\tau)^2}{2\nu}\right]^{-(\nu+1/2)}, \tag{19}$$

so in the high-frequency limit $f\tau \gg 1$ we find the PSD slope of $\alpha_{\rm PSD} = -2\nu - 1$. The DRW is recovered as a special case of the Matérn process with $\nu = 0.5$. As an arbitrary ν, the Matérn covariance represents a non-Markovian process, and the likelihood cannot be evaluated explicitly as in the case of the DRW. Instead, we evaluate it numerically using the `Stheno` library.[155]

5.3. Modeling Setup

Given the low computational cost of the DRW model fitting, we were able to perform a survey of different modeling parameters, such as the type and range of priors, subsets of data to be used, and treatment of the systematic uncertainties and the noise floor. Our general conclusion is that the timescale τ cannot be well constrained and its posterior distributions are dominated by the assumed priors. As an example, Dexter et al. (2014) used log-uniform priors, reducing the distribution tails for large τ. We find that for our data sets τ remains poorly constrained, and with uniform priors very large timescales are permitted. As noted by Kozłowski (2017), the duration of the light curve needs to be significantly longer than the timescale τ to constrain it reliably. The duration and sampling of the 2017 April data may not be sufficient. On the other hand, when fitting data spanning several years (such as in the case of Dexter et al. 2014), one needs to consider whether the underlying process can be assumed to be stationary on such long timescales (e.g., as a consequence of the mass accretion rate modulation).

As a result of the DRW survey, we selected the following set of priors, $\pi(\theta)$:

$$\begin{aligned} \tau\ (\mathrm{hr}) &\sim \mathcal{N}_{\rm T}(0, 8), \\ \mu\ (\mathrm{Jy}) &\sim \mathcal{N}_{\rm T}(2, 1), \\ \sigma\ (\mathrm{Jy}) &\sim \mathcal{N}_{\rm T}(0, 1), \\ \sigma_0\ (\mathrm{Jy}) &\sim \mathcal{U}(0.0, 0.1), \end{aligned} \tag{20}$$

where $\mathcal{N}_{\rm T}(a, b)$ is a normal distribution of mean a and standard deviation b truncated to positive values, and $\mathcal{U}(a, b)$ is a uniform distribution with a range between a and b. For the Matérn model fitting, we adopt identical priors as given by

[155] https://github.com/JuliaGaussianProcesses/Stheno.jl

Table 10
Gaussian Process Modeling Results (ML Estimators with 68% Confidence Intervals)

Data Set	DRW						Matérn					
	μ (Jy)	σ (Jy)	τ (hr)	σ_0 (Jy)	χ^2_n	$\log Z_{\rm DRW}$	μ (Jy)	σ (Jy)	τ (hr)	$\alpha_{\rm PSD}$	σ_0 (Jy)	$\log Z_{\rm Mat}$
SM all LO	$2.45^{+0.14}_{-0.13}$	$0.20^{+0.13}_{-0.02}$	$3.57^{+5.63}_{-0.62}$	< 0.005	0.77	1389	$2.47^{0.31}_{-0.42}$	$0.20^{+0.55}_{-0.02}$	$0.87^{+3.60}_{-0.11}$	$-3.25^{+0.61}_{-0.47}$	< 0.005	1412
SM all HI	$2.46^{+0.16}_{-0.13}$	$0.21^{+0.13}_{-0.02}$	$3.86^{+5.62}_{-0.73}$	< 0.005	0.72	1356	$2.48^{+0.31}_{-0.42}$	$0.21^{+0.57}_{-0.02}$	$0.93^{+2.85}_{-0.37}$	$-3.19^{+0.65}_{-0.43}$	< 0.005	1377
A1 all LO	$2.37^{+0.23}_{-0.18}$	$0.32^{+0.11}_{-0.04}$	$10.56^{+6.84}_{-2.66}$	0.010	1.01	5128[a]	$2.39^{+1.12}_{-0.41}$	$0.29^{+0.62}_{-0.06}$	$1.96^{+5.41}_{-0.63}$	$-2.60^{+0.33}_{-0.41}$	0.011	4967
A1 all HI	$2.42^{+0.25}_{-0.22}$	$0.32^{+0.12}_{-0.04}$	$10.36^{+6.27}_{-2.95}$	0.010	1.01	5025[a]	$2.46^{+0.48}_{-0.69}$	$0.31^{+0.63}_{-0.05}$	$1.92^{+5.26}_{-0.61}$	$-2.65^{+0.44}_{-0.33}$	0.010	5054
A2 all LO	$2.20^{+0.23}_{-0.18}$	$0.24^{+0.18}_{-0.02}$	$3.46^{+6.51}_{-0.66}$	0.014	1.09	4085	$2.22^{+0.97}_{-0.31}$	$0.23^{+0.55}_{-0.03}$	$1.56^{+5.67}_{-0.46}$	$-2.31^{+0.34}_{-0.30}$	0.012	4029
A2 all HI	$2.30^{+0.32}_{-0.19}$	$0.25^{+0.18}_{-0.02}$	$3.65^{+6.60}_{-0.71}$	0.014	1.10	3898	$2.31^{+0.36}_{-0.66}$	$0.24^{+0.56}_{-0.03}$	$1.53^{+5.38}_{-0.53}$	$-2.36^{+0.35}_{-0.28}$	0.013	3864
FULL LO	$2.38^{+0.22}_{-0.12}$	$0.27^{+0.10}_{-0.03}$	$7.37^{+5.83}_{-1.50}$	0.010	0.95	5716[a]	$2.39^{+0.36}_{-0.62}$	$0.26^{+0.54}_{-0.04}$	$1.73^{+5.05}_{-0.39}$	$-2.58^{+0.32}_{-0.30}$	0.011	5748
FULL HI[b]	$2.43^{+0.15}_{-0.18}$	$0.29^{+0.10}_{-0.03}$	$8.07^{+5.79}_{-1.70}$	0.010	0.84	5786[a]	$2.44^{+0.86}_{-0.37}$	$0.28^{+0.58}_{-0.03}$	$1.82^{+5.02}_{-0.43}$	$-2.60^{+0.32}_{-0.31}$	0.010	5817
2005–2019	$3.22^{+0.09}_{-0.10}$	$0.62^{+0.04}_{-0.05}$	$20.72^{+3.16}_{-3.53}$	0.009	1.05	31926						

Notes.
[a] In these fits the DRW evidence and Matérn model results correspond to data sets with the A1 data subsampled with a factor of 4 to facilitate the computationally expensive model fitting. A high degree of consistency between the DRW fits for normal and subsampled data sets has been verified.
[b] Selected as a fiducial DRW fit.

Equation (20), with an additional prior on the PSD slope, $\alpha_{\rm PSD}$,

$$\alpha_{\rm PSD} = -2\nu - 1 \sim \mathcal{U}(-9, -1). \quad (21)$$

5.4. Modeling Results

An overview of the fitting results for different data subsets is shown in Table 10, where the maximum likelihood (ML) estimator parameters are given, along with the 68% confidence intervals. These results establish a good consistency between bands, less so between the pipelines. The estimated noise floor, σ_0, is comparable to the noise amplitudes estimated in Section 4.3.

For the fiducial fit, a combined data set was prepared, merging light curves from the A1 and SM pipelines for increased time coverage (FULL data set in Table 10; see also Table 1 and Appendix C for the fits corner plots) for a light curve with a total time span of 148 hr. In the overlapping time periods, we only use the A1 data. Additionally, since we found constant scaling biases between the pipelines, we correct the SM data by applying small constant (per day/band) scaling factors, reported in Table 4, in order to ensure continuity. The DRW and Matérn fits generally yield consistent ML estimators of mean μ, standard deviation σ, and noise floor σ_0. The Matérn fit has a clear preference for a shorter timescale τ. This may possibly be a demonstration of a DRW bias reported by Kozłowski (2016); the DRW may fit data drawn from different processes well (notice good χ^2_n values reported in Table 10), while biasing timescales toward larger values if the true underlying process has a steeper PSD slope. On the other hand, the DRW timescale fitted to the FULL data sets is consistent with the ∼8 hr found by Dexter et al. (2014) (which, however, could be biased just the same if the true underlying process was not a DRW). For comparison, in IR the DRW timescale was found to be ∼3–4 hr (Meyer et al. 2009; Witzel et al. 2018), between the Matérn and DRW values fitted at mm wavelength. We find that estimated timescales, unlike other model parameters, are generally susceptible to details of the priors. We also report a DRW fit to the FULL data sets (Table 1) combined with the 2005–2019 non-EHT data sets given in Table 6. Due to the numerical conditioning issues of the problem, the Matérn fit was not obtained for this data set. For this complete data set, the fit needs to accommodate a larger historical mean flux density of Sgr A* and a wider range of historically measured values; hence, the mean flux and standard deviation are driven up. It is interesting to notice that the estimated parameters of the 2005–2019 DRW fit are reasonably consistent with the properties of the GλD fit shown in the top left panel of Figure 7, the former corresponding to 3.22 ± 0.62 Jy and the latter corresponding to $3.24^{+0.68}_{-0.60}$ Jy. This confirms that the GP models are capable of describing the source dynamics reasonably well.

5.5. Model Selection and the PSD Slope

Since we explore the posterior space with a nested sampling algorithm, we obtain the Bayesian evidence along with the posterior distributions (Speagle 2020), representing the total likelihood of a given model, Θ,

$$Z_\Theta = \int p(\{x_i\}|\theta)\pi(\theta)d\theta. \quad (22)$$

By directly comparing Bayesian evidences obtained for the same data sets with the DRW and Matérn models, we may select a more likely model. In Table 10, we compare the logarithm of Bayesian evidence for the DRW ($\log Z_{\rm DRW}$) and the Matérn ($\log Z_{\rm Mat}$) models. While the comparison results generally vary depending on the data subset used, the fiducial fit shows the advantage of the Matérn over the DRW model.

We further verify this conclusion by considering a consistency test for the best-fitting DRW and Matérn processes. In this test, we generate a collection of synthetic light curves corresponding to random realizations of the models described by the FULL HI fiducial fits reported in Table 10. These synthetic data sets were generated with the exact sampling of the ALMA A1 light curves from 2017 April 7. We then calculate the analytic SFs for both processes (Equation (7)), empirically measured SFs for the synthetic light curves (Equation (5)), analytic autocorrelation functions (Equations (6) and (18)), and autocorrelations measured on the synthetic light curves (Equation (4)). The results are shown in Figure 11. We see that the bias between the analytic results and what we measure, given the limited time coverage, is more significant for autocorrelations

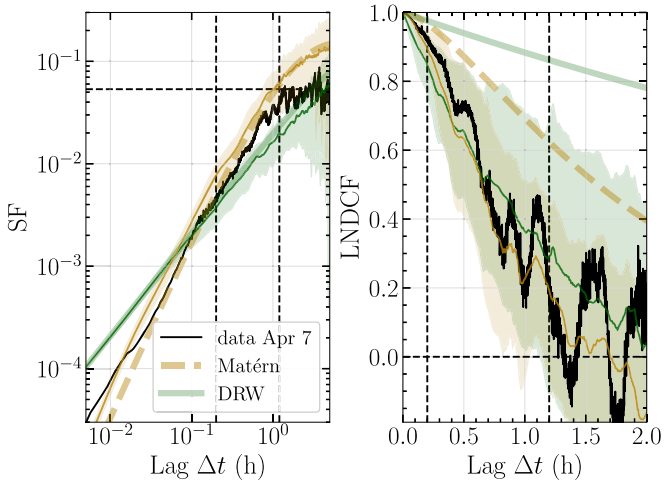

Figure 11. Analytic SF and autocorrelation of the fiducial fits with the DRW and Matérn process compared with the observations (black; A1 pipeline, HI band, 2017 April 7 data). Thin lines and color bands show the median and 1σ ranges for the estimates of the SF and autocorrelation in a random realization of a best-fitting process, given the actual sampling and duration of the ALMA observations.

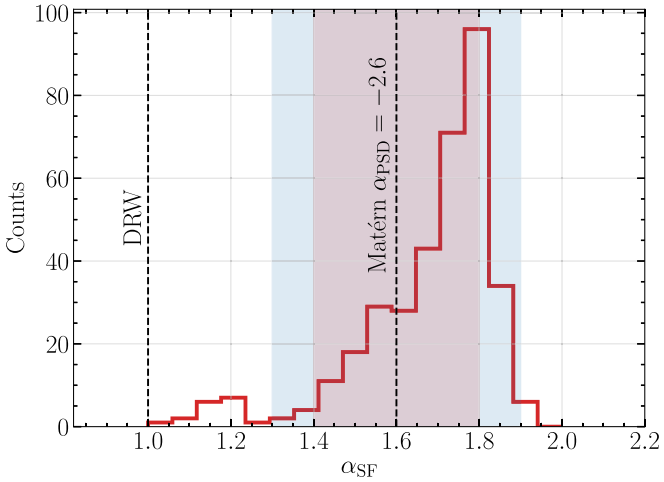

Figure 12. Histogram of the SF slopes ($\alpha_{\rm SF}$) calculated for over 350 GRMHD simulations of Sgr A*. The red shaded region corresponds to the range of slopes measured in the 2017 April observations, and the blue shaded region corresponds to the uncertainty of the slope estimated with the Matérn covariance model. Both the GRMHD simulations and observations disfavor the DRW model and show consistency with the best-fitting Matérn process model.

than for SFs. When these synthetic data tests are compared with the actual SFs and autocorrelations measured from the 2017 April 7 ALMA A1 observations, we see a low constraining power of the autocorrelation measurements. On the other hand, the SFs results show much higher consistency with observations for the Matérn model than for the DRW, as the former reproduces the steep observed SF slope reported in Section 4.3.

We can also make use of the EHT GRMHD library, consisting of over 350 simulations of Sgr A* exploring a variety of black hole spins, observer inclinations, plasma heating parameters, and accretion flow magnetization states (Paper V). In Figure 12, we show a histogram of the high-frequency SF slopes ($\alpha_{\rm SF}$) for the simulation library. The slopes were measured with linear regression on the logarithm of the SF for the timescales shorter than $25\,GM/c^3 \approx 500$ s. The DRW slope is always $\alpha_{\rm SF} = 1$, while for the best-fitting Matérn model with $\alpha_{\rm PSD} = -2.6$ we found the approximated formula given in Section 4.3 to be very consistent with a numerical evaluation, hence $\alpha_{\rm SF} \approx 1.6$. The range of high-frequency slope values measured for ALMA (reported in Table 8) is shaded in red in Figure 12. The uncertainty of the Matérn process slope estimation, as reported in Table 10, is shaded in blue. Remarkably, GRMHD simulations, the SF calculated on observations, and the Matérn fit are reasonably consistent. All GRMHD models indicate $\alpha_{\rm SF} > 1$, steeper than the DRW value.

We also notice that recent results suggest that the mm PSD on shorter timescales may be steeper than $\alpha_{\rm PSD} = -2$ (Iwata et al. 2020; Murchikova & Witzel 2021), and some indications of a steeper 230 GHz slope were also reported by Dexter et al. (2014), who gave a value of $\alpha_{\rm PSD} = -2.3^{+0.6}_{-0.8}$. Along with other hints, all these allow us to conclude that the Matérn covariance model captures the short-timescale variable behavior of Sgr A* light curves better than the DRW model. Note, however, that if the PSD break timescales discussed in Section 4.3 are real, they would not be properly represented within the Matérn covariance model of a single stochastic process with a smooth PSD—the presence of a sharp break in the PSD would indicate superposition of at least two stochastic processes.

6. Periodicity Search and PSD

Identifying a periodic component in radio astronomical data is particularly challenging with the presence of red noise, and given the nonuniform sampling. It is common to misinterpret the uncertainty budget, e.g., by imprinting the white-noise background model in the analysis. Unfortunately, the properly calculated uncertainties related to a particular realization of a stochastic process, along with the nonuniform sampling biases, may prevent one from confidently detecting real periodicity, unless a large number of periods are sampled. In this section, we discuss the PSD estimated from the observational Sgr A* light-curve data with a Lomb–Scargle algorithm (L-S; Scargle 1982). In particular, our aim is to determine whether there are any frequencies excited significantly more than the expectations from the fitted aperiodic GP models, thus indicating a difficulty in interpreting them in the purely stochastic framework discussed in Section 5. Similar investigations in the IR, presented in Do et al. (2009), concluded that the light curves are consistent with a stochastic red-noise process.

If we consider an L-S periodogram of the EHT observations, the red-noise characteristic is apparent; see Figure 13. For ALMA, we can trace the negative slope all the way to a single minute timescale before the observational noise takes over, which was discussed in Section 4.3. The SMA periodograms flatten for timescales shorter than about 3–5 minutes because of the residual noise. For the fiducial fits (FULL HI in Table 10), the transition frequency separating the white- and red-noise parts of the DRW PSD is $f_{\rm DRW} = (2\pi\tau_{\rm DRW})^{-1} = (50\,{\rm hr})^{-1}$, while for the Matérn process fit it is $f_{\rm Mat} = \sqrt{2\nu}(2\pi\tau_{\rm Mat})^{-1} = (9\,{\rm hr})^{-1}$. When the L-S periodogram is compared with the analytic PSDs (Figure 13), neither of the best-fitting models appears to be in good agreement with the data. The reason is the corruption related to the sampling window. To study whether the stochastic model can reproduce the data periodogram, we need to incorporate the real data sampling into the discussion. Hence, we take a Monte Carlo

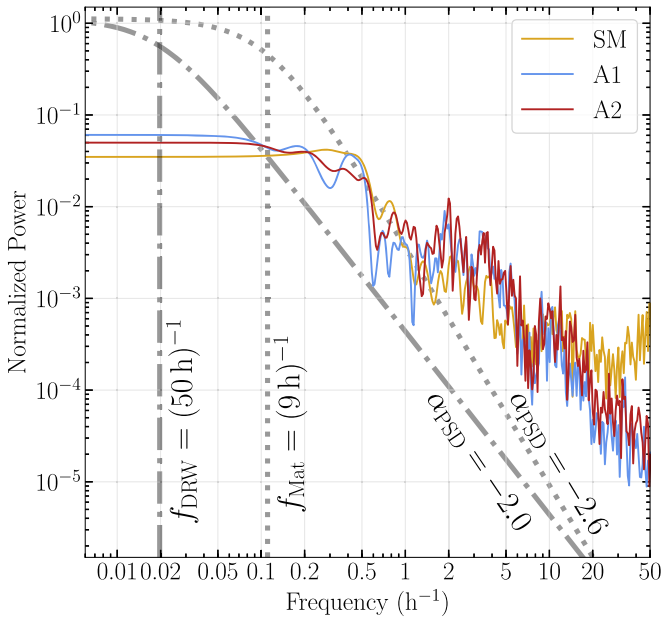

Figure 13. Incoherently averaged, normalized L-S periodograms for all data sets available within each pipeline (averaging all days and bands). The PSDs of the best-fitting DRW ($\alpha_{\rm PSD} = -2.0$) and Matérn ($\alpha_{\rm PSD} = -2.6$) models are shown with dashed–dotted and dotted lines, respectively. The characteristic frequencies of the transition to white noise are shown for both fitted models.

approach, similar to the procedure employed by Haggard et al. (2019). We generate 5×10^4 realizations of the light curves from the best-fitting models, sampled with the original sampling windows of the ALMA A1 data on 2017 April 6, 7, and 11. We use `astroML` (Vanderplas et al. 2012) for the DRW and `Stheno` for the Matérn process light-curve generation. We then calculate the L-S periodogram for each synthetic light curve with `Astropy` (Astropy Collaboration et al. 2018) and compare the results with the L-S periodograms calculated for the actual Sgr A* light-curve data sets. We performed this test for the FULL HI DRW and Matérn fits, as well as for the 2005–2019 combined DRW fit. The example periodograms for the latter model are presented in the top row of Figure 14, along with the residuals between the median L-S value for the DRW model and the value estimated for the observations (middle and bottom rows). The ideal PSD of the DRW model is shown with blue dashed lines. Given the large model correlation timescale with respect to light-curve duration, the ideal DRW PSD effectively corresponds to an almost constant slope of $\alpha_{\rm PSD} = -2$. Hence, all of the intricate structure of the median DRW periodogram inferred from synthetic light curves (black curve), clearly reflected also in the L-S periodograms of the real observations (red curve), can be attributed to the limited and irregular sampling alone. This is visible more clearly in the middle row of Figure 14. No L-S normalized periodogram peak on either of the observing nights indicates deviation by more than 3σ from the aperiodic model predictions. However, when we consider residuals of an unnormalized periodogram (Figure 14, bottom row), in which the PSD represents the amount of variability in physical units (and hence the periodogram test is sensitive to the overall scaling of variance), we see big differences between the days. While 2017 April 6 and 7 are rather calm in comparison to the global fit predictions, the flaring day of 2017 April 11 now shows far more variability than the fit would predict. This variability increase is, however, affecting the whole PSD, not just any selected characteristic frequency. While the fit to all of the 2005–2019 data is shown in Figure 14, these findings are consistent for the other considered models (Matérn and DRW fitted to the EHT 2017 data). We conclude that the amount of variability on the flaring day is not properly described with any of the best-fit models fitted to the broader data sets.

The variability increase on 2017 April 11 was seen already in Table 1 (standard deviations on 2017 April 11 increased 2–3 times) and in Section 4.3 (long-timescale variance was enhanced by a factor of $\sim$10). If we quantify the periodogram consistency with the Monte Carlo model periodogram test, described by Uttley et al. (2002), the DRW model fitted to all of the 2005–2019 data is 99.90% inconsistent with the 2017 April 11 data (the FULL DRW fit to 2017 April data is inconsistent at 100.00% and the Matérn fit to 2017 April data at 98.71%). All best-fitting models are consistent with all the remaining observing days, bands, and reduction pipelines. This particularly strong variability of Sgr A* on 2017 April 11 motivated restricting the first analysis of the EHT VLBI observations to 2017 April 6 and 7, where static imaging (Paper III) and modeling (Paper IV) techniques are more straightforwardly applicable.

7. Summary and Discussion

We have developed algorithms to generate light-curve data from observations with phased interferometric arrays, enabling simultaneous participation in VLBI observations. We apply them here and present the high-cadence and high-S/N 1.3 mm light curves of Sgr A* obtained during the EHT observing campaign in 2017 April with ALMA and SMA. There are several noteworthy conclusions:

1. With the very high S/N of ALMA, thermal noise is not limiting in the analysis. However, significant systematic uncertainties related to the data calibration persist. We elucidate that issue by comparing three independent data reduction pipelines (two for ALMA, one for SMA). While we show general consistency between them, some results, such as the GP correlation timescales (τ) or the presence of SF break timescales, are sensitive to the pipeline choice. We notice overall better performance from the intrafield calibration method A1 (more robust against uncertainties related to low elevation, better consistency with the independently measured SMA flux densities) and conclude that the A1 method should be preferred for future analyses of this nature.
2. During the EHT observations on 2017 April 5–11, Sgr A* exhibited a low flux density of 2.4 ± 0.2 Jy and overall low variability, $\sigma/\mu < 10\%$. The modulation index, σ/μ, is consistent with other observations in 2005–2019. On 2017 April 11, the ALMA observations immediately followed an X-ray flare, with the mm flux density growing by about 50% and reaching a peak flux density $\sim$2.2 hr after the X-ray flare maximum. We observe strongly enhanced variability across multiple timescales on that day, with a near-order-of-magnitude increase in the variance. The statistical PSD properties of the 2017 April 11 observations are inconsistent with those of the GP models fitted to the Sgr A* light-curve data sets.
3. We measure the average spectral index at 220 GHz to be $\alpha = 0.0 \pm 0.1$, where the uncertainties are dominated by the calibration systematics and by the rapid time

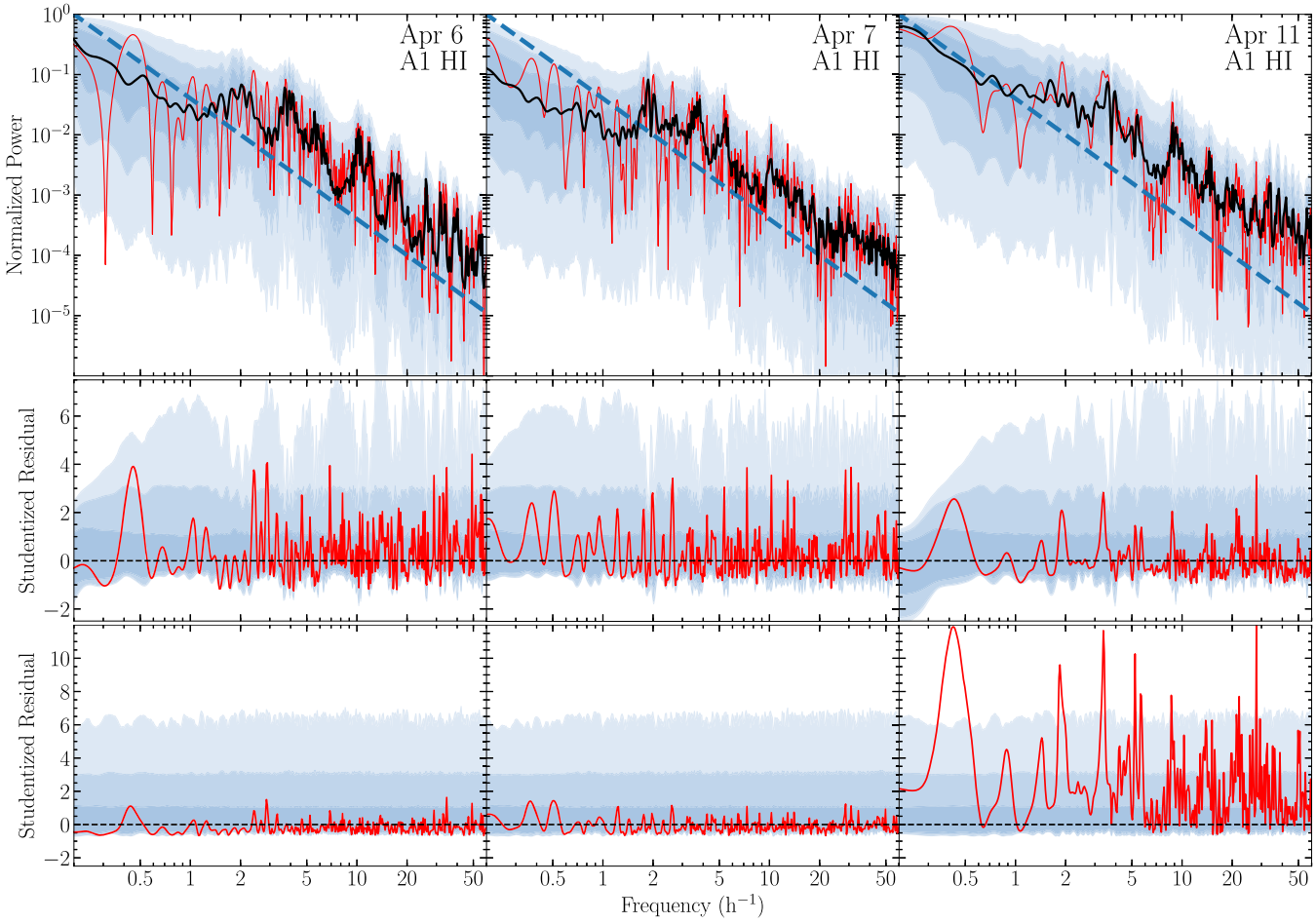

Figure 14. Top: the normalized L-S periodograms for the A1 pipeline HI band data are shown with red lines. The median value of the L-S periodogram, corresponding to a DRW fit to all 2005–2019 data, is shown with black lines. Shaded areas indicate 68.0%, 95.0%, and 99.7% intervals for the L-S periodogram of the DRW model, evaluated with a Monte Carlo procedure. The dashed line represents the ideal PSD of the considered DRW model. Middle: studentized residuals between the data and the median DRW power for a normalized L-S periodogram. The vertical axis is in units of the standard deviation. Bottom: similar to the middle row, but with an unnormalized (physical units) L-S periodogram, showing the overall excess of power on 2017 April 11.

variability of the spectral index, wandering between ± 0.2 on a timescale of $\sim$1 hr. The spectral index immediately following the X-ray flare of 2017 April 11 is significantly lower, -0.25 ± 0.10.

4. No statistically significant autocorrelations are found. If detected, these persistent correlations could be attributed to the presence of the photon shell in the strongly curved spacetime around the black hole. They continue to be expected if sufficiently long observations are aggregated, e.g., from stacking high-cadence ALMA observations over multiple years.
5. There are no time lags detected between the observed frequency bands (between 213 and 229 GHz), indicating that the source is essentially optically thin all the way to the event horizon at the observing frequencies, possibly with irregular patches of higher optical depth evolving on dynamical timescales. This is also consistent with the spectral index variability signatures.
6. With the high cadence of our light curves, we are able to track the short-timescale variability of Sgr A*, confirming a red-noise characteristic across timescales from a single minute to several hours. Furthermore, we see a convincing indication of a PSD slope of 2.6 ± 0.3 for short timescales, steeper than the commonly employed DRW model. There is a mutual consistency between the Matérn process fit to the observations, the SF analysis results, and the predictions from the GRMHD simulations. In the SF analysis, we additionally observe a potential power-law break at a 0.15–0.30 hr timescale, which may approximate the steepening PSD slope of the Matérn process or indicate a superposition of distinct stochastic processes.
7. Aperiodic GP models fitted to the data provide good-quality fits and generally capture the spectral properties of the light curves well. However, the 2017 April 11 observations indicate too much variability to be represented with the same models as the other days. The correlation timescale is not consistently constrained between different considered models. The DRW fit to the collection of observations from 2005 to 2019 gives $\tau = 20.7^{+3.2}_{-3.5}$ hr, while correlations on even longer timescales are hinted at in the long-term monitoring results. For example, four different projects observing between 2016 August and 2017 October all report flux densities below the long-term mean. At the same time, the DRW fit to EHT 2017 data gives $\tau = 8.1^{+5.8}_{-1.7}$ hr, while the Matérn process fits find shorter timescales of $\tau = 1.8^{+5.0}_{-0.4}$ hr. We conclude that the correlation timescale remains poorly constrained. Along with the 2017

April 11 inconsistency, this may suggest that the assumption of a single stationary statistical process is incorrect when different epochs (or different source activity states) are combined.

Overall, the light-curve analysis presented in this paper indicates that during the 2017 EHT observing campaign Sgr A* was in a low-luminosity state with respect to the 2005–2019 average of 3.2 ± 0.6 Jy, implying low optical depth, and thus strengthening the case for event horizon scale imaging with the VLBI data. The source displayed an average amount of variability on 2017 April 5–10. Hence, we expect that the VLBI analysis of 2017 April 6–7 data, presented in Papers I, II, III, IV, V, and VI, should reveal a representative event horizon scale morphology of the source during a nonflaring low-variability period. Nevertheless, we see intrinsic source variability on timescales as short as 1 minute, which may affect the EHT VLBI observations in a nontrivial way, and we argue that these impacts must be mitigated at the data analysis stage (Paper IV; Broderick et al. 2022; Farah et al. 2022). On 2017 April 11, Sgr A* displayed significantly enhanced variability in the aftermath of a strong X-ray flare. This different state may impact Sgr A*'s event horizon scale morphology, and the excess variability on that day may undermine our ability to define a mean static image.

The measured source variability is expected to be related mostly to the intrinsic variability of the compact source, with a small subdominant contribution from the interstellar medium scattering screen (order of 1%; Johnson et al. 2018). Hence, it is possible to use GRMHD simulations of Sgr A* to make a direct comparison of the observed variability metrics reported in this paper with the predictions from numerical models. This approach has been pursued in Paper V, revealing a rather puzzling disagreement—numerical GRMHD simulations seem to produce systematically more variability than what we measure in the Sgr A* light curves; see the discussion in Paper V.

During this campaign, ALMA also recorded Sgr A*'s total intensity light curves and full polarization data. The analysis of that data set, interesting particularly in the context of polarization loops hypothetically associated with the orbital motion in the innermost accretion flow region (Marrone et al. 2006; Gravity Collaboration et al. 2018b), will be presented elsewhere. More light-curve data of similar or improved quality will be delivered with the subsequent EHT VLBI observing campaigns, advancing our understanding of the statistical properties of Sgr A* variability at mm wavelengths and of Galactic Center physics.

We thank Yuhei Iwata, Lena Murchikova, Rebecca Phillipson, and Chris White for comments and discussions, as well as Alexandra Elbakyan for her contributions to the open science initiative. We also thank the anonymous ApJL referee for helpful and constructive comments. The Event Horizon Telescope Collaboration thanks the following organizations and programs: National Science Foundation (awards OISE-1743747, AST-1816420, AST-1716536, AST-1440254, AST-1935980); the Black Hole Initiative, which is funded by grants from the John Templeton Foundation and the Gordon and Betty Moore Foundation (although the opinions expressed in this work are those of the author(s) and do not necessarily reflect the views of these foundations); NASA Hubble Fellowship grant HST-HF2-51431.001-A awarded by the Space Telescope Science Institute, which is operated by the Association of Universities for Research in Astronomy, Inc., for NASA, under contract NAS5-26555; the Academy of Finland (projects 274477, 284495, 312496, 315721); the Agencia Nacional de Investigación y Desarrollo (ANID), Chile via NCN19_058 (TITANs) and Fondecyt 3190878, the Alexander von Humboldt Stiftung; an Alfred P. Sloan Research Fellowship; Allegro, the European ALMA Regional Centre node in the Netherlands, the NL astronomy research network NOVA and the astronomy institutes of the University of Amsterdam, Leiden University, and Radboud University; the China Scholarship Council; Consejo Nacional de Ciencia y Tecnología (CONACYT, Mexico, projects U0004-246083, U0004-259839, F0003-272050, M0037-279006, F0003-281692, 104497, 275201, 263356); the Delaney Family via the Delaney Family John A. Wheeler Chair at Perimeter Institute; Dirección General de Asuntos del Personal Académico—Universidad Nacional Autónoma de México (DGAPA—UNAM, projects IN112417 and IN112820); the European Research Council Synergy Grant "BlackHoleCam: Imaging the Event Horizon of Black Holes" (grant 610058); the Generalitat Valenciana postdoctoral grant APOSTD/2018/177 and GenT Program (project CIDEGENT/2018/021); MICINN Research Project PID2019-108995GB-C22; the European Research Council for advanced grant "JETSET: Launching, propagation and emission of relativistic jets from binary mergers and across mass scales" (grant No. 884631); the Istituto Nazionale di Fisica Nucleare (INFN) sezione di Napoli, iniziative specifiche TEONGRAV; the two Dutch National Supercomputers, Cartesius and Snellius (NWO grant 2021.013); the International Max Planck Research School for Astronomy and Astrophysics at the Universities of Bonn and Cologne; DFG research grant "Jet physics on horizon scales and beyond" (grant No. FR 4069/2-1); Joint Princeton/Flatiron and Joint Columbia/Flatiron Postdoctoral Fellowships, with research at the Flatiron Institute supported by the Simons Foundation; the Japanese Government (Monbukagakusho: MEXT) Scholarship; the Japan Society for the Promotion of Science (JSPS) Grant-in-Aid for JSPS Research Fellowship (JP17J08829); the Key Research Program of Frontier Sciences, Chinese Academy of Sciences (CAS, grants QYZDJ-SSW-SLH057, QYZDJ-SSW-SYS008, ZDBS-LY-SLH011); the Leverhulme Trust Early Career Research Fellowship; the Max-Planck-Gesellschaft (MPG); the Max Planck Partner Group of the MPG and the CAS; the MEXT/JSPS KAKENHI (grants 18KK0090, JP21H01137, JP18H03721, 18K03709, 18H01245, 25120007); the Malaysian Fundamental Research Grant Scheme (FRGS) FRGS/1/2019/STG02/UM/02/6; the MIT International Science and Technology Initiatives (MISTI) Funds; the Ministry of Science and Technology (MOST) of Taiwan (103-2119-M-001-010-MY2, 105-2112-M-001-025-MY3, 105-2119-M-001-042, 106-2112-M-001-011, 106-2119-M-001-013, 106-2119-M-001-027, 106-2923-M-001-005, 107-2119-M-001-017, 107-2119-M-001-020, 107-2119-M-001-041, 107-2119-M-110-005, 107-2923-M-001-009, 108-2112-M-001-048, 108-2112-M-001-051, 108-2923-M-001-002, 109-2112-M-001-025, 109-2124-M-001-005, 109-2923-M-001-001, 110-2112-M-003-007-MY2, 110-2112-M-001-033, 110-2124-M-001-007, and 110-2923-M-001-001); the Ministry of Education (MoE) of Taiwan Yushan Young Scholar Program; the Physics Division, National Center for Theoretical Sciences of Taiwan; the National Aeronautics and Space Administration (NASA, Fermi Guest Investigator grant 80NSSC20K1567, NASA Astrophysics Theory Program grant 80NSSC20K0527, NASA NuSTAR award 80NSSC20K0645); the National Institute of Natural Sciences

(NINS) of Japan; the National Key Research and Development Program of China (grants 2016YFA0400704 and 2016YFA0400702); the National Science Foundation (NSF, grants AST-0096454, AST-0352953, AST-0521233, AST-0705062, AST-0905844, AST-0922984, AST-1126433, AST-1140030, DGE-1144085, AST-1207704, AST-1207730, AST-1207752, MRI-1228509, OPP-1248097, AST-1310896, AST-1555365, AST-1615796, AST-1715061, AST-1716327, AST-1903847, AST-2034306); the Natural Science Foundation of China (grants 11650110427, 10625314, 11721303, 11725312, 11933007, 11991052, 11991053); NWO grant No. OCENW.KLEIN.113; a fellowship of China Postdoctoral Science Foundation (2020M671266); the Natural Sciences and Engineering Research Council of Canada (NSERC, including a Discovery Grant and the NSERC Alexander Graham Bell Canada Graduate Scholarships-Doctoral Program); the National Youth Thousand Talents Program of China; the National Research Foundation of Korea (the Global PhD Fellowship Grant: grants NRF-2015H1A2A1033752, 2015-R1D1A1A01056807; the Korea Research Fellowship Program: NRF-2015H1D3A1066561, Basic Research Support Grant 2019R1F1A1059721); the Netherlands Organization for Scientific Research (NWO) VICI award (grant 639.043.513) and Spinoza Prize SPI 78-409; the New Scientific Frontiers with Precision Radio Interferometry Fellowship awarded by the South African Radio Astronomy Observatory (SARAO), which is a facility of the National Research Foundation (NRF), an agency of the Department of Science and Technology (DST) of South Africa; the Onsala Space Observatory (OSO) national infrastructure, for the provisioning of its facilities/observational support (OSO receives funding through the Swedish Research Council under grant 2017-00648); the Perimeter Institute for Theoretical Physics (research at Perimeter Institute is supported by the Government of Canada through the Department of Innovation, Science and Economic Development and by the Province of Ontario through the Ministry of Research, Innovation and Science); the Spanish Ministerio de Ciencia e Innovaci-n (grants PGC2018-098915-B-C21, AYA2016-80889-P, PID2019-108995GB-C21, PID2020-117404GB-C21); the State Agency for Research of the Spanish MCIU through the "Center of Excellence Severo Ochoa" award for the Instituto de Astrofísica de Andalucía (SEV-2017-0709); the Toray Science Foundation; the Consejería de Economía, Conocimiento, Empresas y Universidad of the Junta de Andalucía (grant P18-FR-1769), the Consejo Superior de Investigaciones Científicas (grant 2019AEP112); the M2FINDERS project, which has received funding by the European Research Council (ERC) under the European Union's Horizon 2020 Research and Innovation Programme (grant agreement No. 101018682); the US Department of Energy (USDOE) through the Los Alamos National Laboratory (operated by Triad National Security, LLC, for the National Nuclear Security Administration of the USDOE (contract 89233218CNA000001); the European Union's Horizon 2020 research and innovation program under grant agreement No. 730562 RadioNet; Shanghai Pilot Program for Basic Research, Chinese Academy of Science, Shanghai Branch (JCYJ-SHFY-2021-013); ALMA North America Development Fund; the Academia Sinica; Chandra DD7-18089X and TM6-17006X; and the GenT Program (Generalitat Valenciana) Project CIDEGENT/2018/021. This work used the Extreme Science and Engineering Discovery Environment (XSEDE), supported by NSF grant ACI-1548562, and CyVerse, supported by NSF grants DBI-0735191, DBI-1265383, and DBI-1743442. XSEDE Stampede2 resource at TACC was allocated through TG-AST170024 and TG-AST080026N. XSEDE JetStream resource at PTI and TACC was allocated through AST170028. The simulations were performed in part on the SuperMUC cluster at the LRZ in Garching, on the LOEWE cluster in CSC in Frankfurt, and on the HazelHen cluster at the HLRS in Stuttgart. This research was enabled in part by support provided by Compute Ontario (http://computeontario.ca), Calcul Quebec (http://www.calculquebec.ca), and Compute Canada (http://www.computecanada.ca). C.C. acknowledges support from the Swedish Research Council (VR). We thank the staff at the participating observatories, correlation centers, and institutions for their enthusiastic support. This paper makes use of the following ALMA data: ADS/JAO.ALMA#2016.1.01154.V. ALMA is a partnership of the European Southern Observatory (ESO; Europe, representing its member states), NSF, and National Institutes of Natural Sciences of Japan, together with National Research Council (Canada), Ministry of Science and Technology (MOST; Taiwan), Academia Sinica Institute of Astronomy and Astrophysics (ASIAA; Taiwan), and Korea Astronomy and Space Science Institute (KASI; Republic of Korea), in cooperation with the Republic of Chile. The Joint ALMA Observatory is operated by ESO, Associated Universities, Inc. (AUI)/NRAO, and the National Astronomical Observatory of Japan (NAOJ). The NRAO is a facility of the NSF operated under cooperative agreement by AUI. Support for this work was also provided by the NASA Hubble Fellowship grant HST-HF2-51431.001-A awarded by the Space Telescope Science Institute, which is operated by the Association of Universities for Research in Astronomy, Inc., for NASA, under contract NAS5-26555. Hector Olivares and Gibwa Musoke were supported by Virtual Institute of Accretion (VIA) postdoctoral fellowships from the Netherlands Research School for Astronomy (NOVA). APEX is a collaboration between the Max-Planck-Institut für Radioastronomie (Germany), ESO, and the Onsala Space Observatory (Sweden). The SMA is a joint project between the SAO and ASIAA and is funded by the Smithsonian Institution and the Academia Sinica. The JCMT is operated by the East Asian Observatory on behalf of the NAOJ, ASIAA, and KASI, as well as the Ministry of Finance of China, Chinese Academy of Sciences, and the National Key R&D Program (No. 2017YFA0402700) of China. Additional funding support for the JCMT is provided by the Science and Technologies Facility Council (UK) and participating universities in the UK and Canada. Simulations were performed in part on the SuperMUC cluster at the LRZ in Garching, on the LOEWE cluster in CSC in Frankfurt, on the HazelHen cluster at the HLRS in Stuttgart, and on the Pi2.0 and Siyuan Mark-I at Shanghai Jiao Tong University. The computer resources of the Finnish IT Center for Science (CSC) and the Finnish Computing Competence Infrastructure (FCCI) project are acknowledged. Junghwan Oh was supported by the Basic Science Research Program through the National Research Foundation of Korea (NRF) funded by the Ministry of Education (NRF-2021R1A6A3A01086420). We thank Martin Shepherd for the addition of extra features in the Difmap software that were used for the CLEAN imaging results presented in this paper. The computing cluster of Shanghai VLBI correlator supported by the Special Fund for Astronomy from the Ministry of Finance in China is acknowledged. The LMT is a project operated by the Instituto Nacional de Astrífisica, Óptica, y Electrínica (Mexico) and the University of Massachusetts at Amherst (USA). The IRAM 30 m telescope on Pico Veleta, Spain, is operated by IRAM and supported by CNRS (Centre National de la Recherche Scientifique, France), MPG

(Max-Planck- Gesellschaft, Germany), and IGN (Instituto Geográfico Nacional, Spain). The SMT is operated by the Arizona Radio Observatory, a part of the Steward Observatory of the University of Arizona, with financial support of operations from the State of Arizona and financial support for instrumentation development from the NSF. Support for SPT participation in the EHT is provided by the National Science Foundation through award OPP-1852617 to the University of Chicago. Partial support is also provided by the Kavli Institute of Cosmological Physics at the University of Chicago. The SPT hydrogen maser was provided on loan from the GLT, courtesy of ASIAA. Support for this work was provided by NASA through the NASA Hubble Fellowship grant No. HST–HF2ers. This research has made use of NASA's Astrophysics Data System. We gratefully acknowledge the support provided by the extended staff–51494.001 awarded by the Space Telescope Science Institute, which is operated by the Association of Universities for Research in Astronomy, Inc., for NASA, under contract NAS5-26555. The EHTC has received generous donations of FPGA chips from Xilinx Inc., under the Xilinx University Program. The EHTC has benefited from technology shared under open-source license by the Collaboration for Astronomy Signal Processing and Electronics Research (CASPER). The EHT project is grateful to T4Science and Microsemi for their assistance with Hydrogen Mas of the ALMA, both from the inception of the ALMA Phasing Project through the observational campaigns of 2017 and 2018. We would like to thank A. Deller and W. Brisken for EHT-specific support with the use of DiFX. We acknowledge the significance that Maunakea, where the SMA and JCMT EHT stations are located, has for the indigenous Hawaiian people.

Appendix A
Light-curve Feedback on the EHT VLBI Data Calibration

Rapid variability in Sgr A* light curves affects the VLBI observations of the EHT as a modulation of the total intensity of the compact source resolved on the VLBI baselines. A detailed measurement of the mm light curve can therefore help inform simultaneous VLBI observations. For a sparse network like the EHT, the additional a priori information provided by time-dependent total intensity light curves can be of paramount importance for a successful reconstruction of the compact source structure. We make use of the light-curve results for the VLBI data calibration in several ways. ALMA gains (G_t) derived as a by-product of the A1 pipeline through intrafield calibration (Section 2.1) were used to produce ALMA a priori amplitude calibration metadata (ANTAB tables, Paper II), updated with respect to the standard ALMA QA2 tables derived under the constant flux density assumption (Goddi et al. 2019). Moreover, the EHT array contains pairs of nearby stations providing intrasite baselines that do not resolve Sgr A* and effectively measure a total compact flux density equal to the light-curve amplitude up to the VLBI calibration station-based gain errors. Using light-curve information as a prior, all stations with a co-observing intrasite companion (ALMA, SMA, the Atacama Pathfinder Experiment [APEX], and the James Clerk Maxwell Telescope [JCMT]) can be absolutely flux-calibrated by way of "network calibration" constraints (Blackburn et al. 2019) that do not depend on any a priori VLBI station calibration. To that end, the combined light curves spanning the entire duration of the VLBI observations were constructed by merging the A1 and SM pipeline results (Sections 2.1 and 2.3), after removing constant offsets between the pipelines (Section 3, Table 4). A smoothed continuous representation of each full-day light curve was then generated through a smoothing spline interpolation (`SciPy`; Virtanen et al. 2020) and employed for the time-dependent network calibration. Similarly, light curves provide a natural variable flux density scaling for simple a priori source models suitable for initial self-calibration of the shortest intersite EHT baselines. For the EHT VLBI observations of Sgr A*, such an approach was used to mitigate poor amplitude calibration of the Large Millimeter Telescope (LMT; M87* Paper III), through modeling visibilities on the shortest baseline (<2 Gλ) to a well-calibrated SMT station with a Gaussian (Paper II). The size of the Gaussian was selected based on the previous VLBI measurements (Johnson et al. 2018) and the pre-imaging constraints derived for the 2017 data set (Paper II). Finally, the effect of total compact flux density modulation can be mitigated in the calibrated VLBI data sets by uniformly renormalizing visibility amplitudes on all baselines by the time-dependent light curves. In this way, a significant contribution to the total source intrinsic variability is removed (Broderick et al. 2022; Georgiev et al. 2022), increasing the robustness of imaging and modeling observations of Sgr A* with a static source model (Paper III; Paper IV). All calibration procedures described above were applied separately to data from the LO and HI frequency bands, in which EHT VLBI observations were performed in 2017 (M87* Paper II).

Appendix B
Full-bandwidth SMA Data

In this paper, we presented SMA light-curve results corresponding to the VLBI observing bands, LO at 227.1 GHz and H I at 229.1 GHz. However, the SMA observed Sgr A* with a particularly wide band, with four subbands, 2 GHz wide in the 208.1–216.1 GHz range, and another four subbands in the 224.1–232.1 GHz range. Since these data confirm the findings obtained for the SMA LO and HI bands, and the correlation between separate SMA subbands is overall very high, we only briefly comment on the entire SMA data set in this appendix. A wide SMA bandwidth is particularly useful for measuring the spectral index. We estimate it using linear regression on amplitudes in all eight subbands, for each separate time stamp. In Figure 15, we show the SMA results alongside the ALMA spectral index measurements, reported in Section 3.3. The error bars correspond to the sample standard deviation in the spectral index distribution. Hence, they capture the intrinsic time variability of the spectral index on top of the statistical uncertainties. We find the SMA spectral index to be consistent with zero, which corroborates the ALMA results (Section 3.3).

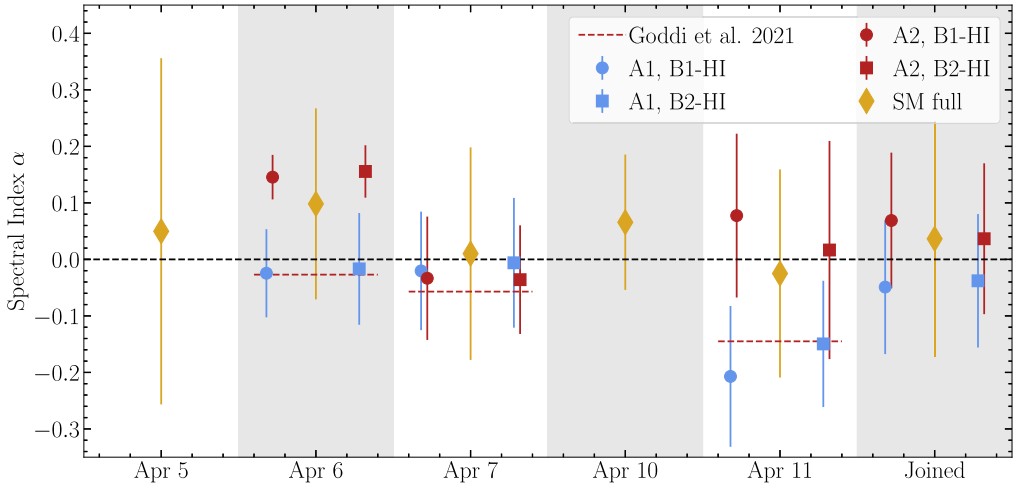

Figure 15. The spectral index measured from the 220 GHz light curves of Sgr A* in 2017 April. The ALMA data points follow values reported in Figure 5. The SMA results were obtained by fitting to all of the eight subbands with frequencies ranging from 208.1 to 232.1 GHz.

Appendix C
Model-fitting Corner Plots

In Figure 16, we present the posterior distribution corner plots corresponding to the fiducial fits to the entire EHT 2017 Sgr A* light-curve data set, FULL H I in Table 10. These corner plots correspond to the two different GP models discussed in Section 5, fitted to the observational data with a nested sampling posterior exploration algorithm.

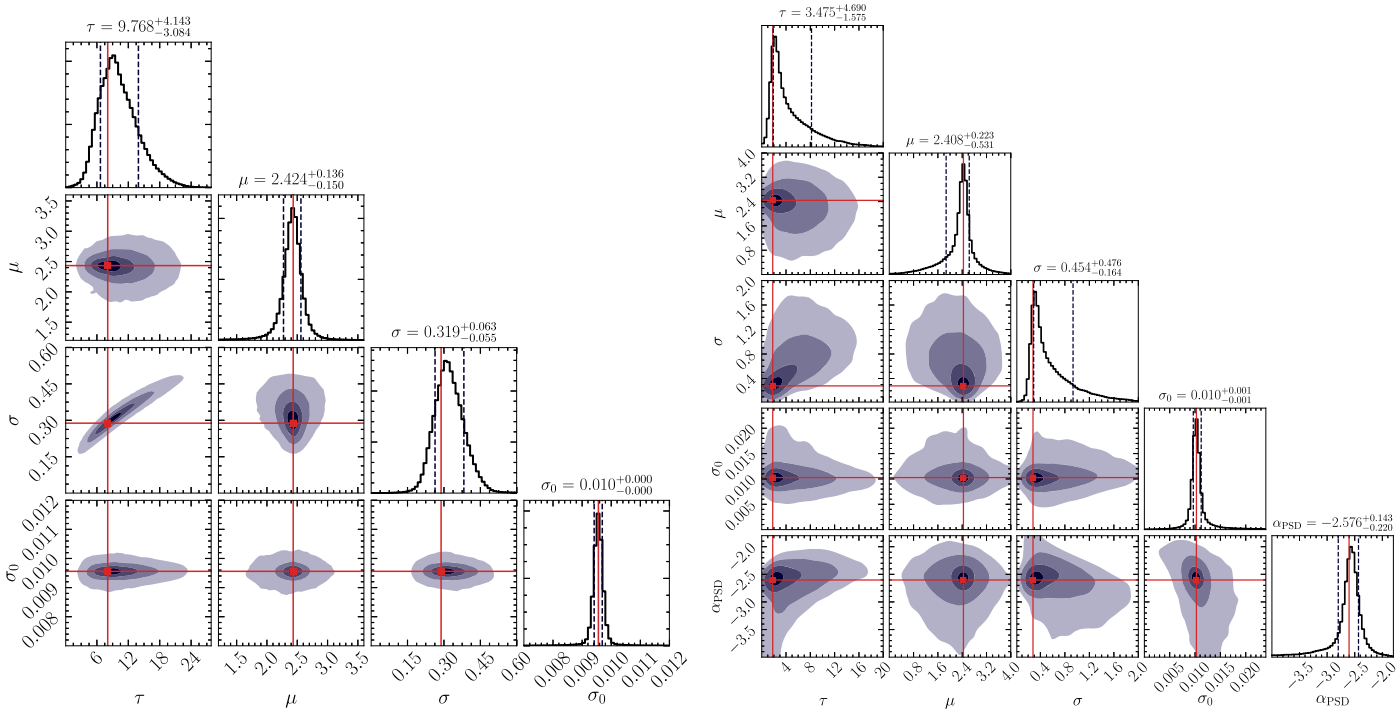

Figure 16. Left: the DRW model best-fit to the EHT light curves of Sgr A*. Contours correspond to 0.2, 0.5, 0.8, and 0.95 of the posterior volume; values of median estimators on the marginalized posteriors are presented. The red line corresponds to the ML estimator, reported in Table 10. Right: same as the left panel, but for the Matérn process model fit.

ORCID iDs

Maciek Wielgus https://orcid.org/0000-0002-8635-4242
Nicola Marchili https://orcid.org/0000-0002-5523-7588
Iván Martí-Vidal https://orcid.org/0000-0003-3708-9611
Garrett K. Keating https://orcid.org/0000-0002-3490-146X
Venkatessh Ramakrishnan https://orcid.org/0000-0002-9248-086X
Paul Tiede https://orcid.org/0000-0003-3826-5648
Ed Fomalont https://orcid.org/0000-0002-9036-2747
Sara Issaoun https://orcid.org/0000-0002-5297-921X
Joey Neilsen https://orcid.org/0000-0002-8247-786X
Michael A. Nowak https://orcid.org/0000-0001-6923-1315
Lindy Blackburn https://orcid.org/0000-0002-9030-642X
Charles F. Gammie https://orcid.org/0000-0001-7451-8935
Ciriaco Goddi https://orcid.org/0000-0002-2542-7743
Daryl Haggard https://orcid.org/0000-0001-6803-2138
Daeyoung Lee https://orcid.org/0000-0002-3350-5588
Monika Moscibrodzka https://orcid.org/0000-0002-4661-6332
Alexandra J. Tetarenko https://orcid.org/0000-0003-3906-4354
Geoffrey C. Bower https://orcid.org/0000-0003-4056-9982
Chi-kwan Chan https://orcid.org/0000-0001-6337-6126
Koushik Chatterjee https://orcid.org/0000-0002-2825-3590
Paul M. Chesler https://orcid.org/0000-0001-6327-8462
Jason Dexter https://orcid.org/0000-0003-3903-0373
Sheperd S. Doeleman https://orcid.org/0000-0002-9031-0904
Boris Georgiev https://orcid.org/0000-0002-3586-6424
Mark Gurwell https://orcid.org/0000-0003-0685-3621
Michael D. Johnson https://orcid.org/0000-0002-4120-3029
Daniel P. Marrone https://orcid.org/0000-0002-2367-1080
Alejandro Mus https://orcid.org/0000-0003-0329-6874
Dimitrios Psaltis https://orcid.org/0000-0003-1035-3240
Bart Ripperda https://orcid.org/0000-0002-7301-3908
Gunther Witzel https://orcid.org/0000-0003-2618-797X
Kazunori Akiyama https://orcid.org/0000-0002-9475-4254
Antxon Alberdi https://orcid.org/0000-0002-9371-1033
Juan Carlos Algaba https://orcid.org/0000-0001-6993-1696
Richard Anantua https://orcid.org/0000-0003-3457-7660
Keiichi Asada https://orcid.org/0000-0001-6988-8763
Rebecca Azulay https://orcid.org/0000-0002-2200-5393
Uwe Bach https://orcid.org/0000-0002-7722-8412
Anne-Kathrin Baczko https://orcid.org/0000-0003-3090-3975
Mislav Baloković https://orcid.org/0000-0003-0476-6647
John Barrett https://orcid.org/0000-0002-9290-0764
Michi Bauböck https://orcid.org/0000-0002-5518-2812
Bradford A. Benson https://orcid.org/0000-0002-5108-6823
Raymond Blundell https://orcid.org/0000-0002-5929-5857
Katherine L. Bouman https://orcid.org/0000-0003-0077-4367
Hope Boyce https://orcid.org/0000-0002-6530-5783
Christiaan D. Brinkerink https://orcid.org/0000-0002-2322-0749
Roger Brissenden https://orcid.org/0000-0002-2556-0894
Silke Britzen https://orcid.org/0000-0001-9240-6734
Avery E. Broderick https://orcid.org/0000-0002-3351-760X
Thomas Bronzwaer https://orcid.org/0000-0003-1151-3971
Sandra Bustamante https://orcid.org/0000-0001-6169-1894
Do-Young Byun https://orcid.org/0000-0003-1157-4109
John E. Carlstrom https://orcid.org/0000-0002-2044-7665
Chiara Ceccobello https://orcid.org/0000-0002-4767-9925
Andrew Chael https://orcid.org/0000-0003-2966-6220
Shami Chatterjee https://orcid.org/0000-0002-2878-1502
Ming-Tang Chen https://orcid.org/0000-0001-6573-3318
Yongjun Chen (陈永军) https://orcid.org/0000-0001-5650-6770
Ilje Cho https://orcid.org/0000-0001-6083-7521
Pierre Christian https://orcid.org/0000-0001-6820-9941
Nicholas S. Conroy https://orcid.org/0000-0003-2886-2377
John E. Conway https://orcid.org/0000-0003-2448-9181
James M. Cordes https://orcid.org/0000-0002-4049-1882
Thomas M. Crawford https://orcid.org/0000-0001-9000-5013
Geoffrey B. Crew https://orcid.org/0000-0002-2079-3189
Alejandro Cruz-Osorio https://orcid.org/0000-0002-3945-6342
Yuzhu Cui https://orcid.org/0000-0001-6311-4345
Jordy Davelaar https://orcid.org/0000-0002-2685-2434
Mariafelicia De Laurentis https://orcid.org/0000-0002-9945-682X
Roger Deane https://orcid.org/0000-0003-1027-5043
Jessica Dempsey https://orcid.org/0000-0003-1269-9667
Gregory Desvignes https://orcid.org/0000-0003-3922-4055
Vedant Dhruv https://orcid.org/0000-0001-6765-877X
Sergio A. Dzib https://orcid.org/0000-0001-6010-6200
Ralph P. Eatough https://orcid.org/0000-0001-6196-4135
Razieh Emami https://orcid.org/0000-0002-2791-5011
Heino Falcke https://orcid.org/0000-0002-2526-6724
Joseph Farah https://orcid.org/0000-0003-4914-5625
Vincent L. Fish https://orcid.org/0000-0002-7128-9345
H. Alyson Ford https://orcid.org/0000-0002-9797-0972
Raquel Fraga-Encinas https://orcid.org/0000-0002-5222-1361
Per Friberg https://orcid.org/0000-0002-8010-8454
Christian M. Fromm https://orcid.org/0000-0002-1827-1656
Antonio Fuentes https://orcid.org/0000-0002-8773-4933
Peter Galison https://orcid.org/0000-0002-6429-3872
Roberto García https://orcid.org/0000-0002-6584-7443
Roman Gold https://orcid.org/0000-0003-2492-1966
Arturo I. Gómez-Ruiz https://orcid.org/0000-0001-9395-1670
José L. Gómez https://orcid.org/0000-0003-4190-7613
Minfeng Gu (顾敏峰) https://orcid.org/0000-0002-4455-6946
Kazuhiro Hada https://orcid.org/0000-0001-6906-772X
Michael H. Hecht https://orcid.org/0000-0002-4114-4583
Ronald Hesper https://orcid.org/0000-0003-1918-6098
Luis C. Ho (何子山) https://orcid.org/0000-0001-6947-5846
Paul Ho https://orcid.org/0000-0002-3412-4306
Mareki Honma https://orcid.org/0000-0003-4058-9000
Chih-Wei L. Huang https://orcid.org/0000-0001-5641-3953
Lei Huang (黄磊) https://orcid.org/0000-0002-1923-227X
Shiro Ikeda https://orcid.org/0000-0002-2462-1448
C. M. Violette Impellizzeri https://orcid.org/0000-0002-3443-2472
Makoto Inoue https://orcid.org/0000-0001-5037-3989
David J. James https://orcid.org/0000-0001-5160-4486
Buell T. Jannuzi https://orcid.org/0000-0002-1578-6582
Michael Janssen https://orcid.org/0000-0001-8685-6544
Britton Jeter https://orcid.org/0000-0003-2847-1712

Wu Jiang (江悟) https://orcid.org/0000-0001-7369-3539
Alejandra Jiménez-Rosales https://orcid.org/0000-0002-2662-3754
Svetlana Jorstad https://orcid.org/0000-0001-6158-1708
Abhishek V. Joshi https://orcid.org/0000-0002-2514-5965
Taehyun Jung https://orcid.org/0000-0001-7003-8643
Mansour Karami https://orcid.org/0000-0001-7387-9333
Ramesh Karuppusamy https://orcid.org/0000-0002-5307-2919
Tomohisa Kawashima https://orcid.org/0000-0001-8527-0496
Mark Kettenis https://orcid.org/0000-0002-6156-5617
Dong-Jin Kim https://orcid.org/0000-0002-7038-2118
Jae-Young Kim https://orcid.org/0000-0001-8229-7183
Jongsoo Kim https://orcid.org/0000-0002-1229-0426
Junhan Kim https://orcid.org/0000-0002-4274-9373
Motoki Kino https://orcid.org/0000-0002-2709-7338
Jun Yi Koay https://orcid.org/0000-0002-7029-6658
Prashant Kocherlakota https://orcid.org/0000-0001-7386-7439
Patrick M. Koch https://orcid.org/0000-0003-2777-5861
Shoko Koyama https://orcid.org/0000-0002-3723-3372
Carsten Kramer https://orcid.org/0000-0002-4908-4925
Michael Kramer https://orcid.org/0000-0002-4175-2271
Thomas P. Krichbaum https://orcid.org/0000-0002-4892-9586
Cheng-Yu Kuo https://orcid.org/0000-0001-6211-5581
Noemi La Bella https://orcid.org/0000-0002-8116-9427
Tod R. Lauer https://orcid.org/0000-0003-3234-7247
Sang-Sung Lee https://orcid.org/0000-0002-6269-594X
Po Kin Leung https://orcid.org/0000-0002-8802-8256
Aviad Levis https://orcid.org/0000-0001-7307-632X
Zhiyuan Li (李志远) https://orcid.org/0000-0003-0355-6437
Rocco Lico https://orcid.org/0000-0001-7361-2460
Greg Lindahl https://orcid.org/0000-0002-6100-4772
Michael Lindqvist https://orcid.org/0000-0002-3669-0715
Mikhail Lisakov https://orcid.org/0000-0001-6088-3819
Jun Liu (刘俊) https://orcid.org/0000-0002-7615-7499
Kuo Liu https://orcid.org/0000-0002-2953-7376
Elisabetta Liuzzo https://orcid.org/0000-0003-0995-5201
Wen-Ping Lo https://orcid.org/0000-0003-1869-2503
Andrei P. Lobanov https://orcid.org/0000-0003-1622-1484
Laurent Loinard https://orcid.org/0000-0002-5635-3345
Colin Lonsdale https://orcid.org/0000-0003-4062-4654
Ru-Sen Lu (路如森) https://orcid.org/0000-0002-7692-7967
Jirong Mao (毛基荣) https://orcid.org/0000-0002-7077-7195
Sera Markoff https://orcid.org/0000-0001-9564-0876
Alan P. Marscher https://orcid.org/0000-0001-7396-3332
Satoki Matsushita https://orcid.org/0000-0002-2127-7880
Lynn D. Matthews https://orcid.org/0000-0002-3728-8082
Lia Medeiros https://orcid.org/0000-0003-2342-6728
Karl M. Menten https://orcid.org/0000-0001-6459-0669
Daniel Michalik https://orcid.org/0000-0002-7618-6556
Izumi Mizuno https://orcid.org/0000-0002-7210-6264
Yosuke Mizuno https://orcid.org/0000-0002-8131-6730
James M. Moran https://orcid.org/0000-0002-3882-4414
Kotaro Moriyama https://orcid.org/0000-0003-1364-3761
Cornelia Müller https://orcid.org/0000-0002-2739-2994
Gibwa Musoke https://orcid.org/0000-0003-1984-189X
Ioannis Myserlis https://orcid.org/0000-0003-3025-9497
Andrew Nadolski https://orcid.org/0000-0001-9479-9957
Hiroshi Nagai https://orcid.org/0000-0003-0292-3645
Neil M. Nagar https://orcid.org/0000-0001-6920-662X
Masanori Nakamura https://orcid.org/0000-0001-6081-2420
Ramesh Narayan https://orcid.org/0000-0002-1919-2730
Gopal Narayanan https://orcid.org/0000-0002-4723-6569
Iniyan Natarajan https://orcid.org/0000-0001-8242-4373
Roberto Neri https://orcid.org/0000-0002-7176-4046
Chunchong Ni https://orcid.org/0000-0003-1361-5699
Aristeidis Noutsos https://orcid.org/0000-0002-4151-3860
Junghwan Oh https://orcid.org/0000-0002-4991-9638
Hiroki Okino https://orcid.org/0000-0003-3779-2016
Héctor Olivares https://orcid.org/0000-0001-6833-7580
Gisela N. Ortiz-León https://orcid.org/0000-0002-2863-676X
Tomoaki Oyama https://orcid.org/0000-0003-4046-2923
Feryal Özel https://orcid.org/0000-0003-4413-1523
Daniel C. M. Palumbo https://orcid.org/0000-0002-7179-3816
Georgios Filippos Paraschos https://orcid.org/0000-0001-6757-3098
Jongho Park https://orcid.org/0000-0001-6558-9053
Harriet Parsons https://orcid.org/0000-0002-6327-3423
Nimesh Patel https://orcid.org/0000-0002-6021-9421
Ue-Li Pen https://orcid.org/0000-0003-2155-9578
Dominic W. Pesce https://orcid.org/0000-0002-5278-9221
Richard Plambeck https://orcid.org/0000-0001-6765-9609
Oliver Porth https://orcid.org/0000-0002-4584-2557
Felix M. Pötzl https://orcid.org/0000-0002-6579-8311
Ben Prather https://orcid.org/0000-0002-0393-7734
Jorge A. Preciado-López https://orcid.org/0000-0002-4146-0113
Hung-Yi Pu https://orcid.org/0000-0001-9270-8812
Ramprasad Rao https://orcid.org/0000-0002-1407-7944
Mark G. Rawlings https://orcid.org/0000-0002-6529-202X
Alexander W. Raymond https://orcid.org/0000-0002-5779-4767
Luciano Rezzolla https://orcid.org/0000-0002-1330-7103
Angelo Ricarte https://orcid.org/0000-0001-5287-0452
Freek Roelofs https://orcid.org/0000-0001-5461-3687
Alan Rogers https://orcid.org/0000-0003-1941-7458
Eduardo Ros https://orcid.org/0000-0001-9503-4892
Cristina Romero-Canizales https://orcid.org/0000-0001-6301-9073
Arash Roshanineshat https://orcid.org/0000-0002-8280-9238
Alan L. Roy https://orcid.org/0000-0002-1931-0135
Ignacio Ruiz https://orcid.org/0000-0002-0965-5463
Chet Ruszczyk https://orcid.org/0000-0001-7278-9707
Kazi L. J. Rygl https://orcid.org/0000-0003-4146-9043
Salvador Sánchez https://orcid.org/0000-0002-8042-5951
David Sánchez-Argüelles https://orcid.org/0000-0002-7344-9920
Miguel Sánchez-Portal https://orcid.org/0000-0003-0981-9664
Mahito Sasada https://orcid.org/0000-0001-5946-9960
Kaushik Satapathy https://orcid.org/0000-0003-0433-3585
Tuomas Savolainen https://orcid.org/0000-0001-6214-1085
Karl-Friedrich Schuster https://orcid.org/0000-0003-2890-9454

Lijing Shao https://orcid.org/0000-0002-1334-8853
Zhiqiang Shen (沈志强) https://orcid.org/0000-0003-3540-8746
Des Small https://orcid.org/0000-0003-3723-5404
Bong Won Sohn https://orcid.org/0000-0002-4148-8378
Jason SooHoo https://orcid.org/0000-0003-1938-0720
Kamal Souccar https://orcid.org/0000-0001-7915-5272
He Sun (孙赫) https://orcid.org/0000-0003-1526-6787
Fumie Tazaki https://orcid.org/0000-0003-0236-0600
Remo P. J. Tilanus https://orcid.org/0000-0002-6514-553X
Michael Titus https://orcid.org/0000-0002-3423-4505
Pablo Torne https://orcid.org/0000-0001-8700-6058
Efthalia Traianou https://orcid.org/0000-0002-1209-6500
Sascha Trippe https://orcid.org/0000-0003-0465-1559
Ilse van Bemmel https://orcid.org/0000-0001-5473-2950
Huib Jan van Langevelde https://orcid.org/0000-0002-0230-5946
Daniel R. van Rossum https://orcid.org/0000-0001-7772-6131
Jesse Vos https://orcid.org/0000-0003-3349-7394
Jan Wagner https://orcid.org/0000-0003-1105-6109
Derek Ward-Thompson https://orcid.org/0000-0003-1140-2761
John Wardle https://orcid.org/0000-0002-8960-2942
Jonathan Weintroub https://orcid.org/0000-0002-4603-5204
Norbert Wex https://orcid.org/0000-0003-4058-2837
Robert Wharton https://orcid.org/0000-0002-7416-5209
Kaj Wiik https://orcid.org/0000-0002-0862-3398
Michael F. Wondrak https://orcid.org/0000-0002-6894-1072
George N. Wong https://orcid.org/0000-0001-6952-2147
Qingwen Wu (吴庆文) https://orcid.org/0000-0003-4773-4987
Paul Yamaguchi https://orcid.org/0000-0002-6017-8199
Doosoo Yoon https://orcid.org/0000-0001-8694-8166
André Young https://orcid.org/0000-0003-0000-2682
Ken Young https://orcid.org/0000-0002-3666-4920
Ziri Younsi https://orcid.org/0000-0001-9283-1191
Feng Yuan (袁峰) https://orcid.org/0000-0003-3564-6437
Ye-Fei Yuan (袁业飞) https://orcid.org/0000-0002-7330-4756
J. Anton Zensus https://orcid.org/0000-0001-7470-3321
Shuo Zhang https://orcid.org/0000-0002-2967-790X
Guang-Yao Zhao https://orcid.org/0000-0002-4417-1659
Shan-Shan Zhao https://orcid.org/0000-0002-9774-3606

References

Astropy Collaboration, Price-Whelan, A. M., Sipőcz, B. M., et al. 2018, AJ, 156, 123
Baganoff, F. K., Bautz, M. W., Brandt, W. N., et al. 2001, Natur, 413, 45
Balick, B., & Brown, R. L. 1974, ApJ, 194, 265
Blackburn, L., Chan, C.-k., Crew, G. B., et al. 2019, ApJ, 882, 23
Boehle, A., Ghez, A. M., Schödel, R., et al. 2016, ApJ, 830, 17
Bouffard, É., Haggard, D., Nowak, M. A., et al. 2019, ApJ, 884, 148
Bower, G. C., Broderick, A., Dexter, J., et al. 2018, ApJ, 868, 101
Bower, G. C., Dexter, J., Asada, K., et al. 2019, ApJL, 881, L2
Bower, G. C., Markoff, S., Dexter, J., et al. 2015, ApJ, 802, 69
Boyce, H., Haggard, D., Witzel, G., et al. 2019, ApJ, 871, 161
Brinkerink, C., Falcke, H., Brunthaler, A., & Law, C. 2021, arXiv:2107.13402
Brinkerink, C. D., Falcke, H., Law, C. J., et al. 2015, A&A, 576, A41
Broderick, A. E., Gold, R., Georgiev, B., et al. 2022, ApJL, 930, L21
Brown, R. L., & Lo, K. Y. 1982, ApJ, 253, 108
Capellupo, D. M., Haggard, D., Choux, N., et al. 2017, ApJ, 845, 35
Chan, C.-K., Psaltis, D., Özel, F., et al. 2015, ApJ, 812, 103
Chatterjee, K., Markoff, S., Neilsen, J., et al. 2021, MNRAS, 507, 5281
Chesler, P. M., Blackburn, L., Doeleman, S. S., et al. 2021, CQGra, 38, 125006
Dexter, J., Kelly, B., Bower, G. C., et al. 2014, MNRAS, 442, 2797
Do, T., Ghez, A. M., Morris, M. R., et al. 2009, ApJ, 691, 1021
Do, T., Hees, A., Ghez, A., et al. 2019a, Sci, 365, 664
Do, T., Witzel, G., Gautam, A. K., et al. 2019b, ApJL, 882, L27
Doeleman, S. S., Weintroub, J., Rogers, A. E. E., et al. 2008, Natur, 455, 78
Eckart, A., Baganoff, F. K., Morris, M., et al. 2004, A&A, 427, 1
Eckart, A., Baganoff, F. K., Schödel, R., et al. 2006, A&A, 450, 535
Eckart, A., García-Marín, M., Vogel, S. N., et al. 2012, A&A, 537, A52
Edelson, R. A., & Krolik, J. H. 1988, ApJ, 333, 646
Event Horizon Telescope Collaboration, Akiyama, K., Alberdi, A., et al. 2019a, ApJL, 875, L1
Event Horizon Telescope Collaboration, Akiyama, K., Alberdi, A., et al. 2019b, ApJL, 875, L2
Event Horizon Telescope Collaboration, Akiyama, K., Alberdi, A., et al. 2019c, ApJL, 875, L3
Event Horizon Telescope Collaboration, Akiyama, K., Alberdi, A., et al. 2019d, ApJL, 875, L4
Event Horizon Telescope Collaboration, Akiyama, K., Alberdi, A., et al. 2019e, ApJL, 875, L5
Event Horizon Telescope Collaboration, Akiyama, K., Alberdi, A., et al. 2019f, ApJL, 875, L6
Event Horizon Telescope Collaboration, Akiyama, K., Alberdi, A., et al. 2022a, ApJL, 930, L12
Event Horizon Telescope Collaboration, Akiyama, K., Alberdi, A., et al. 2022b, ApJL, 930, L13
Event Horizon Telescope Collaboration, Akiyama, K., Alberdi, A., et al. 2022c, ApJL, 930, L14
Event Horizon Telescope Collaboration, Akiyama, K., Alberdi, A., et al. 2022d, ApJL, 930, L15
Event Horizon Telescope Collaboration, Akiyama, K., Alberdi, A., et al. 2022e, ApJL, 930, L16
Event Horizon Telescope Collaboration, Akiyama, K., Alberdi, A., et al. 2022f, ApJL, 930, L17
Emmanoulopoulos, D., McHardy, I. M., & Uttley, P. 2010, MNRAS, 404, 931
Falcke, H., Markoff, S., & Bower, G. C. 2009, A&A, 496, 77
Farah, J., Galison, G., Kazunori, K., et al. 2022, ApJL, 930, L18
Fazio, G. G., Hora, J. L., Witzel, G., et al. 2018, ApJ, 864, 58
Fish, V. L., Doeleman, S. S., Beaudoin, C., et al. 2011, ApJL, 727, L36
Freimer, M., Kollia, G., Mudholkar, G. S., & Lin, C. T. 1988, Commun. Stat., 17, 3547
Genzel, R., Schödel, R., Ott, T., et al. 2003, Natur, 425, 934
Georgiev, B., Pesce, D. W., Broderick, A. E., et al. 2022, ApJL, 930, L20
Ghez, A. M., Salim, S., Weinberg, N. N., et al. 2008, ApJ, 689, 1044
Ghez, A. M., Wright, S. A., Matthews, K., et al. 2004, ApJL, 601, L159
Gillessen, S., Eisenhauer, F., Trippe, S., et al. 2009, ApJ, 692, 1075
Gillessen, S., Plewa, P. M., Eisenhauer, F., et al. 2017, ApJ, 837, 30
Goddi, C., Martí-Vidal, I., Messias, H., et al. 2019, PASP, 131, 075003
Goddi, C., Martí-Vidal, I., Messias, H., et al. 2021, ApJL, 910, L14
Gravity Collaboration, Abuter, R., Amorim, A., et al. 2018a, A&A, 615, L15
Gravity Collaboration, Abuter, R., Amorim, A., et al. 2018b, A&A, 618, L10
Gravity Collaboration, Abuter, R., Amorim, A., et al. 2019, A&A, 625, L10
Gravity Collaboration, Abuter, R., Amorim, A., et al. 2020, A&A, 638, A2
Guo, F., Li, H., Daughton, W., & Liu, Y.-H. 2014, PhRvL, 113, 155005
Hadar, S., Johnson, M. D., Lupsasca, A., & Wong, G. N. 2021, PhRvD, 103, 104038
Haggard, D., Nynka, M., Mon, B., et al. 2019, ApJ, 886, 96
Högbom, J. A. 1974, A&AS, 15, 417
Issaoun, S., Johnson, M. D., Blackburn, L., et al. 2019, ApJ, 871, 30
Iwata, Y., Oka, T., Tsuboi, M., Miyoshi, M., & Takekawa, S. 2020, ApJL, 892, L30
Johnson, M. D., Narayan, R., Psaltis, D., et al. 2018, ApJ, 865, 104
Kelly, B. C., Bechtold, J., & Siemiginowska, A. 2009, ApJ, 698, 895
Kozłowski, S. 2016, MNRAS, 459, 2787
Kozłowski, S. 2017, A&A, 597, A128
Lehar, J., Hewitt, J. N., Roberts, D. H., & Burke, B. F. 1992, ApJ, 384, 453
Li, Y.-P., Yuan, F., Yuan, Q., et al. 2015, ApJ, 810, 19
Lo, K. Y., & Claussen, M. J. 1983, Natur, 306, 647
Marrone, D. P. 2006, PhD thesis, Harvard University
Marrone, D. P., Baganoff, F. K., Morris, M. R., et al. 2008, ApJ, 682, 373
Marrone, D. P., Moran, J. M., Zhao, J.-H., & Rao, R. 2006, JPhCS, 54, 354
Martí-Vidal, I., Roy, A., Conway, J., & Zensus, A. J. 2016, A&A, 587, A143
Martí-Vidal, I., Vlemmings, W. H. T., Muller, S., & Casey, S. 2014, A&A, 563, A136
Matthews, L. D., Crew, G. B., Doeleman, S. S., et al. 2018, PASP, 130, 015002

McMullin, J. P., Waters, B., Schiebel, D., Young, W., & Golap, K. 2007, in ASP Conf. Ser. 376, Astronomical Data Analysis Software and Systems XVI, ed. R. A. Shaw, F. Hill, & D. J. Bell (San Francisco, CA: ASP), 127
Melia, F., & Falcke, H. 2001, ARA&A, 39, 309
Meyer, L., Do, T., Ghez, A., et al. 2009, ApJ, 694, L87
Moriyama, K., Mineshige, S., Honma, M., & Akiyama, K. 2019, ApJ, 887, 227
Mościbrodzka, M., Shiokawa, H., Gammie, C. F., & Dolence, J. C. 2012, ApJL, 752, L1
Murchikova, L., & Witzel, G. 2021, ApJL, 920, L7
Mushotzky, R. F., Edelson, R., Baumgartner, W., & Gandhi, P. 2011, ApJL, 743, L12
Neilsen, J., Markoff, S., Nowak, M. A., et al. 2015, ApJ, 799, 199
Neilsen, J., Nowak, M. A., Gammie, C., et al. 2013, ApJ, 774, 42
Ponti, G., De Marco, B., Morris, M. R., et al. 2015, MNRAS, 454, 1525
Porquet, D., Predehl, P., Aschenbach, B., et al. 2003, A&A, 407, L17
Rasmussen, C. E., & Williams, C. K. I. 2006, Gaussian Processes for Machine Learning (Cambridge, MA: MIT Press)
Ricarte, A., Gammie, C., Narayan, R., & Prather, B. S. 2022, arXiv:2202.02408
Richards, J. L., Max-Moerbeck, W., Pavlidou, V., et al. 2011, ApJS, 194, 29
Ripperda, B., Liska, M., Chatterjee, K., et al. 2022, ApJL, 924, L32
Rybicki, G. B., & Lightman, A. P. 1979, Radiative Processes in Astrophysics (New York: Wiley-Interscience)
Scargle, J. D. 1982, ApJ, 263, 835
Simonetti, J. H., Cordes, J. M., & Heeschen, D. S. 1985, ApJ, 296, 46
Sironi, L., & Spitkovsky, A. 2014, ApJL, 783, L21
Speagle, J. S. 2020, MNRAS, 493, 3132
Su, S. 2007, J. Stat. Softw., 21, 1
Tetarenko, A. J., Casella, P., Miller-Jones, J. C. A., et al. 2021, MNRAS, 504, 3862
Uttley, P., McHardy, I. M., & Papadakis, I. E. 2002, MNRAS, 332, 231
van der Laan, H. 1966, Natur, 211, 1131
Vanderplas, J., Connolly, A., Ivezić, Ž., & Gray, A. 2012, in Conf. on Intelligent Data Understanding (CIDU), Introduction to astroML: Machine learning for astrophysics (Piscataway, NJ: IEEE), 47
Virtanen, P., Gommers, R., Oliphant, T. E., et al. 2020, Nat. Methods, 17, 261
Werner, G. R., Uzdensky, D. A., Cerutti, B., Nalewajko, K., & Begelman, M. C. 2015, ApJ, 816, L8
Wielgus, M., Horák, J., Vincent, F., & Abramowicz, M. 2020, PhRvD, 102, 084044
Witzel, G., Martinez, G., Hora, J., et al. 2018, ApJ, 863, 15
Witzel, G., Martinez, G., Willner, S. P., et al. 2021, ApJ, 917, 73
Wong, G. N. 2021, ApJ, 909, 217
Wright, M. C. H., & Backer, D. C. 1993, ApJ, 417, 560
Yuan, F., Quataert, E., & Narayan, R. 2003, ApJ, 598, 301
Yuan, Q., & Wang, Q. D. 2016, MNRAS, 456, 1438
Yusef-Zadeh, F., Bushouse, H., Wardle, M., et al. 2009, ApJ, 706, 348
Yusef-Zadeh, F., Wardle, M., Heinke, C., et al. 2008, ApJ, 682, 361
Zu, Y., Kochanek, C. S., Kozłowski, S., & Udalski, A. 2013, ApJ, 765, 106
Zylka, R., Mezger, P. G., Ward-Thompson, D., Duschl, W. J., & Lesch, H. 1995, A&A, 297, 83